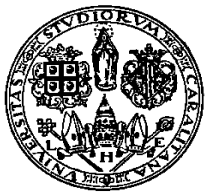

Università degli Studi di Cagliari

DOTTORATO DI RICERCA IN GEOINGEGNERIA E TECNOLOGIE AMBIENTALI

CICLO XXIV

COMPUTATIONAL FLUID DYNAMICS AND EXPERIMENTAL STUDY OF THE HYDRODYNAMICS OF A BUBBLE COLUMN AND AN AIR-WATER JET-STIRRED CELL

Settore scientifico disciplinare di afferenza: NG-IND/06

Tesi di dottorato di: Dott. Ing. Cristina Levanti

Coordinatore Dottorato: Prof. Ing. Aldo Muntoni

Tutore del Dottorato: Prof. Ing. Battista Grosso

Esame finale anno accademico 2011 – 2012

Abstract

A large number of flows encountered in nature and in many industrial processes are intrinsically multiphase flows. The efficiency and the effectiveness of multiphase flow processes strongly depend on the ability to model the fluid flow behaviour. Thus, a robust and accurate description of multiphase flow can lead to an increase in performance, a reduction in cost, and an improvement in safety for engineering systems. In recent years, Computational Fluid Dynamics (CFD) has become an indispensable predictive tool for gathering information to be used for design and optimization for fluid systems.

In this thesis the hydrodynamics of two bubbly flow systems, a bubble column and a waterjet - agitated flotation cell (Hydrojet cell), were studied by means of numerical simulations. In order to validate the bubble column CFD simulations Particle Image Velocimetry (PIV) was used. An experimental investigation about bubble size distribution (BSD) along a water jet was carried out by means of image analysis. Because of high gas fraction and high velocity of the air/water streams used to agitate the Hydrojet cell, with the available equipment, no experimental measurements could be done to evaluate the velocity field of the cell.

The thesis consists of three parts: theoretical part, bubble column study and Hydrojet cell study.

In the theoretical part, first, a summary of fluid dynamics principles and an overview of the principal issues related to multiphase flow modelling were presented. Then a brief introduction to PIV and its application to two phase bubbly flow were given. Finally a review of the principle of the flotation process and its modelling were done in order to highlight the reasons for the low recovery of fine particles. Then the potentialities offered by the use of waterjets to fine particles flotation were presented.

In the second part experimental and numerical studies of a bubble column were presented. PIV technique was used to determine the velocity field of a laboratory bubble column. A separation method for multiphase PIV was developed and tested. By means of the proposed method, the acquired mixed-fluid images were processed to obtain two sets of single phase images before PIV analysis. The velocity field was determined using a multi-pass cross-correlation. Following three-dimensional time-dependent CFD simulations of a lab-scale bubble column were presented. The simulations were carried out using the Euler - Euler approach. Two different multiphase turbulence models, Shear Stress Transport (SST) and Large Eddy Simulation (LES), were tested, and different interfacial closure models reported in the literature were examined. When LES were used to model the turbulence instead of the SST model, much better agreement with the experimental data was found, provided that the drag, lift and virtual mass forces were taken into account.

In the third part a preliminary experimental study, carried out in a rectangular flat cell, was presented. It was carried out to investigate the size distribution of bubbles

generated by a moderate pressure water jet, by means of image analysis. This study showed the ability of water jets at moderate pressure to break an air stream into small bubbles. Increasing the pressure of the pump, smaller and more uniform bubbles were obtained.

Then three-dimensional CFD simulations of the Hydrojet cell are presented. The Hydrojet cell, due to the exceeding computational burden, was simulated as a two-phase (gas-liquid) system, although actually it is a three-phase (gas-liquid-solid) system. Also in this case simulations were carried out using the Euler - Euler approach. The turbulence of the liquid phase was modelled with the SST model. The single reference frame technique was used to describe the movement of the waterjet lance. To achieve a homogeneous aeration in the region near the inlets different inlet velocity and rotational speed were tested.

The results gave useful indications about the role of the four principal operating parameters: nozzles diameter, velocity of rotation of the lance, speed of the water jets and then pressure of the pump and inlet air flow rate. What emerges is the need of high rotational speed of the waterjet lance in order to ensure an uniform gas distribution within the mixing zone. This is not possible with the current apparatus. Thus in order to make the system suitable to produce an appropriate environment for the full development of the flotation process it is necessary to modify the system.

Acknowledgements

This thesis is the end of my journey in obtaining my Ph.D. I would like to thank all those people who made this thesis possible and an unforgettable experience for me.

First of all, I would like to thank my tutor, Professor Battista Grosso, for his suggestions, comments, patience and understanding. I would like to express my thanks to Professor Raimondo Ciccu. It has been a great privilege for me to work with him and learn from his experience.

I would like to thank my present and former colleagues for their help and support: Giovanni Mei, Marco Cigagna, Erminia Marras, Antonio Marocco e Giorgio Costa.

I would like to express my very sincere gratitude to Prof. Nielsen Deen from the Eindhoven University of Technology who kindly gave me the opportunity to conduct part of my research at the TU/e. He always offered me advice and support throughout my stay in Eindhoven.

I would also like to thank all of the members of the Multiphase Reactors group (SMR) at Eindhoven University of Technology who have made my stay in Eindhoven easier and unforgettable.

I would like to thank my parents, especially my mom, and my family, who have over the years supported and guided me in my endeavours. I thank my partner, Nicola, for his support, love, and immense patience throughout the years. Without him I could never have managed until the end. Last but not least, I'd like to thank my friends, especially Elide, for providing support and friendship that I needed.

Contents

List of Figures

List of Tables

Chapter 1 Introduction

A large number of flows encountered in nature and in many industrial processes are intrinsically multiphase flows. The term multiphase flow is used to refer to any fluid flow consisting of more than one phase or component. It's possible to classify them according to the state of the different phases or components and therefore refers to gas/solids flows, or liquid/solids flows or gas/particle flows or bubbly flows and so on. Also two general topologies of multiphase flow can be usefully identified at the outset, namely disperse flows and separated flows. By disperse flows we mean those consisting of finite particles, drops or bubbles (the disperse phase) distributed in a connected volume of the continuous phase. On the other hand separated flows consist of two or more continuous streams of different fluids separated by interfaces.

The efficiency and the effectiveness of multiphase flow processes strongly depend on the ability to model and thus to predict the fluid flow behaviour. There are three ways in which such models are investigated: experimentally, through laboratory-sized models equipped with appropriate instrumentation, theoretically, using mathematical equations and models for the flow, and computationally, using the power and size of modern computers to address the complexity of the flow.

In this thesis the hydrodynamics of two dispersed bubbly flow systems, a bubble column and the Hydrojet cell, are investigated through numerical simulations and experiments. Both will be introduce in the following sections.

A bubble column is a vertical column of liquid with gas introduced continuously at the bottom through a sparger. Bubbles form and travel upwards through the column due to the inlet gas velocity and buoyancy. Because of their simple construction and operation, bubble columns are widely used in process industries. Due to their industrial importance and wide application area, the design and scale-up of bubble column reactors, investigation of important hydrodynamic and operational parameters characterizing their operation have gained considerable attention during the past 20 years.

The Hydrojet cell is a waterjet-agitated flotation cell which has been designed and built at the DIGITA Laboratories of the University of Cagliari. A detailed description of this system will be given in Chapter 9.

1.1 Numerical simulations

Computational fluid dynamics (CFD) is one of the tools (in addition to experimental and theoretical methods) available to solve fluid-dynamic problems.

Fluid motion is governed by the Navier-Stokes equations, a set of coupled and nonlinear partial differential equations (PDE) derived from the basic laws of conservation of mass, momentum and energy. The analytical solution of these equations is practically impossible save for the simplest of flows.

CFD is the art of replacing such PDE systems by a set of algebraic equations which can be solved using digital computers. The central process in CFD is the process of discretization, i.e. the process of taking differential equations with an infinite number of degrees of freedom, and reducing it to a system of finite degrees of freedom. Hence, instead of determining the solution everywhere and for all times, we will be satisfied with its calculation at a finite number of locations and at specified time intervals. The partial differential equations are then reduced to a system of algebraic equations that can be solved on a computer.

The fundamental elements of any CFD simulation are (Apsley 2013):

- the flow field is discretized; i.e. field variables (ρ, u, v, w, p, etc) are approximated by their values at a finite number of nodes;
- the equations of motion are discretized (approximated in terms of values at nodes) by means of numerical methods to obtain a system of algebraic equations;
- the resulting system of algebraic equations is solved to give values at the nodes.

The main stages in a CFD simulation are:

1. pre-processing:
   - formulation of the problem (governing equations, boundary conditions, initial conditions, fluid(s) properties): *mathematical model*;
   - definition of the geometry of the region of interest: *computational domain;*
   - grid generation - construction of a computational mesh (set of control volumes).
2. solving:
   - discretization of the governing equations;
   - solution of the resulting algebraic equations. Discretization yields a large number of algebraic equations (one set for each cell). These equations are then generally solved using an iterative method, starting with a first guess value for all variables and completing a computational cycle. Error or residual values are computed from the discretized equations and the calculations repeated many times, reducing the residual values, until a sufficiently converged solution is judged to have been reached.
3. post-processing:
   - visualization (graphs and plots of the solution);
   - analysis of results (calculation of derived quantities: forces, flow rates, etc.).

While CFD models are fairly well-establish for single phase flow, the physical modelling and the numerical computation of multiphase flows pose great challenges. In all multiphase models, the main difficulties are due to the interfaces between the phases and the discontinuities associate to them (Ishii & Mishimam 1984). The formulation of the constitutive equations is the greatest difficulty when developing a multiphase model for a practical application (Drew & Lahey 1979). As a result, the constitutive equations applied still include considerable uncertainties. Empirical information thus forms an essential part of the model (Manninen & Taivassalo 1996).

Multiphase flow approaches include a wide variety of approaches such as variations in reference frame representation (Eulerian or Lagrangian), phase coupling (intra-phase and/or inter-phase coupling), and particle/flow detail (e.g., high resolution around a

single particle or bulk description of thousands or millions of particles). These different approaches are associated with large variations in computer usage and predictive fidelity. Thus, simulation of dispersed multiphase flow requires careful consideration of both the flow regimes and the relevant numerical approaches. An overview of the methods used to simulate such flow problems numerically is given in Chapter 3.

1.2 Experiments

In order to make certain the computational results of a particular numerical model is reliable and consistent with the flow physics under investigation, capabilities of this numerical model for predicting realistic physical processes and phenomena have to be confirmed before the model is accepted and applied to simulating real world problems (Jia & Wang 2005). Many different measurement techniques are available for this purpose. The most frequently used methods is the Particle Image Velocimetry (PIV). PIV is the newest entrant to the field of fluid flow measurement and provides instantaneous velocity fields over global domains. This technique records the position over time of small tracer particles introduced into the flow to extract the local fluid velocity.

The main disadvantage of optical imaging techniques is their need for undisturbed visibility to the measurement volume. In a multiphase flow, visibility is hampered by the dispersed particles located on the optical path from the focal plane (i.e., measurement volume) to the camera. The limit of the gas fraction in PIV measurements in dispersed gas-liquid flows is discuss in Chapter 4. Using PIV, whole field information of the mean and fluctuating velocities of both phases can be determine, which are typically the quantities of interest for the validation of CFD results.

PIV technique was used to validate the results of the bubble column simulations, while it was not possible, with the available equipment, to do PIV measurements of the Hydrojet cell, due to the high gas fraction and the strong turbulence that characterized the area surrounding the two inlet nozzles.

1.3 Objectives

The objectives of the first part of this study were to determine the flow pattern in a square bubble column experimentally and computationally, and to compare the computations with the experimental data. The experimental results are obtained by PIV measurements. The challenge in applying PIV to multiphase flows is in separating the tracer particles tracking the entrained continuous phase from the dispersed phase. Up to the present no comprehensive method for discerning the phases of multiphase flows has been developed, although optical separation methods have proven to be the most reliable(Deen et al. 2001, Bröder & Sommerfeld 2002). However it is desired to have a cheaper and easier method to avoid the complex and expensive set-up for the optical separation methods. With this aim a simple, inexpensive method of phase separation is proposed.

The aim of the second part of this thesis is to investigate about the feasibility of applying water jet to flotation process, developing a numerical model of a waterjet-agitated cell, through which to obtain useful information about the design of the

Hydrojet system. A proper numerical model of the cell would be able to reduce scale-up problems, highlighting the role of each operating parameter.

Chapter 2 Fluid Dynamics

2.1 Introduction

The starting point of any numerical simulation is the governing equations of the physics of the problem to be solved. These equations together with boundary conditions, initial conditions and the fluid(s) properties defined the *mathematical model*. In this chapter all the elements constituent the mathematical model (governing equations, turbulence models and boundary conditions) for a single phase flow and the approaches to multiphase modelling are briefly presented.

2.2 Governing equations

The governing equations of fluid flow represent mathematical statements of the conservation laws of physics:

1. the mass of fluid is conserved;
2. the rate of change of momentum equals the sum of the forces on a fluid particle (Newton's second law);
3. the rate of change of energy is equal to the sum of the rate of heat addition to and the rate of work done on a fluid particle (first law of thermodynamics).

In the following, the fluid is assumed to be incompressible (ρ = cost) and isothermal. Therefore the energy equation are not required to solve the problem.

2.2.1 Continuity equation

For a stationary differential control volume, application of law of conservation of mass yields the continuity equation in differential form. It is given by

$$\frac{\partial \rho}{\partial t} + \nabla \cdot (\rho \mathbf{u}) = 0 \tag{2.1}$$

where $\mathbf{u}$ is the velocity vector containing the u, v and w velocity components in the x, y and z directions and ρ is the density per unit mass.

For incompressible flows (ρ = cost), the continuity equation (Equation (2.1)) reduces to

$$\nabla \cdot (\rho \mathbf{u}) = 0. \tag{2.2}$$

2.2.2 Momentum equation

Application of the law of conservation of momentum yields a basic set of equations governing the motion of fluids, which are used to calculate velocity and pressure fields.

Cauchy's equation is obtained by considering the equation of motion ('sum of all forces = mass times acceleration') of an infinitesimal volume of fluid. For a fluid which is subject to body forces $\mathbf{f}$, Cauchy's equation is given by

$$\frac{\partial (\rho \mathbf{u})}{\partial t} + \nabla \cdot (\rho \mathbf{u}\mathbf{u}) = -\nabla \cdot \bar{\bar{\sigma}} + \rho \mathbf{f} \tag{2.3}$$

where $\bar{\bar{\sigma}}$ is the stress tensor, and $\mathbf{f}$ contains all of the body forces per unit volume (often simply density times gravity). $\mathbf{u}$ is the velocity vector field, which depends on time and space.

That Cauchy's equation is valid for any continuum provided its deformation is described by an Eulerian approach.

The stress tensor can be split into two contributes:

$$\bar{\bar{\sigma}} = -p\mathbb{I} + \bar{\bar{\tau}} \tag{2.4}$$

where p is the pressure, $\mathbb{I}$ is the 3x3 identity matrix and $\bar{\bar{\tau}}$ the deviatoric stress tensor.

In Equation (2.3) the first term is the rate of increase in momentum per unit volume; the second term represents change in momentum per unit volume, caused by convection; the third term, which include pressure and viscous forces per unit volume, represents molecular contributions, the fourth term represents the gravitational force per unit volume and any other external force, if present.

In order to use these general momentum conservation equations to calculate the velocity field, it is necessary to express viscous stress terms in terms of the velocity field. The equations which relate the stress tensor to the motion of the continuous fluid are called constitutive equations or rheological equations of state. Although the governing momentum conservation equations are valid for all fluids, the constitutive equations, in general, vary from one fluid material to another and possibly also from one type of flow to another.

2.2.3 Constitutive equations

The constitutive equations provide the missing link between the rate of deformation and the resulting stresses in the fluid. The surface stresses $\bar{\bar{\sigma}}$ on any element arise from a combination of pressure p and viscous friction, as prescribed by the constitutive relations:

$$\begin{aligned}
\sigma_{xx} &= -p + \lambda\nabla\cdot\mathbf{u} + 2\mu\frac{\partial u}{\partial x} \quad & \sigma_{yy} &= -p + \lambda\nabla\cdot\mathbf{u} + 2\mu\frac{\partial v}{\partial y} \\
\sigma_{zz} &= -p + \lambda\nabla\cdot\mathbf{u} + 2\mu\frac{\partial w}{\partial z} \quad & \sigma_{xy} &= \sigma_{yx} = \mu\left(\frac{\partial u}{\partial y} + \frac{\partial v}{\partial x}\right) \\
\sigma_{xz} &= \sigma_{zx} = \mu\left(\frac{\partial u}{\partial z} + \frac{\partial w}{\partial x}\right) \quad & \sigma_{yz} &= \sigma_{zy} = \mu\left(\frac{\partial v}{\partial z} + \frac{\partial w}{\partial y}\right)
\end{aligned} \tag{2.5}$$

where μ and λ are the coefficients of dynamic and bulk viscosity respectively. These expressions assume that the relationship between stress and velocity gradients is

- linear (which is valid for Newtonian fluids) and
- isotropic (i.e., the intrinsic properties of the fluid have no preferred direction).

2.2.4 Incompressible Navier-Stokes equations

Fluids, which follow Newton's law of viscosity (although it is referred to as a law, it is just an empirical proposition) are called Newtonian fluids. For such fluids, the viscous stress at a point is linearly dependent on the rates of strain (deformation), as already mentioned in the previous section.

For incompressible flow (Equation (2.2)) and Newtonian fluids the constitutive relations then reduce to

$$\sigma_{ij} = -p\delta_{ij} + \mu\left(\frac{\partial u_i}{\partial x_j} + \frac{\partial u_j}{\partial x_i}\right) \tag{2.6}$$

where δ_{ij} is the Kronecker delta.

Substitution of the constitutive equations (2.6) for an incompressible Newtonian fluid into Cauchy's equations (Equation (2.3)), gives the incompressible Navier–Stokes (N–S) equations:

$$\frac{\partial(\rho\mathbf{u})}{\partial t} + \nabla\cdot(\rho\mathbf{u}\mathbf{u}) = -\nabla p + \mu\nabla^2\mathbf{u} + \rho\mathbf{f}. \tag{2.7}$$

In combination with the equation of continuity (Equation (2.2)) the three momentum equations form a system of four coupled nonlinear, partial differential equations (second order in space and first order in time) for the three velocity components u_i and the pressure p.

This system is mathematically closed, i.e. it can be solved provided that suitable auxiliary conditions, initial and boundary conditions, are supplied.

2.3 Boundary conditions

In order to solve the closed set of governing model equations, it is necessary to specify appropriate initial conditions and boundary conditions. For any reactor engineering problem, it will be necessary to select an appropriate solution domain, which is an important step in model formulation. The solution domain isolates the system being modelled from the surrounding environment. The influence of the environment on the flow processes of interest within the solution domain is represented by suitable formulations of boundary conditions.

The form of the boundary conditions that is required by any partial differential equation depends on the equation itself and the way that it has been discretize. Common boundary conditions are classified either in terms of the numerical values that have to be set or in terms of the physical type of the boundary condition. For steady state problems there are three types of spatial boundary conditions that can be specified as follows (Renade 2002):

1. Dirichlet boundary condition: $\phi = f_1(x, y, z).$ (2.8)

Here the values of the variable ϕ on the boundary are known constants f_1. This allows a simple substitution to be made to fix the boundary value. For example, if $\mathbf{u}$ is the flow velocity, its value may be fixed at the boundary of the domain. For instance, for no-slip and no-penetration conditions on the solid walls, the fluid velocity is the same as the velocity of the wall.

2. Neuman boundary condition: $\frac{\partial\phi}{\partial n} = f_2(x, y, z).$ (2.9)

Here the derivatives of the variable ϕ on the boundary are known f_2, and this gives an extra equation, which can be used to find the value at the boundary. For example, if the velocity does not change downstream of the flow, we can assume that the derivative of $\mathbf{u}$ is zero at that boundary.

3. Mixed type boundary condition: $a\phi + b\frac{\partial \phi}{\partial n} = f_3(x, y, z).$ (2.10)

The physical boundary conditions that are commonly observed in fluid problems are briefly presented here (Ashgriz & Mostaghimi 2002).

Solid walls

Many boundaries within a fluid flow domain will be solid walls, and these can be either stationary or moving walls. If the flow is laminar then the velocity components can be set to be the velocity of the wall. When the flow is turbulent, however, the situation is more complex.

Inlets

At an inlet, fluid enters the domain and, therefore, its fluid velocity or pressure, or the mass flow rate may be known. Also, the fluid may have certain characteristics, such as the turbulence characterizes which needs to be specified.

Symmetry boundaries

When the flow is symmetrical about some plane there is no flow through the boundary and the derivatives of the variables normal to the boundary are zero.

Cyclic or periodic boundaries

These boundaries come in pairs and are used to specify that the flow has the same values of the variables at equivalent positions on both of the boundaries.

Pressure boundary conditions

The ability to specify a pressure condition at one or more boundaries of a computational region is an important and useful computational tool. Pressure boundaries represent such things as confined reservoirs of fluid, ambient laboratory conditions and applied pressures arising from mechanical devices. Generally, a pressure condition cannot be used at a boundary where velocities are also specified, because velocities are influenced by pressure gradients. The only exception is when pressures are necessary to specify the fluid properties, e.g., density crossing a boundary through an equation of state.

In contrast, a stagnation pressure condition assumes stagnation conditions outside the boundary so that the velocity at the boundary is zero. This assumption requires a pressure drop across the boundary for flow to enter the computational region. Since the static pressure condition says nothing about fluid velocities outside the boundary (i.e., other than it is supposed to be the same as the velocity inside the boundary) it is less specific than the stagnation pressure condition. In this sense the stagnation pressure condition is generally more physical and is recommended for most applications.

Outflow boundary conditions

In many simulations there is a need to have fluid flow out of one or more boundaries of the computational region. At such "outflow" boundaries there arises the question of what constitutes a good boundary condition.

In compressible flows, when the flow speed at the outflow boundary is supersonic, it makes little difference how the boundary conditions are specified since flow disturbances cannot propagate upstream. In low speed and incompressible flows,

however, disturbances introduced at an outflow boundary can have an effect on the entire computational region.

The simplest and most commonly used outflow condition is that of a “continuative" boundary. Continuative boundary conditions consist of zero normal derivatives at the boundary for all quantities. The zero-derivative condition is intended to represent a smooth continuation of the flow through the boundary.

It must be stressed that the continuative boundary condition has no physical basis, rather it is a mathematical statement that may or may not provide the desired flow behavior. In particular, if flow is observed to enter the computational region across such a boundary, then the computations may be wrong because nothing has been specified about flow conditions existing outside the boundary.

As a general rule, a physically meaningful boundary condition, such as a specified pressure condition, should be used at out flow boundaries whenever possible. When a continuative condition is used it should be placed as far from the main flow region as is practical so that any adverse influence on the main flow will be minimal.

Opening boundary bonditions

If the fluid flow crosses the boundary surface in either directions an opening boundary condition needs to be utilized. All of the fluid might flow out of the domain, or into the domain, or a combination of the two might happen.

Free surfaces and interfaces

If the fluid has a free surface, then the surface tension forces need to be considered. This requires utilization of the Laplace's equation which specifies the surface tension-induced jump in the normal stress p_s across the interface:

$$p_s = \sigma\kappa \tag{2.11}$$

where σ represents the liquid-air surface tension and κ the total curvature of the interface. A boundary condition is required at the contact line, the line at which the solid, liquid and gas phases meet. It is this boundary condition which introduces into the model information regarding the wettability of the solid surface.

The solution domain, the co-ordinate system used to formulate the governing equations and the characteristics of the governing equations determine the boundary conditions requirements..

2.4 Turbulence

2.4.1 Introduction

In general Newtonian fluid flow in motion can manifest itself in three states. In the first state the flow is smooth and regular, which is known as ”laminar”. The flow moves in layers and there are no fluctuations of the physical properties. In the second state there can locally be small fluctuations in the flow field and the flow is called ”transitional”. It means that the flow is between laminar and the third and final state which is called ”turbulent”. In this turbulent state physical properties like e.g. the velocity and pressure fluctuate in both time and space. The chaotic state of fluid motion arises when the speed of the fluid exceeds a specific threshold, below which viscous forces damp out the chaotic behaviour. Perhaps the simplest way to define turbulence is by reference to the

Reynolds number, a parameter that characterizes a flow. Named after the British engineer Osborne Reynolds, this number indicates the ratio, or relative importance, of the flow's inertial and viscous forces:

$$Re = \frac{UD}{\nu} \tag{2.12}$$

where U and D are characteristic velocity and length scales of the flow and ν is the kinematic viscosity. If the Reynolds number is low, viscous forces damp out any fluctuation and the flow remains smooth and stable. If the Reynolds number is increased inertial forces start to dominate the viscous forces and eventually the flow becomes irregular and chaotic and we end up with what we call a turbulent flow (Drew & Lahey 1979). In turbulent flow it is usual to divide the velocities in one time-averaged part U_i, which is independent of time (when the mean flow is steady), and one fluctuating part u_i' so that $u_i = U_i + u_i'$.

2.4.2 Characteristics of turbulent flow

There is no definition on turbulent flow, but it has a number of characteristic features (Tennekes & Lumley 1972) such as:

1. *Irregularity*. Turbulent flow is irregular and chaotic (they may seem random, but they are governed by Navier-Stokes equation, Equation (2.7)). The flow consists of a spectrum of different scales (eddy sizes). We do not have any exact definition of a turbulent eddy, but we suppose that it exists in a certain region in space for a certain turbulent time and that it is subsequently destroyed (by the cascade process or by dissipation, see below). It has a characteristic velocity and length (called a velocity and length scale). The region covered by a large eddy may well enclose also smaller eddies. The largest eddies are of the order of the flow geometry (i.e. boundary layer thickness, jet width, etc). At the other end of the spectra we have the smallest eddies which are dissipated by viscous forces (stresses) into thermal energy resulting in a temperature increase. Even though turbulence is chaotic it is deterministic and is described by the Navier-Stokes equations.
2. *Diffusivity*. In turbulent flow the diffusivity increases. This means that the spreading rate of boundary layers, jets, etc. increases as the flow becomes turbulent. The turbulence increases the exchange of momentum in e.g. boundary layers and reduces or delays thereby separation at bluff bodies such as cylinders, airfoils and cars. The increased diffusivity also increases the resistance (wall friction) in internal flows such as in channels and pipes.
3. *Large Reynolds Numbers*. Turbulent flow occurs at high Reynolds number.
4. *Three-Dimensional*. Turbulent flow is always three-dimensional. However, when the equations are time averaged we can treat the flow as two-dimensional (if the geometry is two-dimensional).
5. *Dissipation*. Turbulent flow is dissipative, which means that kinetic energy in the small (dissipative) eddies are transformed into internal energy. The small eddies receive the kinetic energy from slightly larger eddies. The slightly larger eddies receive their energy from even larger eddies and so on. The largest eddies extract their energy from the mean flow. This process of transferred energy

from the largest turbulent scales (eddies) to the smallest is called *cascade process*.

6. *Continuum*. Even though we have small turbulent scales in the flow they are process much larger than the molecular scale and we can treat the flow as a continuum.

2.4.3 Turbulence scales

In turbulent flow a wide range of scales are present. The largest scales are of the order of the flow geometry (the boundary layer thickness, for example), with length scale ℓ_0 and velocity scale v_0. These scales extract kinetic energy from the mean flow which has a time scale comparable to the large scales, i.e.

$$\frac{\partial U}{\partial y} = O(t_0^{-1}) = O\left(\frac{v_0}{\ell_0}\right). \tag{2.13}$$

Part of the kinetic energy of the large scales is lost to slightly smaller scales with which the large scales interact. Through the *cascade process*, kinetic energy is in this way transferred from the largest scale to the smallest scales. At the smallest scales the frictional forces (viscous stresses) become large and the kinetic energy is transformed (dissipated) into thermal energy. The kinetic energy transferred from eddy-to-eddy (from an eddy to a slightly smaller eddy) is the same per unit time for each eddy size.

The dissipation is denoted by ε which is energy per unit time and unit mass ($\varepsilon = [m^2/s^3]$). The dissipation is proportional to the kinematic viscosity, ν, times the fluctuating velocity gradient up to the power of two. The friction forces exist of course at all scales, but they are largest at the smallest eddies. In reality a small fraction is dissipated at all scales. However it is assumed that most of the energy that goes into the large scales per unit time (say 90%) is finally dissipated at the smallest (dissipative) scales.

The smallest scales where dissipation occurs are called the Kolmogorov scales whose velocity scale is denoted by v_η, length scale by ℓ_η and time scale by τ_η. We assume that these scales are determined by :

- *viscosity*, ν: since the kinetic energy is destroyed by viscous forces it is natural to assume that viscosity plays a part in determining these scales; the larger viscosity, the larger scales;
- *dissipation* ε: the amount of energy that is to be dissipated is ε. The more energy that is to be transformed from kinetic energy to thermal energy, the larger the velocity gradients must be.

Having assumed that, we can express v_η, ℓ_η and τ_η in ν and ε using dimensional analysis.

$$\begin{aligned} v_\nu &= \nu^a \quad \varepsilon^b \\ [m/s] &= [m^2/s][m^2/s^3] \end{aligned} \tag{2.14}$$

where below each variable its dimensions are given. The dimensions of the left and the right side must be the same. We get two equations, one for meters [m]

$$1 = 2a + 2b \tag{2.15}$$

and one for seconds [s]

$$-1 = -a - 3b \tag{2.16}$$

which give $a = b = 1/4$. In the same way we obtain the expressions for ℓ_η and τ_η so that

$$n_\eta = (\nu\varepsilon)^{\frac{1}{4}}, \quad \ell_\eta = \left(\frac{\nu^3}{\varepsilon}\right)^{\frac{1}{4}}, \quad \tau_\eta = \left(\frac{\nu}{\epsilon}\right)^{\frac{1}{2}}. \tag{2.17}$$

2.4.4 Energy spectrum

The turbulent scales are distributed over a range of scales which extends from the largest scales which interact with the mean flow to the smallest scales where dissipation occurs. In wave number space the energy of eddies from κ to $\kappa + d\kappa$ can be expressed as

$$E(\kappa)d\kappa \tag{2.18}$$

where Equation (2.18) expresses the contribution from the scales with wave number between κ and $\kappa + d\kappa$ to the turbulent kinetic energy κ. The dimension of wave number is one over length; thus we can think of wave number as proportional to the inverse of an eddy's radius, i.e $\kappa \propto 1/r$. The total turbulent kinetic energy is obtained by integrating over the whole wave number space i.e.

$$k = \int_0^\infty E(\kappa)d\kappa. \tag{2.19}$$

The kinetic energy is the sum of the kinetic energy of the three fluctuating velocity components, i.e.

$$k = \frac{1}{2}(\overline{u'^2} + \overline{v'^2} + \overline{w'^2}) = \frac{1}{2}\overline{u_i' u_i'}. \tag{2.20}$$

The spectrum of E is shown in Figure 2.1. We find regions I, II and III which correspond to:

I. in this region we have the large eddies which carry most of the energy. These eddies interact with the mean flow and extract energy from the mean flow. Their energy is passed on to slightly smaller scales. The eddies' velocity and length scales are U and ℓ, respectively;

III. dissipation range. The eddies are small and isotropic and it is here that the dissipation occurs. The scales of the eddies are described by the Kolmogorov scales (see Equation (2.17))

II. inertial sub-range. The existence of this region requires that the Reynolds number is high (fully turbulent flow). The eddies in this region represent the mid-region. This region is a "transport" region in the cascade process. Energy per time unit (ε) is coming from the large eddies at the lower part of this range and is given off to the dissipation range at the higher part. The eddies in this region are independent of both the large, energy containing eddies and the eddies in the dissipation range. One can argue that the eddies in this region should be characterized by the flow of energy (ε) and the size of the eddies $1/\kappa$.
Dimensional reasoning gives

$$E(\kappa) = const.\varepsilon^{\frac{2}{3}}\kappa^{-\frac{5}{3}}. \tag{2.21}$$

This is a very important law (Kolmogorov spectrum law or the $-5/3$ law) which states that, if the flow is fully turbulent (high Reynolds number), the energy spectra should exhibit a $-5/3$-decay.

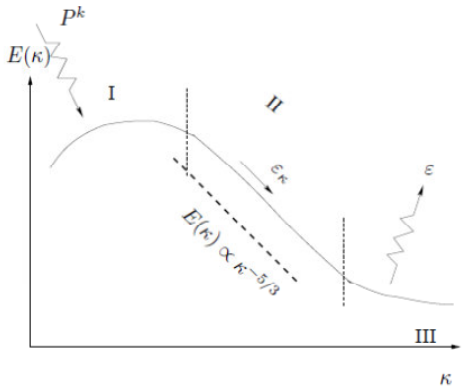

Figure 2.1: Spectrum for k. I: Range for the large, energy containing eddies. II: The inertial sub-range. III: Range for small, isotropic scales (Davidson 2012)

2.5 Turbulence modelling

The solution of the governing equations does not raise any fundamental difficulties in the case of inviscid or laminar flows. The simulation of turbulent flows, however, presents a significant problem. Despite the performance of modern supercomputers, a direct simulation of turbulence by the time-dependent Navier-Stokes equations, called Direct Numerical Simulation (DNS), is still possible only for rather simple flow cases at low Reynolds numbers. The restrictions of the DNS become quite obvious when recalling that the number of grid points needed for sufficient spatial resolution scales as and the CPU-time as Re^3. This does not mean that DNS is completely useless. It is an important tool for understanding the turbulent structures and the laminar turbulent transition. DNS also plays a vital role in the development and calibration of new or improved turbulence models. However, in engineering applications, the effects of turbulence can be taken into account only approximately, using models of various complexities.

The first level of approximation is reached for the Large-Eddy Simulation (LES) approach. The development of LES is founded on the observation that the small scales of turbulent motion posses a more universal character than the large scales, which transport the turbulent energy. Thus, the idea is to resolve only the large eddies accurately and to approximate the effects of the small scales by relatively simple subgrid-scale model. Since LES requires significantly less grid points than DNS, the investigation of turbulent flows at much higher Reynolds numbers becomes feasible. But because LES is inherently three-dimensional and unsteady, it remains computationally still very demanding. LES models are discussed in more detail in Section 2.7.

The next level of approximation is represented by the so-called Reynolds-Averaged Navier-Stokes equations (RANS). This approach, which was presented by Reynolds in 1895, is based on the decomposition of the flow variables into mean and fluctuating parts followed by time or ensemble averaging (Reynolds 1895). In cases where the density is not constant, it is advisable to apply the density (mass) weighted or Favre decomposition (Favre 1965a) to the velocity components. Otherwise, the averaged

governing equations would become considerably more complicated due to additional correlations involving density fluctuations.

By inserting the decomposed variables into the Navier-Stokes equations and averaging, we obtain formally the same equations for the mean variables with the exception of additional one term (for isothermal condition): the Reynolds stress tensor (see next section). Thus the solution of the Reynolds-Averaged Navier-Stokes equations requires the modelling of the Reynolds stresses. A large variety of turbulence models was devised to close the RANS equations and the research still continues. Some of them are discussed in more detail in Section 2.6.

The advantages of this approach are that considerably coarser grids can be used compared to LES, and that stationary mean solution can be assumed (at least for attached or moderately separated flows). Clearly, both features significantly reduce the computational effort in comparison to LES or even DNS. Therefore, the RANS approach is very popular in engineering applications. Of course, because of the averaging procedure, no detailed information can be obtained about turbulent structures.

2.6 Turbulence models based on RANS

2.6.1 Reynolds-Averaged Navier-Stokes (RANS) equations and the closure problem

As previously mentioned the main idea behind Reynolds time-averaging is to express any variable, $\phi(x, y)$, which is a function of time and space, as the sum of a mean, Φ and a fluctuating component, ϕ', commonly called Reynolds' decomposition, as given by

$$\phi(x,t) = \Phi(x) + \phi'(x,t). \tag{2.22}$$

The time averaged quantity is defined as:

$$\Phi = \frac{1}{\Delta t}\int_{t}^{t+\Delta t} \phi dt. \tag{2.23}$$

The Reynolds averaging obeys the following property:

$$\bar{\Phi} = \Phi \quad \bar{\phi}' = 0. \tag{2.24}$$

Equation (2.22) is substituted in the basic governing equations for ϕ and these are then time averaged to yield the governing equations for mean quantities (using Equation (2.24)).

Inserting the Reynolds' decomposition of velocity $(\mathbf{u} = \mathbf{U} + \mathbf{u}')$ and pressure $(p = P + p')$ into the continuity equation (2.1) and the Navier-Stokes equation (2.7) we obtain the Reynolds-averaged form of the conservation equations of mass (overall) and momentum for an incompressible (constant density) fluid:

$$\nabla \cdot (\rho \mathbf{U}) = 0 \tag{2.25}$$

$$\frac{\partial(\rho \mathbf{U})}{\partial t} + \nabla \cdot (\rho \mathbf{U}\mathbf{U} + \rho\overline{\mathbf{u}'\mathbf{u}'}) = -\nabla P - \nabla \cdot \bar{\tau} + \rho\bar{\mathbf{f}} \tag{2.26}$$

where the capital letters indicates a time-averaged value, $\mathbf{u}'$ is the fluctuating velocity. The terms appearing in Equation (2.26) resemble those in Equation (2.7) except for an additional term appearing on the left-hand side. This extra term acts as apparent

stresses due to turbulent motions and are called *Reynolds stress tensor* or turbulent stress tensor and defined as:

$$\tau_{ij} = \rho\overline{u_i' u_j'}. \tag{2.27}$$

The Reynolds-averaged form of conservation equation for a general variable ϕ can be written as:

$$\frac{\partial(\rho\Phi)}{\partial t} + \nabla \cdot (\rho \mathbf{U}\Phi + \rho\overline{u'\phi'}) = -\nabla \cdot (\bar{j}_\phi) + \bar{S}_k \tag{2.28}$$

where the additional term appearing on the left-hand side represents turbulent transport of ϕ.

The Reynolds tensor is symmetric and it represents correlations between fluctuating velocities. It is an additional stress term due to turbulence (fluctuating velocities) and it is unknown. This is called the *closure problem*: the number of unknowns (ten: three mean velocities, mean pressure and six Reynolds stresses) is larger than the number of equations problem (four: the continuity equation and three components of the Navier-Stokes equations). Similarly, for a general scalar variable, ϕ, there is one conservation equation and four unknowns (mean value of general variable, Φ , and three turbulent fluxes $\overline{u'\phi'}$).

A *turbulence model* is a set of equations which express relations between unknown terms appearing in Reynolds-averaged governing equations with known quantities.

2.6.2 Turbulence models for RANS

RANS-based turbulence models can be grouped into three classes: one which uses the concept of turbulent or eddy viscosity and another two which do not. Models pertaining to these classes are:

- *Eddy-viscosity models (EVM)*:
  - Algebraic models or zero-equation turbulence models;
  - One equation models;
  - Two equation models;
- *Non-linear eddy-viscosity models (NLEVM);*
- *Differential stress models (DSM).*

2.6.3 Eddy viscosity models

The Eddy Viscosity/Diffusivity Models (EVM) are based on the Boussinesq (1877) assumption that the turbulent stress tensor can be expressed in terms of the mean rate of strain in the same way as viscous stress for Newtonian isotropic fluid, except that the coefficient of the molecular viscosity is replaced by eddy viscosity. Thus:

$$-\overline{\rho u_i' u_j'} = \mu_T \left(\frac{\partial U_i}{\partial x_j} + \frac{\partial U_j}{\partial x_i} \right) - \frac{2}{3}\delta_{ij} \left(\mu_T \frac{\partial U_k}{\partial x_k} + \rho k \right). \tag{2.29}$$

Here μ_T is referred to as turbulent or eddy viscosity, which, in contrast to molecular viscosity, is not a fluid property but depends on the local state of flow or turbulence. It is assumed to be a scalar and may vary significantly within the flow domain. While k is the turbulent kinetic energy (normal turbulent stresses) and can be expressed as

$$k = \frac{1}{2}\overline{u_i' u_i'} = \frac{1}{2}(u'u' + v'v' + w'w'). \tag{2.30}$$

Substitution of Equation (2.29) in the Reynolds-averaged momentum conservation equations (Equation (2.26)) leads to a closed set, provided the turbulent viscosity is known. The form of the Reynolds-averaged momentum equations remain identical to the form of the laminar momentum equations (Equation (2.7)) except that molecular viscosity is replaced by an effective viscosity, μ_{eff}:

$$\mu_{eff} = \mu + \mu_T. \tag{2.31}$$

This approach is computationally very convenient since the same algorithm and computational code can be used for both laminar and turbulent transport phenomena without having to make any modification. The problem of closure remains, however, except that now it is reduced to define the eddy viscosity and diffusivity coefficients.

By analogy with the kinetic theory of gases, turbulent viscosity may be related to the characteristic velocity and length scales of turbulence (u_T and l_T respectively):

$$\mu_T \propto \rho u_T l_T. \tag{2.32}$$

The turbulence models then attempt to develop suitable methods/equations to estimate these characteristic length and velocity scales to close the set of equations.

Several different models have been developed. Excellent reviews describing the relative merits and demerits of models pertaining to this class are available (Launder & Spalding 1972, Rodi 1984, Markatos 1986, Nallaswamy 1987).

Most simple models, called zero equation models, estimate characteristic length and velocity scales by algebraic equations. Prandtl (1925) proposed a mixing length hypothesis for two-dimensional boundary layer flows which relates turbulent viscosity to velocity gradient:

$$\mu_T = \rho l^2 \left| \frac{\partial U}{\partial y} \right|. \tag{2.33}$$

This hypothesis works surprisingly well for many boundary layer flows. Prandtl suggested the estimation of characteristic length (mixing length) of turbulence (l) by postulating it to be proportional to the distance from the nearest wall.

Various modifications of the mixing length definition have been proposed in the past to account for pressure gradient, wall suction and blowing, flow curvature and rotation, but each was tuned for a specific application.

The mixing length theory assumes that the turbulent transport processes can be described in terms of only one parameter, the mixing length, which is defined solely in terms of flow geometry and takes no account of the turbulence intensity, nor of eddy size and structure. However, the turbulence is not a local phenomenon, but evolves in time and depends on the boundary conditions.

It should be noted that the mixing length theory provides a very simple and computationally convenient way of closing the turbulence problem. However, as it was shown in a few very simple flow examples, each problem requires a different empirical coefficient, which has to be determined from experiment. Besides, in more complex flows it is practically impossible to define in a unique manner the variation of the mixing length. This, and a lack of physical foundation (turbulence eddy structure is

very different from the molecular structure of a gas) has lead to the abandonment of the mixing length concept in practical computation.

An obvious choice for defining u_T is to use the turbulent kinetic energy k (Equation (2.30)) (Kolmogorov 1941, Prandtl 1942), so that

$$\mu_T = k^{1/2}. \tag{2.34}$$

It is noted that $k^{1/2} = \sqrt{\frac{1}{2}(\overline{u'^2} + \overline{v'^2} + \overline{w'^2})}$ is used as a measure of the averaged turbulence intensity. A transport equation for k can easily be derived, the unknown terms need to be modelled, but the equation remains relatively simple and easy to resolve. Defining and providing adequate length scale l_T is more difficult and uncertain. While all models use $k^{1/2}$ as a velocity scale, many variants of models can be found in literature differing in l_T.

Two basic classes of differential EVMs can be distinguishes, depending on how many differential equation need to be solved to provide eddy viscosity ν_T:

- One-equation models (only the differential transport equation for k is solved, whereas l_T is defined algebraically, usually in terms of flow geometrical parameters, in a similar manner as mixing length);
- Two-equations models: in addition to k-equation, another differential transport equation is solved which provides the characteristic turbulence length scale l_T, either directly, or in combination with k.

One-equation models have been popular in some branches of engineering, primarily in aeronautics for computing the flows around aircraft wings, fuselage, and even around the complete airplane. The best known one-equation models are Cebeci and Smith (1967), Baldwin and Lomax (1978), Norris and Reynolds (1975) and more recently Spalart and Almares (1992).

Along with the Spalart-Allmaras model, two-equation models make up the bulk of the turbulence models used for production CFD.

There are several different two-equation models proposed in the literature. The most popular are the $k-\varepsilon$ model, the $k-\omega$ model and the SST model. The latter is briefly presented in the next section and it is the one used in this work.

2.6.4 SST model

The SST (Shear Stress Transport) model of Menter (1994) is an eddy-viscosity model which includes two main novelties:

1. it is combination of a $k-\varepsilon$ model (in the inner boundary layer) and $k-\omega$ model (in the outer region of and outside of the boundary layer). A blending function is adopted to bridge these two models;
2. a limitation of the shear stress in adverse pressure gradient regions is introduced.

The $k-\varepsilon$ model is based on the solution of equations for the turbulent kinetic energy, k , and the turbulent dissipation rate, $\boldsymbol{\varepsilon}$. It has two main weaknesses: it over-predicts the shear stress in adverse pressure gradient flows because of too large length scale (due to

too low dissipation) and it requires near-wall modification (i.e. low-Re number damping functions/terms).

The $k-\omega$ model is based on the solution of equations for the turbulent kinetic energy, k , and the specific dissipation rate, $\boldsymbol{\omega}$. It is better at predicting adverse pressure gradient flow and the standard model of Wilcox (1988) does not use any damping functions. However, the disadvantage of the standard $k-\omega$ model is that it is dependent on the free-stream value of ω (Menter 1992).

In order to improve both $k-\varepsilon$ and $k-\omega$ model, Menter (1994) suggested to combine the two models. The equations of the Wilcox $k-\omega$ model are multiplied by a blending function f_1, and the transformed $k-\varepsilon$ equations are multiplied by the function 1-f_1. Then the corresponding turbulent kinetic energy k equation and the turbulent frequency ω equation are obtained to form the SST model:

$$\frac{\partial \rho k}{\partial t}+\frac{\partial}{\partial x_i}(\rho u_i k)=\frac{\partial}{\partial x_i}\left[(\mu_L+\sigma_k\mu_T)\frac{\partial k}{\partial x_j}\right]+\tau_{ij}S_{ij}-\beta^*\rho\omega k \tag{2.35}$$

$$\begin{aligned}\frac{\partial \rho \omega}{\partial t}+\frac{\partial}{\partial x_i}(\rho u_i \omega)=\frac{\partial}{\partial x_j}\left[(\mu_L+\sigma_\omega\mu_T)\frac{\partial \omega}{\partial x_j}\right]+\\ \frac{C_\omega\rho}{\mu_T}\tau_{ij}S_{ij}-\beta\rho\omega^2+2(1-f_1)\frac{\rho\sigma\omega^2}{\omega}\frac{\partial K}{\partial x_j}\frac{\partial \omega}{\partial x_i}\end{aligned} \tag{2.36}$$

where ρ is the density of fluid, k and ω are the turbulent kinetic energy and its dissipation frequency, respectively. The terms on the right-hand side of Equation (2.36) represent conservative diffusion, eddy-viscosity production and dissipation, respectively. Furthermore, the last term in the ω-equation describes the cross diffusion.

The turbulent eddy viscosity in Equations (2.35) and (2.36) is obtained from

$$\mu_T=\frac{a_1\rho k}{\max(a_1\omega,\ f_2||curl\mathbf{u}||_2)}. \tag{2.37}$$

This definition of the turbulent viscosity guarantees that in an adverse pressure gradient boundary layer, where the production of k is larger than its dissipation ω (hence $a_1\omega<||curl\mathbf{u}||_2$), Bradshaw's assumption, i.e., $\tau=a_1\rho k$ (shear stress proportional to turbulent kinetic energy) is satisfied.

The function f_1 in Equation (2.36), which blends the model coefficients of the $k-\omega$ model in boundary layers with the transformed $k-\varepsilon$ model in free-shear layers and freestream zones, is defined as

$$f_1=\tanh(arg_1^4) \tag{2.38}$$

$$arg_1=\min\left[\max\left(\frac{k^{0.5}}{0.09\omega d},\frac{500\mu_L}{\rho\omega d^2}\right),\frac{4\rho\sigma_{\omega 2}k}{CD_{k_\omega}d^2}\right] \tag{2.39}$$

where d stands for the distance to the nearest wall and CD_{k_ω}, is the positive part of the cross-diffusion term in Equation (2.36), i.e.,

$$CD_{k_\omega}=max\left(2\rho\frac{\sigma_{\omega 2}}{\omega}\frac{\partial k}{\partial x_i}\frac{\partial \omega}{\partial x_i},\ 10^{-20}\right). \tag{2.40}$$

The auxiliary function f_2 in Equation (2.37) is given by

$$f_2=\tanh(arg_2^2) \tag{2.41}$$

$$arg_2^2 = max\left(\frac{2\sqrt{k}}{0.09\omega d},\ \frac{500\mu_L}{\rho\omega d^2}\right). \tag{2.42}$$

The model constants are as follows

$$a_1 = 0.31,\ \beta^* = 0.09,\ \kappa = 0.41. \tag{2.43}$$

Finally, the coefficients of the SST turbulence model $\beta, C_\omega, \sigma_k$, and σ_ω are obtained by blending the coefficients of the $k-\omega$ model, denotes as ϕ_1, with those of the transformed $k-\varepsilon$ model (ϕ_2). The corresponding relation reads

$$\phi = f_1\phi_1 + (1-f_1)\phi_2. \tag{2.44}$$

The coefficients of the inner model ($k-\omega$) are given by

$$\sigma_{k1} = 0.85, \sigma_{\omega_1} = 0.5, \beta_1 = 0.075, C_{\omega 1} = \beta_1/\beta^* - \sigma_{\omega 1}\kappa^2/\sqrt{\beta^*} = 0.533. \tag{2.45}$$

The coefficients of the outer model ($k-\varepsilon$) are defined as

$$\sigma_{k2} = 1.0, \sigma_{\omega_2} = 0.856, \beta_2 = 0.0828, C_{\omega 2} = \beta_2/\beta^* - \sigma_{\omega 2}\kappa^2/\sqrt{\beta^*} = 0.440. \tag{2.46}$$

The boundary conditions for the kinetic turbulent energy and the specific dissipation at solid walls are

$$k = 0 \quad \text{and} \quad \omega = 10\frac{6\mu_L}{\rho\beta_1(d_1)^2} \tag{2.47}$$

with d_1 being the distance of the first node (cell centroid) from the wall. The grid has to be refined such that $y^+ < 3$.

2.7 LES turbulence models

Large Eddy Simulation (LES), originally proposed in 1963 for modelling of atmospheric flows (Smagorinsky 1963), was for the first time successfully applied to industrial flows as early as in 1970 (Deardorff 1970). LES provides a compromise between DNS, where al scales of turbulence are computed directly from the Navier-Stokes equations, and RANS equations, where all scales of turbulence must be modelled. The basic assumption of the LES method is separation of the continuous spectrum of eddy scales into resolved (i.e. computed) and modelled scales. It means that turbulent flow quantities like velocity, pressure, etc. are computed for scales comparable to the mesh size of the computational grid, while the same quantities resulting from scales smaller than the mesh size are being modelled. This assumption correctly reflects one of the basic features of turbulence, i.e. the tendency towards isotropy in small scales, which allows one to expect a much better chance for reliable modelling within this range of scales. On the other hand, the anisotropy, which prevails in larger scales, may properly be resolved in LES computed solutions, provided of course that a properly universal subgrid turbulence model may be found.

The separation of scales is achieved by filtration performed with the use of $G(x)$ filter, that allows one to transform an arbitrary flow-field quantity $F(x)$ to its filtered form $\overline{\overline{F}}(x)$, which is then being resolved numerically. The filtration procedure may be written as a convolution, which, for a simple one-dimensional case, may be written as

$$\overline{\overline{F}}(x) = G(x) * F(x) = \int_0^{+\infty} G(x-\xi)F(\xi)d\xi \tag{2.48}$$

where the symbols ($\bar{\cdot}$) and $*$ denote the result of the filtration and convolution operators, respectively.
Application of the above filtration procedure to N-S equations transforms them into the following from

$$\frac{\partial \overline{\overline{u}}_i}{\partial t} + \frac{\partial (\overline{\overline{u}}_i \cdot \overline{\overline{u}}_j)}{\partial x_j} = -\frac{1}{\rho}\frac{\partial \overline{\overline{p}}}{\partial x_i} + \frac{\partial}{\partial x_j}\left[\nu\left(\frac{\partial \overline{\overline{u}}_i}{\partial x_j} + \frac{\partial \overline{\overline{u}}_j}{\partial x_i}\right) - \tau_{ij}\right] \tag{2.49}$$

where one may notice the appearance of the so-called sub-grid stress tensor τ_{ij} which is given by the formula

$$\tau_{ij} = \overline{\overline{u_i u_j}} - \overline{\overline{u}}_i \cdot \overline{\overline{u}}_j. \tag{2.50}$$

Various subgrid-scale models were proposed in the past and the research still continues. The majority of the present models is based on the eddy-viscosity concept.
The viscosity-based models utilise the Boussinesq (Lesieur & Metais 1996) concept, transformed as follows

$$\tau_{ij} = \nu_t S_{ij} + \frac{1}{3}\tau_{ll} S_{ij} \tag{2.51}$$

where τ_{ij} denotes the subgrid stress tensor given by Equation (2.50), ν_t is the subgrid eddy viscosity coefficient, while the expression

$$S_{ij} = \frac{\partial \overline{\overline{u}}_i}{\partial x_j} + \frac{\partial \overline{\overline{u}}_j}{\partial x_i} \tag{2.52}$$

is the rate of the strain tensor of the filtered flow field. The first subgrid closure was proposed by Smagorinsky (1963), who developed a subgrid analogy to the mixing length model, given by the following formula

$$\nu_t = (C_s \Delta)^2 |S| \tag{2.53}$$

where Δ denotes the characteristic subgrid length scale (or filter width), C_s is a constant adjusted arbitrarily for a given flow type (solution), while the absolute measure of local strain is given by the formula

$$|S| = \sqrt{2 S_{ij} S_{ij}} \tag{2.54}$$

2.8 Multiphase flows

2.8.1 Introduction

A multiphase fluid is composed of two or more distinct components or 'phases' which themselves may be fluids or solids, and has the characteristic properties of a fluid. Within the discipline of multiphase flow dynamics the present status is quite different from that of the single phase flows. The theoretical background of the single phase flows is well established (the core of the theory being the Navier-Stokes equations as the previous section showed) and apparently the only outstanding practical problem that still remains unsolved is turbulence, or perhaps more generally, problems associated with flow stability. While it is rather straightforward to derive the equations of the conservation of mass, momentum and energy for an arbitrary mixture, no general counterpart of the Navier-Stokes equations for multiphase flows have been found (Hiltunen et al. 2009). Using a proper averaging procedure it is however quite possible to derive a set of "equations of multiphase flows" which in principle correctly

describes the dynamics of any multiphase system and is subject only to very general assumptions. The drawback is that this set of equations invariably includes more unknown variables than independent equations, and can thus not be solved. In order to close this set of equations, additional system dependent constitutive relations and material laws are needed. Considering the many forms of industrial multiphase flows, such as flow in a fluidized bed, bubbly flow in nuclear reactors, gas-particle flow in combustion reactors and fiber suspension flows within pulp and paper industry, it seems virtually impossible to deduce constitutive laws that would correctly describe interactions and material properties of the various phases involved, and that would be common even for these few systems. Furthermore, even in a laminar flow of, e.g., liquid-particle suspensions, the presence of particles induces fluctuating motion of both particles and fluid. Analogously to the Reynolds stresses that arise from time averaging the turbulent motion of a single phase fluid, averaging over this ”pseudo-turbulent” motion in multiphase systems leads to additional correlation terms that are unknown *a priori*. For genuinely turbulent multiphase flows, the dynamics of the turbulence and the interaction between various phases are problems that presumably will elude general and practical solution for decades to come. A direct consequence of the complexity and diversity of these flows is that the discipline of multiphase fluid dynamics is and may long remain a prominently experimental branch of fluid mechanics.

2.8.2 Fundamental forces in multiphase flow

Any fluid motion origins from forces acting on fluid elements. In general, forces can be classified in three different categories. Volume forces (also called body forces) act on a volume element of size $\mathcal{V} \propto L^3$, surface forces act on a surface or area element of a size $\mathcal{A} \propto L$, and line forces act on a curve element of size $\mathcal{C} \propto L$, where L is a linear dimension.

The pressure force acts on area o surface elements and tends to accelerate the fluid in direction of the pressure gradient. The inertial force is a volume force and tends to retain the actual direction and magnitude of the motion unchanged. The viscous force acts on a surface or area element and tends to make the flow field uniform and thus to diminish velocity differences. The gravity force tends to accelerate the fluid in direction of the gravity vector. Related to the gravity force is the buoyancy force, which is the difference between the gravity when the density is non-uniform. In two-phase flow the non-uniform density is due to the presence of different phases. The surface tension force acts on a line or curve element and tends to minimize the surface area of the interface. The surface tension is specific to gas-liquid or liquid-liquid two-phase flows (Wörner 2003).

2.8.3 Dispersed bubbly flows

The description of bubbly flows involves modelling of a deformable (gas-liquid) interface separating the phases; discontinuities of properties across the phase interface; the exchange between the phase; and turbulence modelling.

Most of the dispersed flow models are based on the concept of a domain in the static (Eulerian) reference frame for description of the continuous phase, with addition of a reference frame for the description of the dispersed phase. The dispersed phase may be

described in the same static reference frame as the continuous, leading to the Eulerian-Eulerian (EE) approach; or in a dynamic (Lagrangian) reference frame, leading to the Eulerian-Lagrangian (EL) approach. Multiphase modelling approaches are discussed in the next section.

2.8.4 Modelling approaches

The models for solving multiphase flow can generally be divided into three classes:

- Interphase tracking models;
- Eulerian-Lagrangian models;
- Eulerian-Eulerian models.

The interphase tracking models include among others level-set methods and Volume Of Fluid (VOF) methods. These methods accurately describe the interface between two phases, which is important for properly modeling for example the change in the shape of a rising bubble in quiescent liquid. The drawback is however that these methods require a high level of resolution both in grid and modeling in order to describe the interface properly, which requires large computational efforts. These methods are therefore not suitable for solving dispersed bubbly flows.

In the Euler-Lagrange approach, also called discrete bubble model (DBM), the fluid phase is treated as a continuum by solving the time-averaged Navier-Stokes equations, whereas the dispersed phase is solved by numerically integrating the equations of motion for the dispersed phase, i.e. computing the trajectories of a large number of particles or droplets through the calculated flow field. The dispersed phase consists of spherical particles that can exchange mass, momentum and energy with the fluid phase. Although the continuous phase acts on the dispersed phase through drag and turbulence while vice versa can be neglected, the coupling between the discrete and continuous phase can be included. The drawback is that the computational effort increases as the total number of particles to be tracked increases. This method is therefore only suited for solving dilute flows.

In the Eulerian-Eulerian approach, also called two-fluid model, the different phases are treated mathematically as interpenetrating continua. Since the volume of a phase cannot be occupied by the other phases, the concept of phasic volume fraction is introduced. These volume fractions are assumed to be continuous functions of space and time and their sum is equal to one. Conservation equations for each phase are derived to obtain a set of equations, which have similar structure for all phases. These equations are closed by providing constitutive relations that are obtained from empirical information.

Within the Eulerian-Eulerian approach, there are three methods: volume of fluid, mixture, and Eulerian. The volume of fluid model solves a single set of momentum equations for two or more fluids and tracks the volume fraction of each fluid throughout the domain. The mixture model solves for the momentum equation of the mixture and prescribes relative velocities to describe the dispersed phases. The Eulerian model solves momentum and continuity equations for each of the phases, and the equations are coupled through pressure and exchange coefficients.

In the present work, the flow in the simulated systems was modelled using the Eulerian approach due to its computational appropriateness at high dispersed phase contents.

2.8.5 Eulerian multiphase model

As already mentioned, in the Eulerian approach, the dispersed and continuous phases are assumed to be interpenetrating continua and for each phase a complete set of Navier-Stokes equations has to be solved.

For single-phase flows, rigorous basic transport equations are given in the form of mass, momentum and energy conservation (see Section 2.2). These equations are local, instantaneous equations and can be applied to all the volume and time domains under consideration. For multiphase flow processes, such local instantaneous field equations cannot be formulated without appropriate averaging. Several different averaging methods have been used. For example, Ishii (1975) and Drew (1983) used time averaging while Harlow and Amsden (1975), Rietema and van den Akker (1983) and Ahmedi (1987) used a volume averaging method. Besnard and Harlow (1988), Kataoka and Serizawa (1989) and Lahey and Drew (1989), among others, discussed various issues involved in the formulation of governing equations for multiphase flow processes. Recently, Enwald et al. (1996) discussed in detail the rigorous formulation of two-fluid model equations based on averaging techniques and corresponding closure laws.

2.8.5.1 Governing equations

In this section, the governing equations used in the numerical simulations, are presented without going into details of their derivation. As in the previous sections, the fluid in each phase is assumed to be incompressible and isothermal. Therefore energy balances are not required. Also the interfacial mass transfer between the water and gas phase is zero.

Phasic volume fractions describe the region occupied by each phase and are incorporated into the conservation equations for mass and momentum. The phasic volume fraction α must satisfy the relation:

$$\sum_{k=1}^{n} \alpha_k = 1 \tag{2.55}$$

where k is the total number of phases.

The conservation equations are written by performing an ensemble average of the local instantaneous balance for each phase (i.e. liquid and gas). The liquid is modelled as the continuous (primary) phase and the gas is modelled as the dispersed (secondary) phase.

The continuity equation for phase k is:

$$\frac{\partial}{\partial t}(\alpha_k \rho_k) + \nabla \cdot (\alpha_k \rho_k \mathbf{u}_k) = 0 \tag{2.56}$$

where ρ is the density and $\mathbf{u}$ is the velocity field. The right hand side is zero because applications in this research do not involve mass transfer or reactions.

The momentum equation for phase k is given by:

$$\frac{\partial(\alpha_k \rho_k \mathbf{u}_k)}{\partial t} + \nabla \cdot (\alpha_k \rho_k \mathbf{u}_k \mathbf{u}_k) = -\alpha_k \nabla p - \nabla \cdot (\alpha_k \bar{\bar{\tau}}_k) + \alpha_k \rho_k \mathbf{g} + \mathbf{M}_{I,k} \quad (2.57)$$

where p is the pressure shared for all phases, $\mathbf{g}$ is the gravity, $\bar{\bar{\tau}}_k$ is the stress tensor for phase k and the term $\mathbf{M}_{I,k}$ describes the interfacial forces. The interface term will be discussed later on.

The velocities in Equations (2.56) and (2.57) are defined as follows:

$$\mathbf{u}_k = \bar{\mathbf{u}}_k - \mathbf{u}'_k. \quad (2.58)$$

Here, $\mathbf{u}_k$ is the part of the velocity for phase k that will be resolved in the numerical simulations, $\bar{\mathbf{u}}_k$ is the instantaneous velocity and $\mathbf{u}'_k$ is the unresolved part of the numerical simulations. The interpretation of the terms $\mathbf{u}_k$ and $\mathbf{u}'_k$ depends on the method of derivation. When Equations (2.56) and (2.57) are obtained through ensemble averaging, then $\mathbf{u}_k$ and $\mathbf{u}'_k$ represent the mean velocity and the fluctuating velocity. When Equations (2.56) and (2.57) are obtained through a filtering operation, these terms are respectively the grid scale (GS) and the sub-grid scale (SGS) velocities (Deen 2001). When either ensemble averaging or filtering is used, unclosed parts occur in the stress term and in the interface forces. In this thesis, the unclosed part of the interface forces will be neglected.

The stress term of phase k is described as follows:

$$\bar{\bar{\tau}}_k = -\mu_{eff,k}(\nabla \mathbf{u}_k + (\nabla \mathbf{u}_k)^T - \frac{2}{3} I \nabla \cdot \mathbf{u}_k) \quad (2.59)$$

where $\mu_{eff,k}$ is the effective viscosity of phase k and I is the unit tensor.

2.8.5.2 Turbulence closure

The effective viscosity of the liquid phase $\mu_{eff,L}$ is modelled with three contributions as in the work of Deen (2001), molecular viscosity $\mu_{L,lam}$, shear-induced turbulent viscosity $\mu_{L,Tur}$ and an extra term due to bubble induced turbulence $\mu_{L,BIT}$:

$$\mu_{eff,L} = \mu_{L,lam} + \mu_{L,Tur} + \mu_{L,BIT}. \quad (2.60)$$

The effective viscosity of the gas phase is calculated as follows according to Jakobsen et al. (1997):

$$\mu_{eff,G} = \frac{\rho_G}{\rho_L} \mu_{eff,L}. \quad (2.61)$$

The turbulence induced by the movement of the bubbles is modelled as proposed by Sato & Sekoguchi (1975):

$$\mu_{L,BIT} = \rho_L C_{\mu,BIT} \alpha_G d_B \mid \mathbf{u}_G - \mathbf{u}_L \mid \quad (2.62)$$

where d_B is the bubbles diameter and $C_{\mu,BIT}$ is a model constant which is equal to 0.6.

The shear-induced turbulent viscosity in the liquid phase, $\mu_{L,Turb}$ is calculated using the chosen turbulence model. In this thesis two different models to calculate the turbulent viscosity are used: the LES model and the SST model.

When the SST model is used, the shear-induced turbulent viscosity in the liquid phase is formulated as follows:

$$\mu_{L,Tur} = C_\mu \rho_L \frac{k_L^2}{\varepsilon_L}. \quad (2.63)$$

The turbulent kinetic energy k and its energy dissipation rate ε are calculated from their conservation equations(Equations (2.35) and (2.36)).

When the LES is used, the model proposed by Smagorinsky (1963) is used to calculate the turbulent viscosity $\mu_{L,Tur}$

$$\mu_{L,Tur} = \rho_L (C_s \Delta)^2 |S| \tag{2.64}$$

where C_s is a model constant with a value of 0.1 and S is the characteristic filtered rate of strain and Δ is the filter width.

2.8.5.3 Interfacial forces

Interfacial force closure is one of the central topics in Eulerian multiphase flow modelling.

The motion of a single bubble with constant mass can be written according to Newton's second law:

$$m_b \frac{d\mathbf{u}}{dt} = \sum \mathbf{F}. \tag{2.65}$$

The bubble dynamics are described by incorporating all relevant forces acting on a bubble rising in a liquid. It is assumed that the total force, $\sum \mathbf{F}$ is composed of separate and uncoupled contributions originating from pressure, gravity, drag, lift, virtual mass and turbulent dispersion:

$$\sum \mathbf{F} = \mathbf{F}_P + \mathbf{F}_G + \mathbf{F}_D + \mathbf{F}_L + \mathbf{F}_{VM} + \mathbf{F}_{TD} + \mathbf{F}_{WL} + \mathbf{F}_{WD}. \tag{2.66}$$

For each force the analytical expression or a semi-empirical model is used, based on bubble behaviour observed in experiment or in DNS.

In this work the interface forces take into consideration, as in the work of Deen (2001), are drag, lift and virtual mass forces. Thus the term $\mathbf{M}_{I,k}$ in Equation (2.57), for the liquid (L) phase and the gas (G) phase is given as follows:

$$\mathbf{M}_{I,L} = -\mathbf{M}_{I,G} = \mathbf{M}_{D,L} + \mathbf{M}_{L,L} + \mathbf{M}_{VM,L}. \tag{2.67}$$

For an extensive discussion of these forces the reader is referred to the works of Jakobsen et al. (1997) and Delnoij et al. (1997).

The drag force is originated by the differences in velocities between the phases and is expected to have the largest influence in the momentum transfer between the gas and liquid phases. The drag force is given as:

$$\mathbf{M}_{D,L} = -\frac{3}{4} \alpha_G \rho_L \frac{C_D}{d_B} |\mathbf{u}_G - \mathbf{u}_L| (\mathbf{u}_G - \mathbf{u}_L). \tag{2.68}$$

Ishii & Zuber (1979) gave the following expression for the drag coefficient C_D in the case of distorted bubbles:

$$C_D = \frac{2}{3} E\ddot{o}^{1/2} \tag{2.69}$$

where $E\ddot{o}$ is the dimensionless Eötvös number ($E\ddot{o} = g\Delta\rho d_B^2/\sigma$).

In this thesis, in bubble column simulations, a bubble size of 4.0 mm is used, unless otherwise mentioned. This gives $E\ddot{o} = 2.2$ and $C_D = 1.0$. The bubble size was chosen based on the PIV observations of Deen et al. (2001).

The effect of shearing motion in the liquid phase on the movement of the gas-phase is modeled through the lift force:

$$\mathbf{M}_{L,L} = \alpha_G \rho_L C_L (\mathbf{u}_G - \mathbf{u}_L) \times \nabla \times \mathbf{u}_L \tag{2.70}$$

where C_L is a model constant, which is set to 0.5.

The acceleration of the liquid in the wake of the bubble is taken into account through the virtual mass force, which is given by:

$$\mathbf{M}_{VM,L} = \alpha_G \rho_L C_{VM} \left(\frac{D\mathbf{u}_G}{Dt} - \frac{D\mathbf{u}_L}{Dt} \right). \tag{2.71}$$

With C_{VM} a model constant with a value of 0.5. The D/Dt operators denote the substantial derivatives in the two phases.

Chapter 3 Numerical Methods

3.1 Overview

Mathematical models of flow processes, presented in Chapter 2, are non-linear, coupled partial differential equations (PDEs). Because of the coupled nature of the equations and the presence of non-linear terms, the fluid flow equations are generally not amenable to analytical method of obtaining the solution. In general, closed form analytical solutions are possible only if these PDEs can be made linear, either because non-linear terms naturally drop out (as in the case of parallel flows or flows that are inviscid and irrotational everywhere) or because the nonlinear terms are small compared to other terms so that they can be neglected (e.g., creeping flows, small amplitude sloshing of liquid etc.). If the non-linearities in the governing PDEs cannot be neglected, which is often the case for most engineering flows, one normally has to resort to numerical methods to obtain solutions.

An analytical solution to a partial differential equation gives the value of ϕ as a function of the independent variables (x, y, z, t). The numerical solution, on the other hand, aims to provide us with values of ϕ at a discrete number of points in the domain. The process of converting governing transport equations into a set of equations for the discrete values of ϕ is called discretization process and the specific methods employed to bring about this conversion are called discretization methods.

The discrete values of ϕ are typically described by algebraic equations relating the values at grid points to each other. The development of numerical methods focuses on both the derivation of the discrete set of algebraic equations, as well as a method for their solution. In arriving at these discrete equations for ϕ we will be required to assume how ϕ varies between grid points i.e., to make profile assumptions. Most widely used methods for discretization require local profile assumptions. That is, we prescribe how ϕ varies in the local neighbourhood surrounding a grid point, but not over the entire domain.

The conversion of a differential equation into a set of discrete algebraic equations requires the discretization of space. This is accomplished by means of mesh generation. Mesh generation divides the domain of interest into elements or cells, and associates with each element or cell one or more discrete values of ϕ. It is these values ϕ we wish to compute.

We should also distinguish between the discretized equations and the methods employed to solve them. For our purposes, let us say that the accuracy of the numerical solution, i.e., its closeness to the exact solution, depends only on the discretization process, and not on the methods employed to solve the discrete set (i.e., the path to solution). The path to solution determines whether we are successful in obtaining a solution, and how much time and effort it will cost us. But it does not determine the final answer.

Since we wish to get an answer to the original differential equation, it is appropriate to ask whether our algebraic equation set really gives us this. When the number of grid points is small, the departure of the discrete solution from the exact solution is expected to be large. A well-behaved numerical scheme will tend to the exact solution as the number of grid points is increased. The rate at which it tends to the exact solution depends on the type of profile assumptions made in obtaining the discretization. No matter what discretization method is employed, all well-behaved discretization methods should tend to the exact solution when a large enough number of grid points is employed.

This chapter reviews the operations required to achieve a numerical solution:

1. discretization of the domain;
2. from PDEs to discrete algebraic equations: spatial and temporal discretization;
3. from coupled unknowns to uncoupled unknowns: uncoupling;
4. from (huge) linear equation systems to their solution: linear solvers.

3.2 Discretization of the Domain: Grid Generation

The first step of every numerical simulations is the grid generation: the space, where the flow is to be computed – the physical space, is divided into a set of discrete sub-domains, or computational cells, or control volumes called grid or mesh.

The fundamental unit of the mesh is the cell (sometimes called the element). Associated with each cell is the cell centroid. A cell is surrounded by faces, which meet at nodes or vertices. In three dimensions, the face is a surface surrounded by edges. In two dimensions, faces and edges are the same. A variety of mesh types are encountered in practice which are briefly presented below.

3.2.1 Regular and Body-fitted Meshes

In many cases, our interest lies in analyzing domains which are regular in shape: rectangles, cubes, cylinders, spheres. These shapes can be meshed by regular grids, as shown in Figure 3.1(a). The grid lines are orthogonal to each other, and conform to the boundaries of the domain. These meshes are also sometimes called orthogonal meshes. For many practical problems, however, the domains of interest are irregularly shaped and regular meshes may not suffice. An example is shown in Figure 3.1(b). Here, grid lines are not necessarily orthogonal to each other, and curve to conform to the irregular geometry.

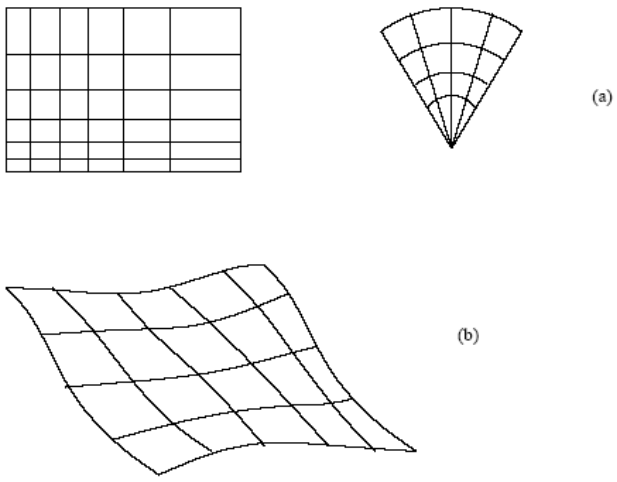

Figure 3.1: Regular and Body-Fitted Meshes

3.2.2 Structured, Block Structured, and Unstructured Meshes

The meshes shown in Figure 3.1 are examples of *structured* meshes. Here, every interior vertex in the domain is connected to the same number of neighbour vertices. Figure 3.2a shows a block-structured mesh. Here, the mesh is divided into blocks, and the mesh within each block is structured. However, the arrangement of the blocks themselves is not necessarily structured. Figure 3.2b shows an unstructured mesh. Here, each vertex is connected to an arbitrary number of neighbour vertices. Unstructured meshes impose fewer topological restrictions on the user, and as a result, make it easier to mesh very complex geometries.

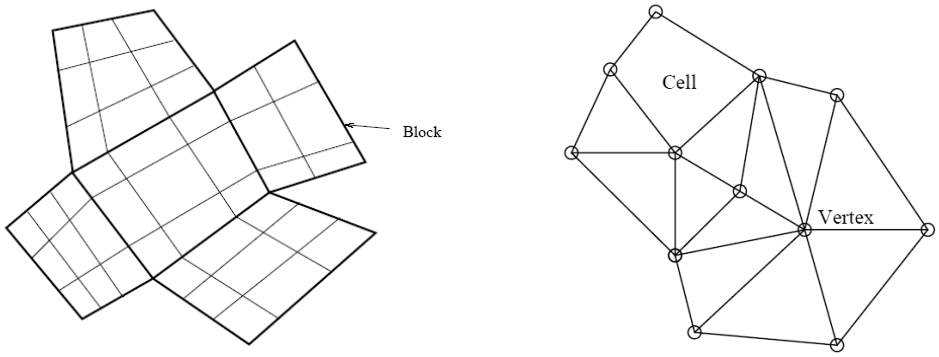

a) b)

Figure 3.2: a) Block-Structured Mesh, b) Unstructured Mesh

3.2.3 Conformal and Non-Conformal Meshes

An example of a non-conformal mesh is shown in Figure 3.3. Here, the vertices of a cell or element may fall on the faces of neighbouring cells or elements. In contrast, the meshes in Figure 3.1 and Figure 3.2 are conformal meshes.

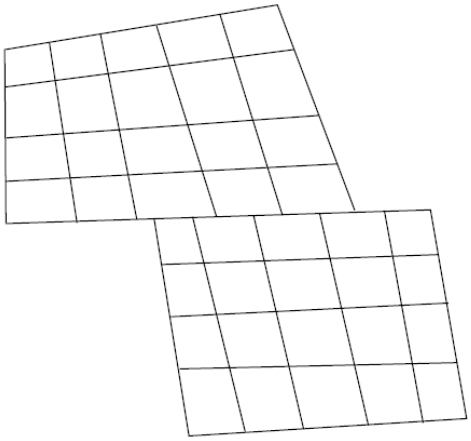

Figure 3.3: Non-Conformal Mesh

3.2.4 Cell Shapes

Meshes may be constructed using a variety of cell shapes. The most widely used are quadrilaterals and hexahedra. Methods for generating good-quality structured meshes for quadrilaterals and hexahedra have existed for some time now. Though mesh structure imposes restrictions, structured quadrilaterals and hexahedra are well-suited for flows with a dominant direction, such as boundary-layer flows. More recently, as computational fluid dynamics is becoming more widely used for analyzing industrial flows, unstructured meshes are becoming necessary to handle complex geometries. Here, triangles and tetrahedral are increasingly being used, and mesh generation techniques for their generation are rapidly reaching maturity. Another recent trend is the use of hybrid meshes.

3.3 Convection-Diffusion equation

Instead of considering the spatial and temporal discretization of each Navier-Stokes equations separately, it is useful to express each of them as a particular case of generic convection-diffusion equation. In three-dimensional Cartesian co-ordinates the convection-diffusion equation has the following expression:

$$\overbrace{\underbrace{S}_{\text{source term}}}^{\text{generation of } \phi} = \overbrace{\underbrace{\frac{\partial(\rho\phi)}{\partial t}}_{\text{transient term}}}^{\text{accumulation of } \phi} + \overbrace{\underbrace{\sum_{i=1}^{3}\left[\frac{\partial}{\partial x_i}(\rho u_i \phi)\right]}_{\text{convection term}} + \underbrace{\sum_{i=1}^{3}\left[\frac{\partial}{\partial x_i}\left(-\Gamma\frac{\partial\phi}{\partial x_i}\right)\right]}_{\text{diffusion term}}}^{\text{transport of } \phi}. \tag{3.1}$$

The use of a generic convection-diffusion equation is not only useful to simplify the distretization, but also provides information about the physical mining of the terms in the model. It is used to model the transport of a generic physic magnitude (momentum, energy or mass depending on the equation) in a continuous fluid medium with a velocity field $\mathbf{u} = (u, v, w)$, that in this point is assumed to be know. The changes in this generic magnitude are described in terms of ϕ, the unknown of the equation. It can stand for a variety of different quantities such as mass fraction or a velocity component.

None of the terms of the equation has a meaning in absence of the others. However, if they could be isolate, their role in the transport and generation of ϕ in a infinitesimally small control volume would be (using the energy equation as an example):

- the source term describe the generation of energy in the control volume;
- the transient term describe the energy accumulated;
- the convection term describe the flux of energy leaving the control volume due to the velocity $\mathbf{u}$ of the fluid medium;
- the diffusion term describe the energy flux leaving the control volume due to molecular diffusion. This process transports energy from point of higher energy to point of lower energy concentration, independently of the velocity $\mathbf{u}$.

Thus Equation (3.1) is simply a balance between the generation, accumulation and transport of a generic variable ϕ. The transport can be due to convection (associated to a macroscopic movement of the medium) or to diffusion (due to molecular diffusion).

The terms ϕ, Γ and S (generic unknown, generalized diffusion coefficient and source term) are to be changed depending on the equation, according to the Table 1

Table 1: Terms of the generic convection-diffusion equation

Equation	$\boldsymbol{\varphi}$	$\boldsymbol{\Gamma}$	$\boldsymbol{S}$
Mass conservation	1	0	0
x momentum conservation	u	μ	$-\frac{\partial p}{\partial x}$
y momentum conservation	v	μ	$-\frac{\partial p}{\partial y}$
z momentum conservation	w	μ	$-\frac{\partial p}{\partial z}$

If $\mathbf{u}$, Γ and C are independent of the transported variable ϕ, Equation (3.1) is a linear PDE.

This is not the case of any the governing flow equation. In fact momentum equations $\phi = u_j$ are clearly non-linear due to convective terms that for this case become $(\rho u_j \phi) = \frac{\partial}{\partial x_i}(\rho u_i u_j)$. We may think of momentum equations as convection-diffusion equations in which the components of the velocity themselves are being transported. S is also non-linear, as pressure gradient terms depend on $\mathbf{u}$ and buoyancy terms on T (coupled with $\mathbf{u}$).

The use of a generic expression for all the scalar equations, is a first step towards the numerical solution of the set. However, due to a number of reasons, such the use of staggered grids, in many CFD codes the discretization of each of the equations is implement in a separate function. Additionally, the mass conservation equation, (a first order and non-transient equation) is quite artificially expressed in terms of the general convection diffusion equation (second order and transient).

3.4 Spatial discretization

Several methods have been employed over the years to solve the Navier-Stokes equations numerically, including the finite difference (FDM), finite element (FEM),

spectral element, and finite volume (FVM) methods. The most common in commercially available CFD programs are: FVM (~80%) and FEM (~15%).
Only the finite control volume method will be considered in this work.

3.4.1 Finite Volume Method

In the FVM, discretized equations are obtained by integrating the governing transport equations over a finite control volume (CV).
There are several possibilities of defining the shape and position of the control volume with respect to the grid. Two basic approaches can be distinguished:

- *cell-centred* scheme (Figure 3.4a) - here the flow quantities are stored at the centroids of the grid cells. Thus, the control volumes are identical to the grid cells.
- *cell-vertex* scheme (Figure 3.4b) - here the flow variables are stored at the grid points. The control volume can then either be the union of all cells sharing the grid point, or some volume centred around the grid point. In the former case we speak of overlapping control volumes, in the second case of dual control volumes.

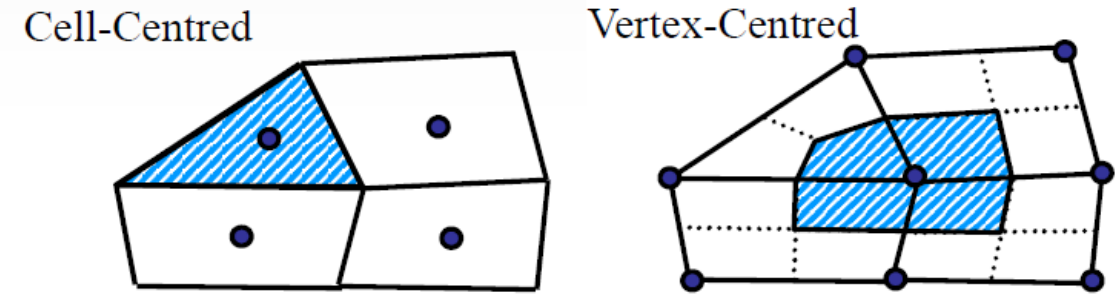

Figure 3.4: Cell-Centred and Vertex-Centre scheme

Before beginning the discretization, the generic convection-diffusion equation will be expressed in terms of a flux vector **J**. Equation (3.1) can be expressed using vectorial operators as:

$$\nabla \cdot (\rho \mathbf{u} \phi) - \nabla \cdot (\Gamma \nabla \phi) = S. \tag{3.2}$$

The total flux vector **J** is defined as

$$\mathbf{J} = \rho \mathbf{u} \phi - \Gamma \nabla \phi. \tag{3.3}$$

It is decomposed into a convective $\mathbf{J}^C$ plus a diffusive $\mathbf{J}^D$ fluxes:

$$\mathbf{J}^C = \rho \mathbf{u} \phi \tag{3.4}$$

$$\mathbf{J}^D = -\Gamma \nabla \phi. \tag{3.5}$$

Flux vector allows us to express Equation (3.2) as

$$\nabla \cdot \mathbf{J} = S. \tag{3.6}$$

Considering a cell-centre scheme, the approximated value of ϕ is evaluated for every node located inside each CV. Thus an algebraic, linear *discretization equation* will be obtained for each of the control volumes.

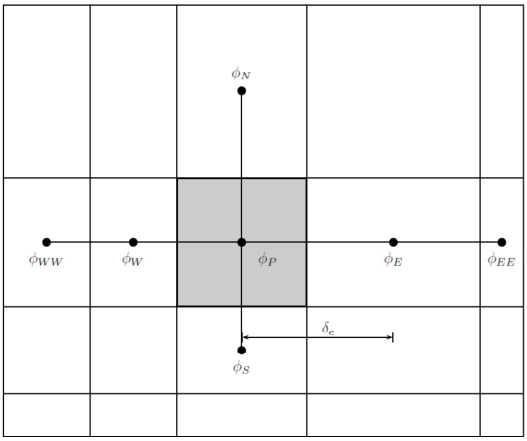

Figure 3.5: Fragment of a Cartesian structured two-dimensional mesh

The global set of linear equation will allow us to solve for each of the nodes. To do so, Equation (3.6), is integrated in each CV. For instance, considering a generic control volume filled in the Cartesian mesh shown in Figure 3.5

$$\int_{V_p} \nabla \cdot \mathbf{J} \, dv = \int_{V_p} S \, dv \tag{3.7}$$

At this point, V_p denotes the spatial region covered by the control volume. Using divergence theorem on the left hand side and expressing the right hand side in terms of the average of the source term, we obtain:

$$\int_{\partial V_p} \mathbf{J} \cdot \mathbf{n} \, ds = \bar{S} V_P \tag{3.8}$$

where V is the integrated volume, ∂V_p the outer surface of the control volume and $\mathbf{n}$ a unit vector normal to it. The left hand-side integral can be expressed as a sum of the contributions on each face. Assuming for simplicity a two-dimensional domain,

$$J_e - J_w + J_n - J_s = \bar{S} V_P \tag{3.9}$$

where J_f is the integral of the convective-diffusive flux of ϕ across cell face f (f = e, w, n or s). For instance,

$$J_e = \int_e \mathbf{J} \cdot \mathbf{n} \, ds = J_e^C + J_e^D \tag{3.10}$$

and $\bar{S}$ the averaged source term,

$$\bar{S} = \frac{1}{V_p} \int_{V_p} S dv \tag{3.11}$$

No approximations have been made so far. Equation (3.8) is still exactly equivalent to the set of integral equations over all the control volumes. The integral expressions (3.9) are *conservative:* they express the conservation principle for the unknown variable ϕ in the CV considered, as the differential equation expresses it for an infinitesimal CV. For any group of control volumes, including the whole computational domain, an integral conservation of quantities such as mass and momentum is satisfied even for coarse meshes. Thus, FVM is said to be conservative.

Next step is to express integral Equation (3.9) in terms of the unknown nodal values ϕ_E , ϕ_U, ϕ_N, ϕ_S, ϕ_P. to do this, two approximations are made:

1. consider flux vector **J** as a constant along each face and equal to the value at the central point of the face.
2. use a function profile to approximate the values of the flux vectors **J** at the central points of the interface as a function of the nodal values.

In order to preserve the conservative property of the method, the discretization has to be consistent, i.e., exactly the same expression has to be used to evaluate the convective and diffusive fluxes at the control volumes sharing an interface. Otherwise, a flux balance will be satisfied only in each CV but neither in groups of CVs nor in all the domain. It is convenient to treat convective and diffusive terms of **J** separately. using as an example the e face we proceed as follows:

- *Diffusive terms* are approximated using a second-order central difference scheme:

$$\begin{gathered}\int_e \mathbf{J}^D \cdot \mathbf{n} ds = \int_e -\Gamma \nabla \phi \cdot \mathbf{n} ds = \int_e -\Gamma \frac{\partial \phi}{\partial x} ds \approx \\ -\Gamma \left(\frac{\partial \phi}{\partial x}\right)_e S_e \approx -\Gamma S_e \frac{\phi_E - \phi_P}{\partial x_e} = D_e(\phi_P - \phi_E)\end{gathered} \quad (3.12)$$

Here the sub-index e denotes the central point of the east interface and $D_e = \frac{\Gamma_e S_e}{\delta e}$. This central-difference approximation, involving the central node ϕ_P plus four neighbours is second order accurate (if the interface is located midway of the discretization nodes). If the generalized diffusion coefficient Γ depends on the position, the value Γ_e has to be interpolated from the neighbouring values Γ_E and Γ_P. This can be either be due to non-homogeneous domains or to non-constant physical properties.

- *Convective terms* are approximated as:

$$J_e^C = \int_e \mathbf{J}^C \cdot \mathbf{n} ds = \int_e \rho \mathbf{u} \phi \cdot \mathbf{n} ds = \rho \int_e u_e \phi ds \approx \rho u_e \phi_e S_e = F_e \phi_e \quad (3.13)$$

where u_e is the component of $\mathbf{u}$ normal to the e face, evaluated in its central point, S_e is the surface of the e face and $F_e = \rho u_e S_e$ is the mass flow rate at the e face. In general, an interpolation has to done to evaluate F_e but this is not the critical point. The main problem is the evaluation of ϕ_e. It is considered to be a function of ϕ_P and its neighbouring nodes. For orthogonal meshes the values at the face are usually considered to be a function of the neighbours at the same axis, i.e.

$$\phi_E = f(\phi_{WW}, \phi_W, \phi_P, \phi_E, \phi_{EE}) \quad (3.14)$$

To avoid physically unrealistic flows, the function f has to be bounded by the node values used in its interpolation. Many differencing schemes are available, but the more accurate schemes tend to be less robust or slower. Three of the differencing schemes offered by the most common CFD software are described in the next section, of which the last two are used in this work.

- The *source term* $\bar{S}$ can be approximated in different ways. The most simple is to assume that the nodal value prevails over all the control volume,

$$\bar{S} = S_P. \quad (3.15)$$

In many case, the source term depends on ϕ. It is therefore beneficial to make the term 'at least nominally linear' (Patankar 1980) by expressing it as:

$$\bar{S}_\phi \Delta V = (S_{\phi_C} + S_{\phi_P}\phi_P)\Delta V. \tag{3.16}$$

The values of S_{ϕ_C} and S_{ϕ_P} should be chosen very carefully if the solution procedure is to succeed (see the four rules of Patankar (1980)). The most important point to note is that S_{ϕ_P} should be non-positive.

Combining the previous expressions, the discretized flux conservation equation can be written as:

$$(J_e^D + F_e\phi_e) - (J_w^D + F_w\phi_w) + (J_n^D + F_n\phi_n) - (J_s^D + F_s\phi_s) = S_P V \tag{3.17}$$

that can be expressed as a linear relation between ϕ_P and its neighbours:

$$a_P\phi_P = \sum_{nb} a_{nb}\phi_{nb} + b. \tag{3.18}$$

However, direct expansion of Equation (3.17) does not necessarily lead to acceptable coefficients for Equation (3.18).

The behaviour of numerical methods depends on the source term linearization employed and interpolation practices. Before discussing in more details some of the available discretization methods, a brief discussion of the desired characteristics of these methods will be useful. The most important properties of the discretization method are:

1. *Conservativeness*: To ensure the overall conservation of ϕ, the flux of ϕ leaving a CV across a given face, must be equal to the flux of ϕ entering the adjacent CV through the same face. Therefore, the flux through the common face must be represented by one and the same expression in adjacent CVs.
2. *Boundedness*: Numerical solution methods must respect the physically consistent bounds on variable values (bounded by minimum and maximum boundary values when there is no source). An essential requirement of boundedness is that all the coefficients of the discretized equation should be of the same sign and (usually) positive. If this condition is not satisfied, it is possible to observe unphysical 'wiggles' in the solution. It must also be noted that source term linearization practices (Equation (3.16)) should ensure that S_{ϕ_P} is always negative in order to possess the boundedness property (otherwise the value of a_P may become negative). Diagonal dominance of the discretized equations is a desirable feature for satisfying the 'boundedness' criterion. Scarborough (1958) gave a sufficient condition for diagonally dominant set of equations as:

$$\frac{\sum |a_{nb}|}{a_P} \begin{cases} \leq 1 & \text{at all nodes} \\ < 1 & \text{at least at one node} \end{cases} \tag{3.19}$$

   Diagonal dominance and all positive coefficients ensure boundedness. Special procedures are invoked to ensure the boundedness of many higher order schemes, which otherwise, may produce wiggles and unbounded solutions. Some of these methods are discussed in the following.

3. *Transportiveness*: Transportiveness can be illustrated by considering the distribution of ϕ in the vicinity of its source. The contours of constant ϕ are shown in Figure 3.6 for different values of Peclet number (ratio of strengths of convection and diffusion, $P_e = F/D$). For a process with zero Peclet number (pure diffusion), contours of constant ϕ are circular and therefore conditions at node P will be influenced not only by upstream conditions at W but also by all the conditions further downstream (node E). As the value of Peclet number increases (more convection), directionality of influence becomes increasingly biased towards the upstream direction. This means that conditions at node E are strongly influenced by those at P but conditions at P will experience only a weak influence from those at node E. At the extreme case of infinite Peclet number, the constant ϕ contours are completely stretched in the direction of flow and conditions at node E will not influence those at node P. Discretization schemes must respect the transportiveness properties (directionality of influence) of flow processes.

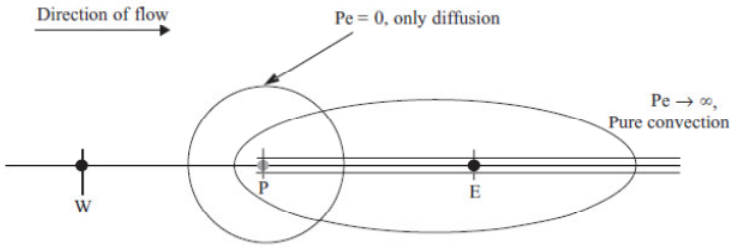

Figure 3.6: Distribution of ϕ around its source (Versteef & Malaalasekara 1995)

3.4.2 Discretization Schemes for convective terms

As introduced above, the accuracy, numerical stability and the boundness of the solution depend on the numerical scheme used to discretize convective terms. The central issue is the specification of an appropriate relationship between the convected variable, stored at the cell centre and its value at each of the cell faces. Among the numerous possible schemes, we will only consider three of them, which are simple and commonly used. Further information can be found in the specialized texts on finite volume methods.

As in the previous section, the methods of interpolation will be introduced using the two-dimensional Cartesian grid shown in Figure 3.5.

Central Differencing Scheme (CDS)

This is probably the most natural approach but is not very robust. The value of ϕ at a face is calculated from the mean of the values at the grid nodes on each side of the face. In terms of our example illustrated in Figure 3.5, this means:

$$\phi_e = \frac{\phi_P + \phi_E}{2} \tag{3.20}$$

This scheme is 2nd-order accurate, but is unbounded so that unphysical oscillations appear in regions of strong convection and also in the presence of discontinuities such

as shocks. One way to reduce these errors is to use a refined grid, but the best way is to use another differencing scheme.

There is one exception to this rule. Central differencing is the preferred discretization scheme when the LES turbulence model is used as was done during this research.

Upwind Differencing Scheme (UDS)

In this scheme, the value of ϕ at a face takes the value of ϕ at the upstream node. In our example, this means approximating by either ϕ_P or ϕ_E. In the upwind interpolation, the choice, P or E, is dictatedby the direction of the flow

$$\phi_e = \begin{cases} \phi_P & \text{if} \quad (\mathbf{V} \cdot \mathbf{n})_e > 0 \\ \phi_E & \text{if} \quad (\mathbf{V} \cdot \mathbf{n})_e < 0 \end{cases} \quad . \tag{3.21}$$

The UDS is unconditionally bounded and highly stable, but it is only 1st-order accurate in terms of truncation error and may produce severe numerical diffusion. The scheme is therefore highly diffusive when the flow direction is skewed relative to the grid lines.

Hybrid Differencing

This is a combination of upwind and central differencing, and is the most robust of the schemes described here. The scheme used depends on the relative magnitudes of convection and diffusion, given by the Peclet number for the face, Pe_f:

$$Pe_f = \frac{C_f}{D_f} \tag{3.22}$$

where: C_f is the convection coefficient at face f; D_f is the diffusion coefficient at face f ; and $f = n, s, e, w$.

If $|Pe_f| > 2$, convection dominates diffusion and upwind differencing is used, and when $|Pe_f| \leq 2$, diffusion becomes important and central differencing is used.

Hybrid differencing was used during this research when the RANS turbulence model is used.

3.4.3 Implementation of Boundary Conditions

Near the boundary of the computational domain, the boundary conditions should be incorporated into the integral balance equations for the cells and, thus, into the finite volume discretization. The special treatment concerns only the surface integrals over the faces lying on the boundary. The cumulative (convective plus diffusive) flux should be determined on the basis of the boundary conditions.

Let us consider the two-dimensional example shown in. One face lying on the boundary is e. We have to replace the surface integrals $-\int_e \rho \mathbf{u}\phi \cdot \mathbf{n} ds + \int_e \Gamma \nabla \phi \cdot \mathbf{n} ds$ by an integral that gives the flux due to the boundary conditions. For the Neumann condition, when the normal component of the boundary flux $\mathbf{q}$ is prescribed, this can be done in a straightforward manner. We simply replace the surface integrals by

$$-\int_e (\mathbf{q} \cdot \mathbf{n}) ds = -\int_e q_n ds \approx -q_{ne} S_e. \tag{3.23}$$

For the Dirichlet and mixed conditions, the flux is unknown and has to be approximated using the boundary conditions and values of ϕ at interior points.

For example, in the case of the Dirichlet condition, when ϕ at the Face e is prescribed, we assume that the flux is provided by a diffusive mechanism activated by the gradient of ϕ at the boundary. The boundary flux is

$$\int_e (\mathbf{q} \cdot \mathbf{n}) ds = -\int_e \Gamma \nabla \phi \cdot \mathbf{n} ds \approx -\Gamma \left(\frac{\partial \phi}{\partial n} \right)_e S_e. \tag{3.24}$$

To approximate the gradient of ϕ we can use the scheme of the first order

$$\left(\frac{\partial \phi}{\partial n} \right)_e \approx \frac{\phi_e - \phi_p}{|Pe|} \tag{3.25}$$

or the interpolation of higher order, which uses values of ϕ at more than one interior grid points.

3.5 Time discretization

After discretizing the spatial derivatives in the governing PDE's (such as the Navier-Stokes equations), we obtain a coupled system of nonlinear ODE's in the form

$$\frac{d\mathbf{u}}{dt} = \mathbf{F}(\mathbf{u}, t). \tag{3.26}$$

These can be integrated in time using a time-marching method to obtain a time-accurate solution to an *unsteady* flow problem. For a *steady* flow problem, spatial discretization leads to a coupled system of nonlinear algebraic equations in the form

$$\mathbf{F}(\mathbf{u}) = 0. \tag{3.27}$$

As a result of the nonlinearity of these equations, some sort of iterative method is required to obtain a solution. The major difference in the space and time co-ordinates lies in the direction of influence. In unsteady flows, there is no backward influence. The governing equations for unsteady flows are, thus, parabolic in time. Therefore, essentially all the numerical methods advance in time, in a step-by-step or 'marching' approach.

The methods for integration in time can be grouped into two major categories:

- explicit methods, which calculate the solution at the new time step by using only the variable values from previous steps;
- implicit methods, which use in the evaluation of the integral the unknown new values and thus require the solution of an equation system.

The explicit methods are thus much simpler and they require less storage and computing time per time step than the implicit methods. However, explicit methods suffer from instability if the time step is larger than a certain limit. Thus, they are not suitable for problem which do not require small time steps.

The most widely used methods for discretization of time derivatives are two-level methods. In order to facilitate further discussion, it is convenient to rewrite the basic governing equation as an ordinary differential equation with respect to time by employing the spatial discretization schemes discussed earlier:

$$\frac{d\phi}{dt} = f(t, \phi). \tag{3.28}$$

By integrating with respect to time between two grid points, one obtains:

$$\int_n^{n+1} \frac{d\phi}{dt} dt = \phi^{n+1} - \phi^n = \int_n^{n+1} f(t, \phi) dt. \tag{3.29}$$

Since the variation of ϕ with time is not known, some approximations are necessary to evaluate the integration of the function. Four commonly used approximations are detailed below.

Explicit Euler: Integral is evaluated using the value of ϕ available at the previous node:

$$\int_n^{n+1} f(t, \phi) dt = \Delta t \; f(t_n, \phi_n). \tag{3.30}$$

Implicit Euler: Integral is evaluated using the value of ϕ available at the next node:

$$\int_n^{n+1} f(t, \phi) dt = \Delta t \; f(t_{n+1}, \phi_{n+1}). \tag{3.31}$$

Mid-point rule: Integral is evaluated using the value of ϕ available at the midpoint:

$$\int_n^{n+1} f(t, \phi) dt = \Delta t \; f(t_{n+\frac{1}{2}}, \phi_{n+\frac{1}{2}}). \tag{3.32}$$

Trapezoid rule: Integral is evaluated using linear interpolation:

$$\int_n^{n+1} f(t, \phi) dt = \Delta t \frac{1}{2} [f(t_n, \phi_n) + f(t_{n+1}, \phi_{n+1}). \tag{3.33}$$

The first method is an explicit method while the remaining three are implicit methods (to varying degree). The Euler explicit and implicit methods are first-order accurate (errors are proportional to Δt) while the remaining two methods are second-order accurate (errors are proportional to Δt^2). Explicit methods have minimum requirements for memory and computations but are unstable at larger time steps. Implicit methods may require an iterative solution (and more memory) to obtain the values at the new time step but are much more stable. Apart from the two-level methods discussed here, there are multi-level methods such as the Runge–Kutta methods and Adams methods. Detailed discussion of these methods can be found in Press et al. (1992). For computational flow modelling, if the spatial discretization is second-order accurate, two-level methods for integration with respect to time will generally be sufficient, and are widely used. For special purposes, when higher order spatial discretization is used (for example, in large eddy simulations), higher order schemes can be used.

Here we discuss application of two-level methods to solve the generic unsteady transport equation (Equation (3.1)).

Integration of the transient term in Equation (3.1) over a computational cell and over a time interval can be written as:

$$\int \int_V \frac{\partial(\rho\phi)}{\partial t} dV \; dt = (\phi_P^{n+1} - \phi_P^n) \rho \Delta V. \tag{3.34}$$

The procedure for evaluating integrals of the remaining terms of Equation (3.1) over a control volume remain the same as discussed earlier. To evaluate integration with respect to time, it will be necessary to employ one of the two-level methods discussed above. As mentioned earlier, generally all the terms appearing in Equation (3.1) are linearized when carrying out discretization. Linearization simplifies the task of time

integration. Integration of ϕ with respect to time can then be written (considering the example of a term containing ϕ_E):

$$\int a_E \phi_E dt = a_E[\theta\phi_E^{n+1} + (1-\theta)\phi_E^n]\Delta t \tag{3.35}$$

where θ is a parameter controlling the degree of implicitness. Zero implies an explicit scheme, and one implies a fully implicit scheme (0.5 corresponds to the Crank–Nicholson scheme). Carrying out such a procedure for all terms of the governing transport equation, a discretized equation is obtained for the unsteady simulations:

$$\begin{aligned} a_P\phi_P^{n+1} = &\sum_{nb} a_{nb}[\theta\phi_{nb}^{n+1} + (1-\theta)\phi_{nb}^n] \\ &+ \left(a_P^0 - \sum_{nb}(1-\theta)a_{nb} + (1-\theta)S_P\right)\phi_P^n + S_{C\phi} \end{aligned} \tag{3.36}$$

where

$$a_P = \theta\sum_{nb} a_{nb} + a_P^0 - \theta S_{P\phi} \quad a_P^0 = \rho\frac{\Delta V}{\Delta t}. \tag{3.37}$$

For physically realistic and bounded results, it is necessary to ensure that all the coefficients of the discretization equation are positive. This requirement imposes restrictions on the time step that can be used with different values of θ. It can be seen that a fully implicit method with θ equal to unity is unconditionally stable. Detailed stability analysis is rather complex when both convection and diffusion are present. In general, simplified criteria may be used when an explicit method is used in practical simulations:

$$\Delta t < \frac{\Delta x_i}{u_i} \quad \text{or} \quad \frac{\Delta x^2}{2\Gamma_\phi}. \tag{3.38}$$

These criteria can be interpreted as no fluid particle (information) can propagate more than one grid length in a single time step. If the details of development from the initial guess to the final steady state are not important and only the final steady state is of interest, such a restriction on the time step may limit the rate of convergence. In such a case, implicit methods are advantageous. Since implicit methods are unconditionally stable, large time steps can be used and it might suffice to do a single iteration per time step. Such a pseudo-time-marching approach can be conveniently used to obtain steady state solutions to complex flow problems. Pseudo-time-marching is analogous to employing an under-relaxation. Pseudo-time-marching uses the same time step for all CVs, which is equivalent to using a different under-relaxation factor for each CV; use of a constant under-relaxation factor for all CVs is equivalent to applying a different time step for each CV.

3.6 Coupling

The discussion in the previous sections assumed that the velocity field required to calculate the necessary coefficients of the discretized equations was somehow known. However, generally, the velocity field needs to be calculated as part of the overall solution procedure by solving momentum conservation equations. The governing equations are discussed in Chapters 2. The basic momentum transport equations

governing laminar flow are considered here to illustrate the application of the finite volume method to calculation of the flow field. The governing equations can be written:

$$\frac{\partial}{\partial t}(\rho u) + \nabla \cdot (\rho u u) = -\nabla p + \nabla \cdot \left(\mu(\nabla u + \nabla u^T) + \left(\kappa - \frac{2}{3}\mu \right) \delta_{ij} \right) + \rho g. \quad (3.39)$$

It can be seen that since momentum equations are vector equations, the convective and diffusive terms in the equations appear more complicated than the generic transport equations discussed in the previous section. The convective terms are non-linear and the viscous terms contain more than one term. However, all of these terms can be discretized using the methods discussed in the previous section. All the extra non-zero terms not conforming to the generic equations are usually combined in the form of a source term. It must also be noted that all the three momentum equations are strongly coupled because each velocity component appears in all three momentum equations. This coupling can also be handled by the techniques of iterative solution discussed earlier. The unique feature of momentum equations, which distinguish them from the generic transport equation discussed earlier, is the role played by the pressure. The pressure gradients appear in the source terms of the momentum equations but there is no obvious equation to obtain the pressure. The pressure field is indirectly specified via the continuity equation. It is, therefore, necessary to calculate the pressure field in such a way that the resulting velocity field satisfies the continuity equation. Special treatments are needed to convert the indirect information in the continuity equation into a direct algorithm to calculate pressure (algorithms to treat pressure–velocity coupling). Some widely used algorithms are discussed in this subsection. Since the principal variable in momentum equations is a vector, it allows more freedom in the choice of variable arrangements on the grid.

3.6.1 Co-located and Staggered Grid Arrangement

Basic features of grids used for numerical solution are discussed in Section 3.2. When all the variables are stored at the same set of grid nodes, the arrangement is termed as ‘colocated’. It is, however, not necessary that all the variables share the same grid. It is possible, and sometimes advantageous, to use different locations for storing values of different velocity components and pressure (staggered grid). The two types of grid arrangement are shown in Figure 3.7. ‘Co-located’ seems to be an obvious choice, which has significant advantages in complicated solution domains. However, straightforward application of the finite volume method discussed earlier for momentum equations using the co-located grid fails to recognize the difference between a checkerboard pattern and uniform pressure fields. The staggered grid arrangement is proposed to suit the natural coupling of pressure and velocity. In this arrangement, the velocity field is stored at the faces of CV around a pressure node. In such an arrangement, the pressure and diffusion terms are very naturally approximated by a central difference approximation without interpolation. Also the evaluation of mass fluxes in the continuity equation (on the faces of a pressure CV) is straightforward. With a staggered grid arrangement, the natural coupling between pressure and velocity fields helps to avoid some types of convergence problems and oscillations in the pressure field. Because of these advantages, the staggered grid arrangement has been used extensively to solve momentum equations. In recent years, more and more problems with complex

geometry have been tackled using non-orthogonal grids. The staggered grid arrangement for equations in generalized coordinates is complicated because it introduces additional curvature terms, which are difficult to treat numerically. Thus, improved pressure–velocity coupling algorithms were developed which enable the use of co-located grids to solve momentum equations. Most commercial CFD codes now use co-located arrangements.

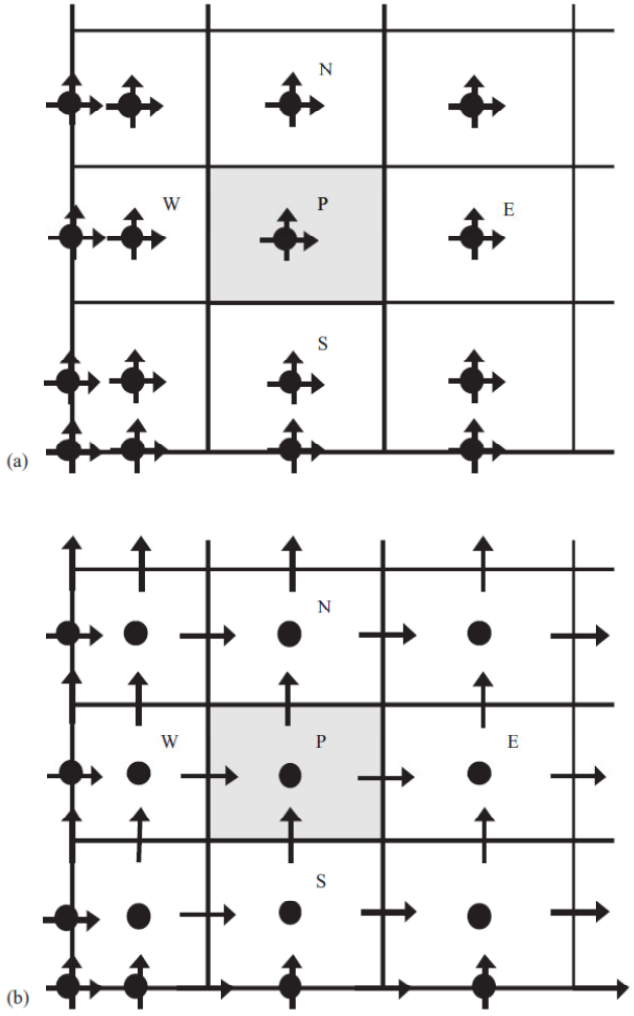

Figure 3.7: (a) Co-located and (b) Staggered grid arrangements (Renade 2002)

3.6.2 Algorithms to Treat Pressure–Velocity Coupling

The momentum and continuity equations can be combined to derive an equation for pressure. For example, for constant density and viscosity fluid, the continuity equation can be used to simplify the divergence of the momentum equation (Equation (3.39)) to yield an equation for pressure:

$$\frac{\partial}{\partial x_i}\left(\frac{\partial p}{\partial x_i}\right) = -\frac{\partial}{\partial x_i}\left[\frac{\partial(\rho u_i u_j)}{\partial x_j}\right]. \tag{3.40}$$

This elliptic pressure equation can be solved by the methods discussed earlier. It is important to note that the numerical approximations of this equation must be consistent with the approximations used in discretizing the original momentum and

continuity equations. For example, the outer derivative of pressure in Eq. (3.40) comes from the continuity equation, while the inner derivative arises from momentum equations. These outer and inner derivatives must be discretized using the corresponding schemes used for discretizing the continuity and momentum equations, respectively. Violation of this constraint may lead to incorrect solution of the continuity equation. To maintain consistency, generally the pressure equation is derived directly from the discretized momentum and continuity equations rather than approximating Equation (3.40). Several methods have been proposed to estimate the pressure field. The most widely used methods for incompressible flows, which are relevant to reactor engineering applications, are implicit or semi-implicit pressure correction methods. In these methods, pressure or pressure correction (or both) equations are derived from the discretized momentum and continuity equations, and used to enforce mass conservation at each iteration (or time step).

Here we will only discuss the SIMPLE (Semi-Implicit Pressure Linked Equations) algorithm, proposed by Patankar and Spalding (1972), which is one of the most common algorithms for the incompressible flow calculations. In this method, discretized momentum equations are solved using the guessed pressure field. The discretized form of the momentum equations can be written:

$$a_P u_{iP}^* = \sum a_{nb} u_{inb}^* + S_{u_i}^* - V_{Pi} \left(\frac{\delta p^*}{\delta x_i} \right) \tag{3.41}$$

where $(\delta / \delta x_i)$ indicates a discretized version of spatial derivative and * indicates the guess value or the value obtained from the previous iteration. V_{Pi} is the volume of CV around the node P. The velocity values obtained by solving these equations will not satisfy the continuity equation since the correct pressure field will not be known beforehand. In order to correct the fields obtained, SIMPLE proposes corrections of the form:

$$u_{iP} = u_{iP}^* + u_{iP}' \qquad p = p^* + p'. \tag{3.42}$$

The discretized versions of the momentum equations and Equation (3.42) lead to discretized equations in terms of velocity and pressure correction:

$$a_P u_{iP}' = \sum a_{nb} u_{inb}' - V_{Pi} \left(\frac{\delta p'}{\delta x_i} \right). \tag{3.43}$$

The corrected velocities are assumed to satisfy continuity equations. If the corrected velocity expressions (Equation (3.42)) are substituted in the discretized continuity equation, pressure correction equations can be derived. However, velocity corrections as given by Equation (3.43) involve velocity corrections at neighbouring nodes and unless some approximations are made, it is not possible to obtain the desired pressure correction equations. In SIMPLE algorithm, the first term comprising velocity corrections at the neighbouring nodes is neglected to yield a simplified expression for velocity corrections:

$$u_{iP}' = -\frac{V_{Pi}}{a_P} \left(\frac{\delta p'}{\delta x_i} \right). \tag{3.44}$$

For a staggered grid arrangement, velocity correction can be related to pressure corrections at the two nodes around it:

$$u'_e = \left(\frac{V_P}{a_P \delta x_i}\right)(p'_P - p'_E). \tag{3.45}$$

Substitution of this velocity correction into the discretized form of the continuity equation then leads to a pressure correction equation of the following form:

$$a_P p'_P = \sum a_{nb} p'_{nb} + S^*_M \tag{3.46}$$

where S_M is the mass imbalance and * indicates the value obtained from the currently available values of variables. The coefficients of this discretized equation, a_P and a_{nb}, can be obtained with the help of Equation (3.44). Equation (3.46) can be solved to obtain the pressure correction field. Once the pressure correction field is known, Equation (3.44) can be used to obtain velocity corrections. Equation (3.43) can then be used to obtain the corrected pressure and velocity field. The gross assumption of neglecting velocity corrections at the neighbouring nodes (first term of Equation ((3.43)), however, has detrimental consequences on the overall performance of the algorithm. The corrected pressure and velocity fields need to be under-relaxed in order to maintain the stability of the algorithm. Under-relaxation is a way to control the change in the variable values during the iterative processes. Such under-relaxation for the pressure and velocity field may considerably reduce the rate of convergence.

The SIMPLER (SIMPLE Revised) algorithm of Patankar (1980) is an improved version of SIMPLE. In this algorithm the discretized continuity equation is used to derive a discretized equation for pressure, instead of a pressure correction equation as in SIMPLE. Thus the intermediate pressure field is obtained directly without the use of a correction. Velocities are, however, still obtained through the velocity corrections of SIMPLE.

Van Doormal and Raithby (1984) proposed another variation of SIMPLE, called SIMPLEC (SIMPLE consistent). This method follows the same steps as the SIMPLE algorithm, with the difference that the momentum equations are manipulated so that the SIMPLEC velocity correction equations omit terms that are less significant than those omitted in SIMPLE.

The PISO algorithm, which stands for Pressure Implicit with Splitting of Operators, of Issa (1989) is a pressure-velocity calculation procedure developed originally for non-iterative computation of unsteady state problems. PISO involves one predictor step and two corrector steps and may be seen as an extension of SIMPLE, with a further corrector step to enhance it. Details of the derivation of this second correction equation may be found in Issa (1986) and Versteeg and Malalasekara (1995).

It must be noted that there is no single algorithm, which may be identified as the best algorithm for all types of problems. The performance of any algorithm depends on the flow conditions, the degree of coupling between various equations, the amount of under-relaxation used and sometimes, also on details of the numerical technique used to solve the algebraic equations (direction of sweeps and so on).

The solution algorithm for this class of methods can be summarized as follows:

1. Momentum equations are solved using the guessed (or available from the previous iteration) velocity and pressure field.
2. The pressure correction equation is solved and the velocity field is corrected using the derived pressure correction field. For PISO, a second pressure

correction equation is solved to correct the pressure and velocities again. For SIMPLER, the pressure equation is solved based on the updated velocity field.

3. Scalar equations (if any) are then solved using the corrected velocity field (for example, k and ε equations when solving the $k-\varepsilon$ model of turbulence or the enthalpy equation when solving non-isothermal flows).
4. Fluid properties are updated (if not constants).
5. Return to step 1 until a converged solution is obtained.

The algorithms discussed so far can be applied directly when staggered grids are used. For the co-located grid, however, some modifications to these algorithms are required to avoid oscillations in the pressure field. Although these oscillations can be filtered out (van der Wijngaart 1990), to devise a compact pressure correction equation similar to those discussed earlier, it is necessary to consider corrections to cell face velocities rather that node velocities (where the values are naturally available in co-located grids). The corrections to cell face velocities can be derived following the methods discussed earlier, the only difference is that the coefficients a_P in Equation (3.44) are not the nodal values, as in the staggered arrangement, but are interpolated cell centre values. This procedure may appear unnatural compared to direct application of the staggered arrangement, however, as already mentioned a co-located grid arrangement is preferable for flow simulations in complex geometry. Details of the derivation of pressure correction equations and application of SIMPLE-like algorithms to co-located grids may be found in Lilek and Peric (1995) and Ferziger and Peric (1995) among others.

3.7 Numerical solution to Algebraic Equations

Various discretization methods for partial differential equations have been described. Through this process, we obtain a system of linear or non-linear algebraic equations that need to be solve by some numerical methods. The complexity and size of this set of equations depend on the dimensionality and geometry of the physical problem. Whether the equations are linear or nonlinear, efficient and robust numerical methods are required to solve the system. There are essentially two families of numerical methods: direct methods and iterative methods.

Direct methods of solution of linear algebraic equations are essentially matrix inversion algorithms (Gauss elimination, LU decomposition etc. Details of these methods can be found in Press et al. 1992). These methods have large memory requirements and are computationally expensive for a large number of equations. These methods become especially inefficient when solving linearized non-linear equations.

Iterative methods are based on repeated application of a relatively simple algorithm (a Jacobi point by point method or line by line methods) leading to eventual convergence. If each iteration is inexpensive and the required number of iterations is small, an iterative method will be more efficient than the direct method. For many CFD problems, this is usually the case. The other advantage of iterative methods is that only non-zero coefficients of the equations need to be stored in core memory. In the next section only a brief overview of some of iterative methods is given.

3.7.1 Iterative methods

Iterative methods are the most widely used solution methods in computational fluid dynamics. These methods employ a guess-and-correct philosophy which progressively improves the guessed solution by repeated application of the discrete equations. Let us consider an extremely simple iterative method, the Gauss-Seidel method. The overall solution loop for the Gauss-Seidel method may be written as follows:

1. Guess the discrete values of ϕ at all grid points in the domain.
2. Visit each grid point in turn. Update ϕ using

$$\phi_P = \frac{a_E \phi_E + a_W \phi_W + b}{a_P} \tag{3.47}$$

   The neighbour values, ϕ_E and ϕ_W are required for the update of ϕ_P. These are assumed known at prevailing values. Thus, points which have already been visited will have recently updated values of ϕ and those that have not will have old values.
3. Sweep the domain until all grid points are covered. This completes one iteration.
4. Check if an appropriate convergence criterion is met. We may, for example, require that the maximum change in the grid-point values of ϕ be less than 01 %. If the criterion is met, stop. Else, go to step 2.

The iteration procedure described here is not guaranteed to converge to a solution for arbitrary combinations of a_P, a_E and a_W. Convergence of the process is guaranteed for linear problems if the *Scarborough criterion* is satisfied.

We note that direct methods do not require the Scarborough criterion to be satisfied to obtain a solution; we can always obtain a solution to our linear set of equations as long as our coefficient matrix is not singular.

The Gauss-Seidel scheme can be implemented with very little storage. All that is required is storage for the discrete values of ϕ at the grid points. The coefficients a_P, a_E , a_W and b can be computed on the fly if desired, since the entire coefficient matrix for the domain is not required when updating the value of ϕ at any grid point. Also, the iterative nature of the scheme makes it particularly suitable for non-linear problems. If the coefficients depend on ϕ, they may be updated using prevailing values of ϕ as the iterations proceed.

Nevertheless, the Gauss-Seidel scheme is rarely used in practice for solving the systems encountered in CFD. The rate of convergence of the scheme decreases to unacceptably low levels if the system of equations is large. Most of the common CFD software use a *multigrid method* to accelerate the rate of convergence of this scheme and make it usable as a practical tool.

It was developed in the 1960's in Russia by Fedorenko (1962) and Bakhvalov (1966). They applied multigrid for the solution of elliptic boundary-value problems. The methodology was further developed and promoted by Brandt (1977, 1981). The idea of multigrid is based on the observation that iterative schemes usually eliminate high-frequency errors in the solution (i.e., oscillations between the grid nodes) very effectively. On the other hand, they perform quite poor in reducing low-frequency (i.e., global) solution errors. Therefore, after advancing the solution on a given grid, it is

transferred to a coarser grid, where the low frequency errors become partly high-frequency ones and where they are again effectively damped by an iterative solver. The procedure is repeated recursively on a sequence of progressively coarser grids, where each multigrid level helps to annihilate a certain bandwidth of error frequencies. After the coarsest grid is reached, the solution corrections are successively collected and interpolated back to the initial fine grid, where the solution is then updated. This complete multigrid cycle is repeated until the solution changes less than a given threshold. In order to accelerate the convergence even further, it is possible to start the multigrid process on a coarse grid, carry out a number of cycle and then to transfer the solution to a finer grid, where the multigrid cycles are performed again. The procedure is then successively repeated until the finest grid is reached. This methodology is known as Full Multigrid (FMG)(Brandt 1981).

3.8 Boundary and initial conditions

To allow for a numerical treatment, first of all the domain has to be discretized, as explained above. After that, a PDE is solved over the domain with the use of a numerical method. An unambiguous solution of the PDEs is only possible provided that boundary conditions are specified. For an unsteady problem, in addition to the boundary conditions, also boundary conditions in time, i.e. the initial conditions have to be specified.

The numerical solution of the problem is significantly influenced by boundary and initial conditions, respectively. Even the best numerical algorithm will not help much, when boundary conditions are not specified appropriately, because they influence the solution at the boundary and often even deep into the computational domain. In so-called blind tests, which are contests where numerical modellers calculate flow problems without knowledge of the measured data, using the same program, typically very different correspondence with reality was achieved, depending on the ability of the modeller to set the boundary conditions adequately.

As for the initial conditions, the situation is somewhat different. Obviously, they have to be specified correctly, especially when the temporal evolution of the flow has to be correct from the beginning. However, the flow “forgets” the initial condition after some time. Often, the initial condition is of secondary importance, because only a final steady situation is of interest. In this case it is important to set physically meaningful initial conditions, so that the solution does converge, especially for the case of nonlinear flow problems. Often it is then meaningful to start from a known initial condition, which can for example be a flow at rest.

Chapter 4 Particle Image Velocimetry

4.1 Introduction

Experimental fluid mechanics has for a long time been used to visualize flow phenomenon. An early pioneer was Ludwig Prandtl who used aluminium particles in water flumes to describe the flow in a qualitative manner. In line with the rapid development of Computational Fluid Dynamics, CFD, the need for new validation tools has increased. By combining Prandtls attempt to trace particles and contemporary tools in laser and computer technologies a quantitative non intrusive whole field technique, so called Particle Image Velocity (PIV) has been developed. The PIV technique has been improved and grown in popularity through recent decades with the increase in computer capacity and it has rapidly spread in the world being recognized as the most advanced whole-flow-field-technique because of its strong merits. Its application ranges have been expanding to measure turbulent flow, multiphase flow, internal flow of fluid machines, bioengineering, medical engineering, environmental engineering, energy engineering, development of new materials, sports science, life science, robotics and so on. In this chapter an introduction of the PIV principles and the application of this method to two phase bubbly flow are given.

4.2 Principle of operation

The working principle of 2D PIV is quite simple and it is schematically described in Figure 4.1. The flow is seeded with light reflecting particles (tracer particles) which accurately follow the fluid motion and do not alter the fluid properties or flow characteristics. The tracer particles are illuminated by means of a thin light sheet generated from a pulsed light source (usually a double-head pulsed laser). The light scattered by them is recorded “via a high quality lens” either on a single frame (e.g. on a high-resolution digital or film camera) or on two separate frames on special cross-correlation digital cameras. Double frame mode is more commonly used and the remaining part of this introduction will deal with this acquisition method. The output of the digital sensor is transferred to the memory of a computer directly.

For the evaluation two subsequent images of the flow are divided into small subareas called “interrogation areas”. It is assumed that all particles within one interrogation area have moved homogeneously between the two illuminations. The volume-averaged displacement $\mathbf{s}_D(\mathbf{x}, t)$ of the particle images between the interrogation area in the first image and the interrogation area in the second image is determined by means of a cross-correlation analysis.

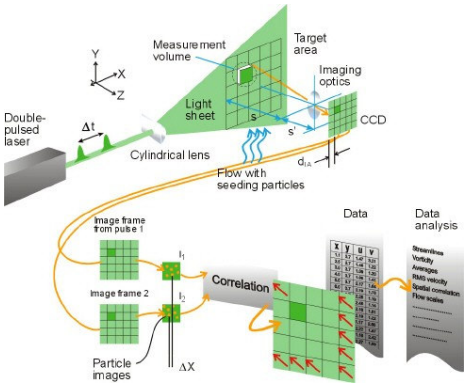

Figure 4.1: Experimental arrangement for PIV

When the interrogation areas contain a sufficient number of particle images, the cross-correlation consists of a dominant correlation peak embedded in a background of noise peaks, as illustrated in Figure 4.2.

The location of the tall peak, referred to as the displacement-correlation peak, corresponds to the particle-image displacement. The projection of the vector of the velocity in the interrogation area (two-component velocity vector), $\mathbf{u}(x,t)$, is then determined by dividing the measured displacement by the image magnification M_0 and the time delay Δt:

$$\mathbf{u}(x,t) = \frac{s_D(x,t)}{M_0 \Delta t}. \tag{4.1}$$

The process of interrogation is repeated for all interrogation areas of the PIV recording.

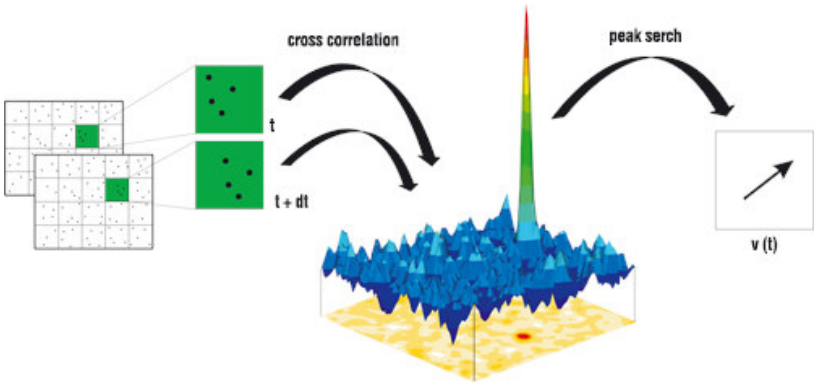

Figure 4.2: Graphical representation of the PIV process on a single interrogation area

4.3 Basic elements

4.3.1 Seeding

Seeding the flow with light reflecting particles is necessary in order to image the flow field. The tracer particles form the basis of the velocity measurement in PIV. The particles should be as small as possible so that they are able to closely follow the flow. However on the other hand, they may not be too small, because then they will not scatter enough light, and hence produce too weak images. Any particle that follows the flow satisfactorily and scatters enough light to be captured by the camera can be used. The number of particles in the flow is of importance in obtaining a good signal peak in

the cross-correlation. A good rule of thumb is that around ten particles should be correlated for each measured velocity vector.

4.3.2 Density of tracer particle images

Qualitatively three different types of image density can be distinguished (Adrian 1991). In the case of low image density, the images of individual particles can be detected and images corresponding to the same particle originating from different illuminations can be identified. Low image density requires tracking methods for evaluation. Therefore, this situation is referred to as "Particle Tracking Velocimetry", abbreviated "PTV". In the case of medium image density, the images of individual particles can be detected as well. However, it is no longer possible to identify image pairs by visual inspection of the recording. Medium image density is required to apply the standard statistical PIV evaluation techniques. In the case of high image density , it is not even possible to detect individual images as they overlap in most cases and form speckles. This situation is called "Laser Speckle Velocimetry" (LSV), a term which has been used at the beginning of the nineteen-eighties for the medium image density case as well, as the (optical) evaluation techniques were quite similar for both situations.

The working range of PIV can be distinguished from that of PTV and LSV through two parameters: the source density N_s and the image density N_I (Westerweel 1993; Adrian & Yao 1984). The source density indicates whether the image consists of individual particle images (i.e.$N_s \ll 1$), or that particle images overlap (i.e.$N_s \gg 1$). The source density is defined as follows:

$$N_S = C\Delta z_0 \frac{\pi d_\tau^2}{4M_0^2} \tag{4.2}$$

where C is the trace particle concentration [m^{-3}], Δz_0 [m] the light-sheet thickness, M_0 the image magnification and d_τ [m] the particle image size.

The image density is the average number of particle images per interrogation area. The image density is given as:

$$N_I = C\Delta z_0 \frac{\pi D_I^2}{M_0^2} \tag{4.3}$$

where D_I [m] is the interrogation size. PIV, PTV, LSV each have their own working ranges, which are given in Table 2.

Table 2: Working ranges for optical measurement techniques

PTV	PIV	LSV
$N_s \ll 1, N_I \ll 1$	$N_s \ll 1, N_I \gg 1$	$N_s \gg 1, N_I \gg 1$

4.3.3 Illumination

The illumination system of a PIV is always composed of light source and optics to shape the light source beam into a planar sheet to illuminate the flow field.

Light source

The particle tracers need to be illuminated and observed twice within the time separation. The first requirement for a light source suited for PIV experiments is a short duration of illumination δt. A practical criterion for the choice of the maximum duration of each illumination pulse is that particle images do not appear as streaks but rather as a circular dots. This is obtained when the (imaged) particle displacement within the pulse duration is significantly smaller than the size of the particle image itself:

$$\delta t \ll \frac{d_\tau}{\mathbf{v}M}. \tag{4.4}$$

The second requirement is that the illuminated particles are distributed within a thin sheet such that they can be imaged in focus and their position in depth is dictated by the laser sheet. A third requirement is that the intensity of the light source must allow the scattered light from the seeding particles to be detected by digital imaging devices. The required pulse energy E is proportional to the linear dimension L of the area of interest.

Lasers are widely used in PIV, because of their ability to emit monochromatic light with high energy density which can easily be bundled into thin light sheet for illuminating and recording tracer particles without chromatic aberrations.

Double-pulsed illumination is the current norm in PIV. The intensity of illumination required to form visible images of micrometer-sized particles usually requires the use of pulsed solid-state laser sources emitting pulses with energy between 5 and 500 mJ. The energy needed is closely coupled with the scattering properties of the particles.

Currently, solid-state Nd:YAG (Neodymium Yttrium Aluminum Garnet)(Figure 4.3) laser using frequency-doubling crystals to produce pulses at 532 nm are the most used. It produces pulse energies ranging between 10mJ and 1J. With its very short pulse duration (5-15 ns) this instrument is practically suited to illuminate flows without any limit on the flow speed.

The standard architecture of a PIV laser consists of two separate lasers firing independently at the required pulse separation. Therefore the time separation can be freely optimized for the experimental condition, primarily the flow speed and the imaging magnification.

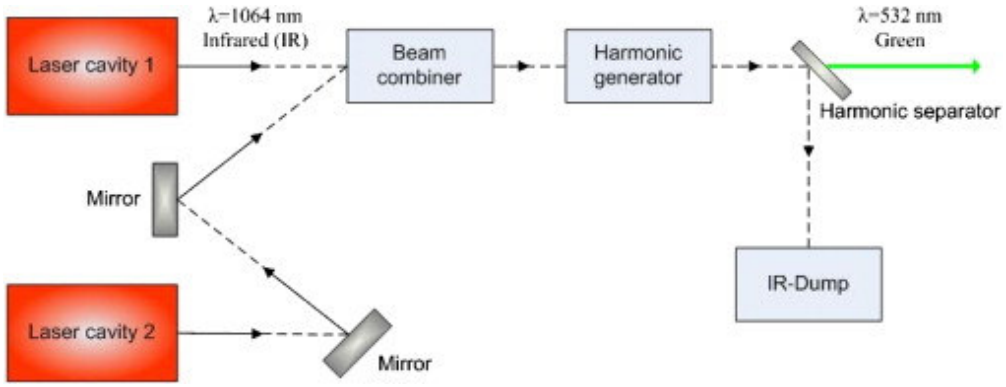

Figure 4.3: Double cavity Nd:YAG PIV-laser

Light sheet formation optics

The circular-cross-section beam delivery by the light source is shaped into a thin sheet by means of cylindrical and spherical lenses. Common arrangements are illustrate in Figure 4.4.

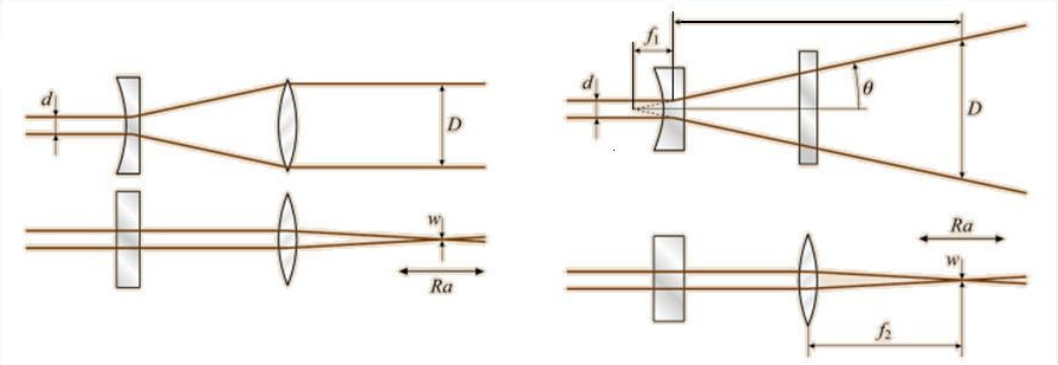

Figure 4.4: PIV optical configuration

4.3.4 Imaging

A schematic of the PIV optical configuration is shown in Figure 4.4. The light sheet has a finite thickness Δz_0 and is assumed to be uniform along the x and y directions. An image of the tracer particles in the light sheet is formed by means of a lens on the surface of an image sensor (usually a CCD or CMOS sensor array). We assume that the system consists of an aberration-free, thin circular lens, characterizes by its focal length f, aperture number $f^{\#}$ (given by the focal length divided by the aperture diameter D), and image magnification M_0, defined as the ratio of the image distance Z_0 and object distance z_0. The diameter d_τ of the image of a small tracer particle with diameter d_p in the light sheet (with wavelength λ) is given by:

$$d_\tau \cong (d^2 + M_0^2 d_p^2)^{1/2} \tag{4.5}$$

with

$$d_s = 2.44(1 + M_0) f^{\#} \lambda \tag{4.6}$$

where d_s is the diffraction-limited spot diameter and $M_0 d_p$ the geometric image diameter. The diffraction-limited spot results from the finite resolution for optical system due to diffraction effects; for a point source ($d_p \to 0$) or distant object $M_0 \to 0$ the light captured by the objective is spread over a small spot also known as the *Airy* disc, with diameter d_s, surrounded by diffraction rings of decreasing brightness (Raffel et al. 1998). For all practical porpoises in PIV, the light distribution in the Airy disc is well approximated by a Gaussian intensity with an e^2 diameter of $0.74 d_s$. The expression in (4.5) would be exact when the diffraction-limited spot and geometrical-optics particle image follow a Gaussian intensity distribution.

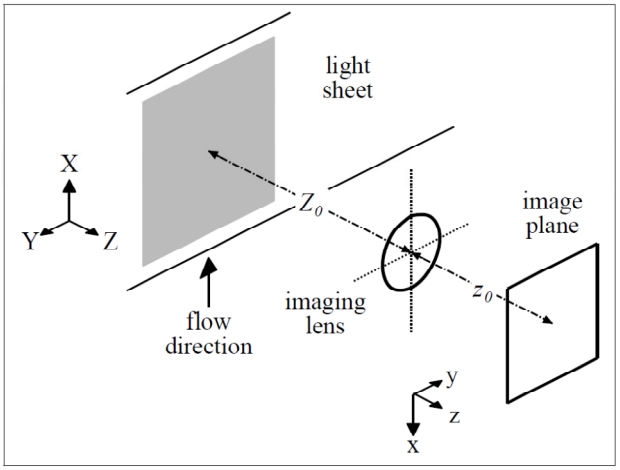

Figure 4.5: Schematic representation of imaging set-up in PIV

The particle-image diameter follows (4.5) for particle image in focus, i.e., when the light sheet thickness Δz_0 is smaller than the focal depth δz of the optical system (Figure 4.5) given by (Adrian 1991)

$$\delta z \approx 4\left(1+\frac{1}{M_0}\right)^2 f^{\#}\lambda. \tag{4.7}$$

4.3.5 Solid-state cameras

The popular trend nowadays is to use solid-state cameras, called digital cameras, as image recording media. These cameras record images on an electronic image sensor. Recent advances in electronic imaging have provided an attractive alternative to the photographic methods of PIV recording. Immediate image availability and thus feedback during recording as well as a complete avoidance of photochemical processing are a few of the apparent advantages brought about with electronic imaging.

Solid-state image sensors capture two-dimensional images on a planar, rectangular array of sensors, each sensor converting light energy to electrical energy and, ultimately, a digital word. Each sensor and its associated storage or electronics is called a pixel. For PIV, square pixels are preferred. The most common solid state sensor used in PIV are Charge Coupled Devices, or CCD, and Complementary Metaloxide Semiconductor (CMOS) devices.

4.3.6 Digital image processing

Digital image processing encompasses all computer operation on digital images. For a full account of all possible methods one is referred to the many text books that have been written on this subject (Gonzalez & Woods 2008, Pratt 2001, Castleman 1996). In general two approaches are distinguished in image processing (Tropea et al. 2007):

1. image restoration attempts to repair undesirable effects (e.g., perspective distortion, image blur due to defocusing);
2. image enhancement accentuates certain image feature (e.g., improvement of image contras, suppression of background illumination).

The interrogation analysis of PIV images by means of spatial correlation is based on the requirement that the image statistical properties are homogeneous, i.e., the image mean standard deviation are spatially uniform and the spatial correlation is a function of the difference of two spatial location. This implies:

1. homogeneous seeding;
2. uniform illumination;
3. uniform image background.

In many practical situation these requirements may not be fully met and some of these non-ideal aspects in PIV images can be compensated by means of image-processing methods.

4.4 Digital PIV evaluation

As mentioned above, the essential principle of PIV is to illuminate a seeded flow-field with two pulses of laser light and record the particle images. Traditionally, both exposures have been recorded on a single frame, creating a "double exposure." The double exposed frame is then processed using auto-correlation techniques. However, this leads to a directional ambiguity arising because the double exposed frame contains no information about which set of particle images were recorded from the first laser pulse, and which from the second. Image shifting using a rotating or spinning mirror can be used to overcome this ambiguity, but does increase experimental complexity.

A better alternative when using digital cameras is to record each of the two exposures on separate frames, followed by analysis based on cross-correlation of the two frames. Recording on separate frames preserves the time sequence of the pulses so no directional ambiguity occurs. Also, cross-correlation processing provides improved dynamic range for velocity compared with auto-correlation of double exposures.

4.4.1 Cross-correlation

The aim of the cross-correlation is to find the distance that the particle pattern has moved during the inter image time and translate this into a velocity measure.

From a signal (Figure 4.6) processing point of view, the first image may be considered the input to a system whose output produces the second image of the pair. The system's transfer function, $\mathbf{H}$, converts the input image I to the output image I' and is comprised of the displacement function $\mathbf{d}$ and an additive noise process, $\mathbf{N}$. The function of interest is a shift by the vector $\mathbf{d}$ as it is responsible for displacing the particle images from one image to the next.

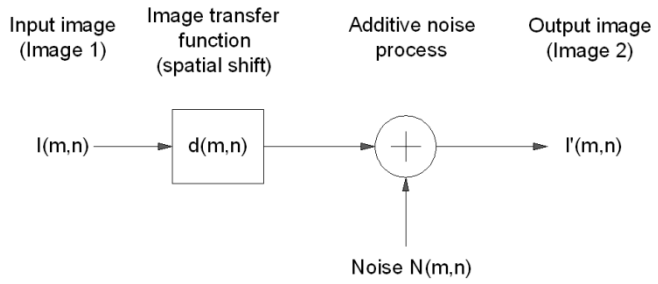

Figure 4.6: Idealize linear digital signal processing model describing the functional relationship between two successively recorded particle image frames (Reffael et al. 1998)

This function can be described, for instance, by a convolution with $\delta(\mathbf{x} - \mathbf{d})$. The additive noise, $\mathbf{N}$, models effects due to recording noise and three-dimensional flow among other things. If both $\mathbf{d}$ and $\mathbf{u}_i$ are known, it should be possible to use them as transfer function for the input image I to produce the output image I'. With both images I and I' known the aim is to estimate the displacement field $\mathbf{d}$ while excluding the effects of the noise process $\mathbf{N}$. The fact that the signals (i.e. images) are not continuous, that is, the dark background cannot provided any displacement information, makes it necessary to estimate the displacement field $\mathbf{d}$ using a statistical approach based on localized interrogation windows.

Rather than estimate the displacement field $\mathbf{d}$ analytically the method of choice is to locally find the best match between the images in a statistical sense. This is accomplished through the use of the discrete cross-correlation function, whose integral formulation is given by:

$$R_{II} = \sum_{i=-K}^{K} \sum_{i=-L}^{L} I(x,y)I'(i+x, j+y). \tag{4.8}$$

The variables I and I' are the sample (e.g. intensity values) as extracted from the images where I' is larger than the template *I*. Essentially the template I is linearly "shifted" around in the sample I' without extending over edge of I'. For each choice of sample shift (x,y), the sum of the products of all overlapping pixel intensities produces one cross-correlation value $R_{II}(x,y)$. By applying this operation for a range of shifts $(-M \leq x \leq +M, -N \leq y \leq +N)$ a correlation plane the size of $(2M+1) \times (2N+1)$ is formed. This is shown graphically in Figure 4.7.

For shift values at which the samples' particle image align each other, the sum of the product of pixel intensities will be larger than elsewhere, resulting in a high cross-correlation value R_{II} at this position. Essentially cross-correlation function statistically measures the degree of match between the two samples for a given shift. The highest value in the correlation plane can then used as a direct estimate of the particle image displacement.

4.4.2 Cross-correlation function via finite Fourier transforms

The direct method to compute the cross-correlation quickly becomes very heavy to apply when larger data-sets are to be analyzed. A more efficient way to estimate cross-correlation functions is use fast Fourier transforms (FFTs). This reduces the

computation from $O[N^4]$ operations to $O[N^2 log_2 N]$ operations in the case of a two-dimensional correlation. When Fourier transforms are used one takes advantage of the correlation theorem (see e.g. Bendat & Piersol 1986) which states that the cross-correlation of two functions is equivalent to a complex conjugate multiplication of their Fourier transforms:

$$R_{AB} \Leftrightarrow \hat{A} \cdot \hat{B}^*. \tag{4.9}$$

Where $\hat{A}$ and $\hat{B}$ are the Fourier transforms of A and B, respectively and $\hat{B}^*$ represents the complex conjugate of $\hat{B}$.

In practice two real-to-complex, two-dimensional FFT's and one complex-to-real inverse, two dimensional FFT are needed each of which requires approximatively half of the computation time of standard FFT's (Figure 4.7).

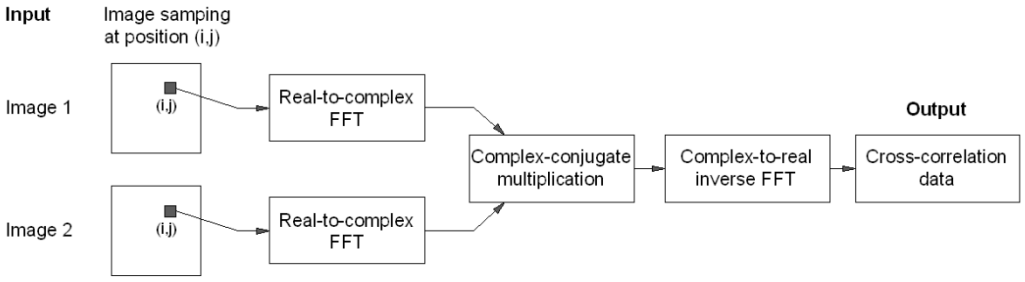

Figure 4.7: Implementation of cross-correlation using fast Fourier transforms

Using FFTs means treating the data as if it is periodic. The periodicity can give rise to aliasing if the particles have moved a distance larger than half the size of the interrogation area. The solution to aliasing problems is to either increase the interrogation area size or reduce the inter image time Δt. A maybe more serious problem with the FFTs is that bias errors occur if these are not accounted for. Due to the finite size of the interrogation areas the overlap of the images becomes smaller with increasing displacement. This bias results in an underestimation of the peak magnitude for all displacements other than zero. A weighting function should be applied to the cross-correlation function to avoid this bias. This weighting function is found by convoluting the sample weighting functions (which should be equal to one for all points in the image and zero elsewhere). The bias is removed by dividing the correlation function with the effective weighting function which will have a pyramid shape.

4.4.3 Advanced digital interrogation techniques

The data yield in the interrogation process can be significantly increased by using a window offset equal to the local integer displacement in a second interrogation pass (Westerweel et al., 1997). By offsetting the interrogation windows the fraction of matched particles images to unmatched particle images is increased, thereby increasing the signal-to-noise ration of the correlation peak.

4.4.4 Peak detection and subpixel interpolation

When the cross-correlation has been performed a measure of the displacement is found by detecting the location of the highest correlation peak. Just detecting the peak will

result in an uncertainty of ±1/2 pixel in the peak location. However, the accuracy can be increased substantially by curve fitting and interpolation.

The use of curve fitting on the correlation peak to obtain subpixel resolution was the critical step that allowed for a digital implementation of PIV. The measurement resolution of displacement estimations changed from ± 1/2 pixel to 1/100th of a pixel upon the implementation of a sub-pixel estimator. Generally, the subpixel fit is taken over the primary correlation value and the neighbouring pixel on either side.

In commercial codes, the subpixel location of the correlation peak in both the x- and y-directions is determined using the five central points of the correlation peak (Fore 2010); the four adjacent points in the x- and y-directions and the central correlation peak value. Although many sub-pixel estimators are available the three most commonly used are the centroid estimator, the parabolic estimator and the Gaussian estimator (Willert & Gharib 1991).

When the maximum peak has been detected at $[i,\ j]$, the neighbouring values are used to fit a function to the peak. In the case of a Gaussian peak fit when the peak is assumed to have the shape $f(x) = Cexp[-(x_0 - x)^2/k]$, the displacement are found by:

$$x_0 = i + \frac{\ln R_{(i-1,j)} - \ln R_{(i+1,j)}}{2\ln R_{(i-1,j)} - 4\ln R_{(i,j)} + 2\ln\ R_{(i+1,j)}}$$
$$y_0 = j + \frac{\ln R_{(i,j-1)} - \ln R_{(i,j+1)}}{2\ln R_{(i,j-1)} - 4\ln R_{(i,j)} + 2\ln\ R_{(i,j+1)}} \tag{4.10}$$

Westerweel (1993) stated that the Gaussian estimator is superior to both the centroid and parabolic estimators as it produces the lowest measurement errors of the three sub-pixel estimators examined. The Gaussian estimator is generally accepted as being the standard estimator when processing with the standard cross-correlation algorithms.

4.4.5 Measurement accuracy and valid vector detection probability

The measurement accuracy of the DPIV processing algorithm can be defined by three metrics: the valid vector detection (VVD) probability, biases, and RMS errors. The most crucial factor in designing a digital algorithm is the VVD probability (Adrian 2005) which is a direct reflection of the signal strength. The VVD probability should be on the order of 90-100% to provide an accurate measurement (Westerweel et al. 2005). The major factors responsible for invalid measurement, so-called outliers or spurious vectors, are an insufficient number of particles being present in the interrogation areas, strong velocity gradients and strong three-dimensional flow motions. It is inherent to their nature that the outliers usually appear randomly both in direction and in amplitude. Usually these errors are larger than one pixel and are therefore easy to detect. The erroneous vectors are removed through the process of validation (see Section 4.5.1).

Provided the measurement is valid, the accuracy is then described by bias and RMS errors. Given a unique displacement applied to all particles, the particle displacements obtained with PIV at various interrogation locations can be different. Suppose that the actual particle displacement is d_a and N displacements d_i (i= 1, 2, 3...N) have been

evaluated. The difference between the actual displacement d_a and the mean of these displacements,

$$d_m = \frac{1}{N}\sum_{i=1}^{N} d_i. \tag{4.11}$$

is the means-bias error d_b

$$d_b = d_m - d_s. \tag{4.12}$$

The random error is used to determine the deviation of measured displacements for each realization from the mean measured displacement. This is termed the root mean square (RMS) error or σ, and is defined as:

$$\sigma = \left(\frac{\sum_{i=1}^{N} (d_i - d_m)^2}{N} \right)^{1/2} \tag{4.13}$$

which reflects the deviation of the particle displacements from their mean.

The measurement RMS is a reflection of the noise floor, which is clearly related to the image noise and signal density. Several sources of bias error can exist within the measurement.

The loss of correlation bias is a result of the decreased energy density at higher image shifts. As a result, the correlation peak is biased to lower image displacements (Raffel at al. 1998). Peak-locking is a discretization error in which measurements are biased toward integer pixel values (Raffel at al. 1998). The bias errors ('peak locking') decrease with increasing diameter of the particle images, whereas the random errors increase proportionally to the particle-image diameter. Consequently, there exists an optimum for which the total error is minimal. Typical values for the optimal particle-image diameter is 2-4 pixels, with an error of 0.10 to 0.15 pixels.

Fluid acceleration can introduce a bias due to the assumption of constant velocity between image pairs. Similarly, shear and rotation within the velocity field can lead to large biases due to the assumption of constant displacement over the window domain. Iterative correlation methods described above have shown substantial capabilities to minimize these errors.

While erroneous vectors and RMS are relatively easy to detect through a visual inspection of the vector fields, these bias errors can be more subtle. Therefore, it is important to quantify these errors and to remove them when possible.

4.4.6 Iterative correlation methods

As the displacement between regions increases, the number of particle images that contribute to the correlation peak decreases and is referred to as the out-of-pattern effect. Concerns were raised that the loss of signal would increase measurement errors and therefore investigations proceeded to minimise this effect. One solution to increase measurement accuracy is through the use of iterative correlation methods.

One of the simplest iterative methods is discrete window shifting (DWS) (Westerweel et al. 1997). This method estimates the shift required by the first region by estimating the displacement from an initial cross-correlation. After the shift, a second cross-

correlation provides a sub-pixel displacement where the out-of-pattern effect has less of an influence on measurements.

An extension to the DWS is continuous window shifting. After an initial displacement estimation this process uses bi-linear image interpolation before a second cross-correlation provides the sub-pixel displacement. Advances in this technique have lead to the development of higher order interpolation functions being developed including the sinc function (Lourenco & Krothapalli 1995 and Roesgen 2003) and a Gaussian function (Nobach et al. 2004) and also the Particle Image Distortion (PID) technique (Huang et al. 1993a). This process manipulates the interrogation region shape before a final displacement estimate is determined.

Although these methods have been shown to have a substantially better estimate over the standard DWO, they are substantially more computationally expensive and are heavily dependent upon the interpolation scheme used to return to a rectilinear grid.

4.5 Post-processing data

4.5.1 Data validation.

After automatic evaluation of the PIV recordings a certain number of incorrectly velocity vectors (so-called outliers) can usually be found by visual inspection of the raw data. These vectors deviate unphysically in magnitude and direction from nearby "valid" vectors, and are often the result of insufficient particle images, large in-plane or out-plane displacements, or high spatial gradients of the velocity; other causes can be a strong background image or light-sheet inhomogeneity. In practice the number of spurious vectors in a PIV data set is relative low (typically less than 5%). However, their occurrence is more or less inevitable.

Methods to reduce or remove the outliers have been discussed in many publications (Keane & Adrian 1990, Willert 1992, Huang et al. 1993a, 1993b, Westerweel 1993)

Generally, PIV measurement data are subjected to a post-interrogation procedure in which spurious vectors are identified and subsequently discarded from the data set.

For automated validation there are generally two approaches, which are based on:

1. correlation signal quality;
2. local coherence of the vector map, i.e., a comparison of each vector with measurement displacements in adjacent interrogation regions.

In general methods based on correlation signal quality are not very robust and the evaluation based on coherence appears to be much more efficient.

The effectiveness of several validation techniques based on local coherence of the vector map has previously been discussed by Westerweel (1994). Three different tests, based on the global-mean, the local-mean and the local-median estimators have been compared. Westerweel (1994) found that a local median test is the most effective.

4.5.2 Replacement of incorrect data.

After having validated all PIV data it is possible to fill in the missing data using, for instance, bilinear interpolation. According to Westerweel (1994) the probability that

there is another spurious vector in the direct neighborhood of a spurious vector is given by a binomial distribution. For istance if the data contains 5% spurious vectors, more than 80% of the data can be recovered by a straight bilinear interpolation from the four valid neighboring vectors. The remaining missing data can be estimated by using some sort of weighted average of the surrounding data, such as the adaptive Gaussian window technique proposed by Agüi & Jiménes (1987).

Some post-processing methods also required smoothing of the data. The reason is that the experimental data are affected by noise in contrast to numerical data. A simple convolution of data with a 2 x 2, 3 x 3 or larger smoothing karnel (with equal weights) is generally sufficient for this purpose.

4.6 Multi phase flows

Initially applied only to single phase flows, PIV has been adapted to measure the in-plane velocity field of multiphase flows. There are many different implementations of PIV for two-phase flows, which have been reviewed extensively by Brücker (2000), Deen et al. (2002) and Seol and Socolovsky (2008), among others.

The difficulty in dealing with multiphase flows lies in the fact that the bubble phase and liquid phase exist together in the flow. Thus, the challenge in applying PIV to multiphase flows is in separating the tracer particles tracking the entrained continuous phase from the dispersed phase particles, droplets, or bubbles. There are several methods available to discriminate and separate the information of the phases present in the flow, which have been reviewed by Brücker (2000).

Broadly speaking, these methods can be classified into the following three main groups:

- Optical method: two separate images are generated for bubbles and tracer particles by means of optical filters, two-camera system and fluorescent tracer particles (Sridhar et al. 1991; Hilgers et al. 1995; Deen 2001);
- Image processing techniques: the phases are separated into two images before PIV analysis (Gui & Merzkirch 1996, Gui et al. 1997; Delnoij et al. 1999, Brücker 2000, Grota & Strauß 2000, Kiger & Pan 2000, Deen et al. 2002) or after processing the mixed-fluid PIV images (Seol et al. 2007);
- Ensemble correlation technique: the phases are discriminated on basis of the slip velocity between the bubbles and the surrounding liquid (Delnoij et al. 1999, Deen 2001).

Although the optical separation methods have proven to be the most reliable (Deen 2001, Bröder & Sommerfeld 2002), it is desired to have a cheaper and easier method to avoid the complex and expensive setup for the optical separation methods.

In this thesis, a simple, inexpensive method of phase separation is tested. This method uses standard tools available in most image analysis software and PIV software. Starting from an original image which contains both phases, by means of image processing techniques, it's possible to obtain a mask in which seed particles and bubbles are separated. This is attained by taking advantage of the difference in size and intensity between bubbles and trace particles. When this mask is subtracted from the raw image ones obtains an image that contains only trace particles. Then subtracting

the trace particle image from the original image an image of bubbles is obtained. A more detailed description of the method is presented in Chapter 5.

Chapter 5 Flotation Modelling

5.1 Introduction

Froth flotation is a highly versatile method for physically separating particles based on differences in the ability of air bubbles to selectively adhere to specific mineral surfaces in a mineral/water slurry. The particles with attached air bubbles are then carried to the surface and removed, while the particles that remain completely wetted stay in the liquid phase. Froth flotation has been used in the mineral industry since early 19th century and it has been proved to be a cost effective beneficiation process for several minerals. Since then, there has been a steady progress and development in flotation process and nowadays it is widely used throughout the mining industry as well as the chemical, and petroleum industries.

Although froth flotation is the dominating mineral beneficiation technique, its high process efficiency is often limited to a narrow particle size range of approximately 10–100 μm(Tao 2005). This is in contrast with the progressive reduction of grade mineral deposits that leads to the production of ultrafine particles in order to liberate mineral particles from the ore. Therefore, to exploit economically complex low-grade mineral deposits, it is crucial improving the flotation efficiency of fine particles.

The problem (very old) of processing by flotation, the fine and ultrafine mineral particles continues to be one of the major technical challenges in the area of mineral processing (Trahar 1981, Sivamohan, 1990, Collins & Read 1971).

In this chapter a review of the principle of the flotation process and its modelling are done in order to highlight the reasons for the low recovery of fine particles. Then the potentialities offered by the use of waterjets to fine particles flotation are presented.

5.2 Principle of flotation

Flotation is a physico-chemical separation process that utilizes the difference in surface properties of the valuable minerals and the unwanted gangue minerals. In general, the substances to be separated are crushed until their individual components are present "liberated". This mixture, the *feed*, is suspended in an aqueous, not too thick pulp (or gangue) which has to be properly stirred in order to maintain the state of suspension. To selectively separate the valuable component from the others (the tailings), gas bubbles are dispersed to which the valuable component is selectively attached whereas the other components remain in the pulp. The attachment of particles to gas bubbles result in aggregates of lower density which rise (float) to the pulp surface. Thus, basically, a separation takes place according to density, but the separating characteristic is the attachability to gas bubbles. At the pulp surface the rising bubbles form a froth layers in which the particles attached to them gather. This froth layer can be removed mechanically from the surface (Shulze 1984).

The process of material being recovered by flotation from the pulp comprise three mechanisms:

1. selective attachment to air bubbles (or "true flotation");
2. entrainment in the water which passes through the froth;
3. physical entrapment between particles in the froth attaches to air bubbles (often referred to as "aggregation").

Although the degree of entrainment and the physical entrapment also influence the separation efficiency between the valuable mineral and gangue, true flotation is the dominant mechanism for the recovery. So we will focus only on this mechanism.

As already mentioned, in true flotation the mineral particles can only attach to the air bubbles if they are hydrophobic. Particles can either be naturally hydrophobic, or the hydrophobicity can be induced by chemical treatments. Naturally hydrophobic materials include hydrocarbons, and non-polar solids such as elemental sulfur. Coal is a good example of a material that is typically naturally hydrophobic, because it is mostly composed of hydrocarbons.

The attachment of the bubbles to the surface is determined by the interfacial energies between the solid, liquid, and gas phases. This is determined by the Young/Dupre Equation,

$$\gamma_{1V} \cos\theta = (\gamma_{SV} - \gamma_{S1}) \tag{5.1}$$

where γ_{1V} is the surface energy of the liquid/vapor interface, γ_{SV} is the surface energy of the solid/vapour interface, γ_{S1} is the surface energy of the solid/liquid interface, and θ is the “contact angle”, the angle formed at the junction between vapor, solid, and liquid phases, as shown in Figure 5.1. If the contact angle is very small, then the bubble does not attach to the surface, while a very large contact angle results in very strong bubble attachment. A contact angle near 90° is sufficient for effective froth flotation in most cases.

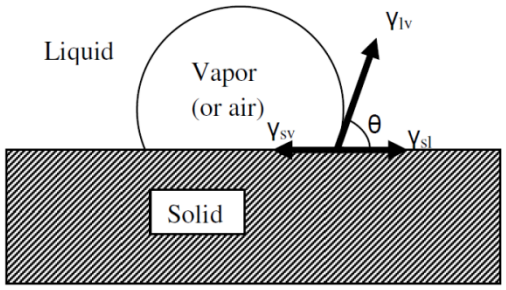

Figure 5.1: Contact angle between and air bubble and a solid surface immersed in liquid.

5.3 Flotation kinetics and modelling

Flotation kinetics studies the variation of floated mineral mass according to flotation time. If all operational variables are kept constant, the algebraic relationship between the parameters mentioned above is a flotation rate equation. By analogy with chemical kinetics, the equation representing flotation kinetics may be expressed by the following equation (Derjaguin & Dukhin 1961, Sutherland 1948):

$$\frac{dN_1}{dt} = f(k, N_i) = -k_1 N_1^f - k_2 N_2^g \tag{5.2}$$

The model directly predicts the change in particle concentration, N_i, with respect to time, t, as a function of a certain concentration(s), N_i, and rate constant(s), k_i. The negative sign indicates that the concentration is diminishing due to the loss of particles being floated. The exponents f and g signify the order of the process.

Most researchers believe that flotation is a first order process and a function of only the particle concentration and a rate constant (Sutherland 1948, Jameson et al. 1977):

$$\frac{dN_1}{dt} = kN_1 \tag{5.3}$$

where k is the flotation rate constant and t is the flotation time.

The rate constant, k, within this equation conveys how rapidly one species floats. A high rate constant indicates that certain species floats quickly while a low rate constant indicates slow flotation.

If the initial number of particles is N_0 at $t = 0$, Equation (5.3) can be integrated to yield

$$N = N_0 e^{-kt} \tag{5.4}$$

The recovery of the particles, R, is defined by

$$R = \frac{N_0 - N}{N_0} \tag{5.5}$$

In terms of the recovery, Equation (5.5) becomes:

$$R = R_{max}(1 - e^{-kt}) \tag{5.6}$$

where R represents the fractional recovery of the floatable species after time t; R_{max} is the maximum theoretical flotation recovery, i.e. after infinite time; and t is mean residence time of particles in the cell.

For the case of a perfectly mixed reactor design, fractional recovery derived from Equation (5.3), is given by:

$$R = \frac{kt}{1 + kt} \tag{5.7}$$

This model has been typically used for calculation of the fractional recovery of particles in the pulp phase of a single flotation cell (Lynch 1981).

In a simple batch flotation case where mixing is not involved (Jameson et al. 1977, Yoon & Mao 1996), the flotation rate constant is

$$k = \frac{3J_g}{2d_b}P \tag{5.8}$$

where d_b is the bubble diameter, P is the bubble–particle collection efficiency and J_g is the superficial gas velocity, defined as volumetric gas flow rate divided by the cross-sectional area of the flotation column.

According to Sutherland, flotation rate can be expressed as a product of collision frequency between particles and bubbles (Z_{12}) and probability of flotation (P) as presented here (Sutherland 1948):

$$k = -Z_{12}P \tag{5.9}$$

Z_{12} is related to the particle–bubble collision frequency dependent on the size of the particles and bubbles, and hydrodynamics of the flotation pulp.

As previously mentioned, the capture of a particle and a bubble is generally divided into three separate process (Derjaguin & Dukhin 1961): collision, attachment and detachment.

The bubble–particle collection or capture efficiency, P, can be defined as a product of bubble–particle collision, P_c, attachment, P_a, and stability, P_s, efficiencies, since these processes, all of which are probabilities, are independent of each other. This dissection was formally proposed by Derjaguin and Dukhin (1961):

$$P = P_c P_a P_s \tag{5.10}$$

The probability of attachment depends mostly on the surface characteristics of the mineral, the degree of collector adsorption on the mineral surface, and the induction time required for attaching the hydrophobic particle to the bubble. The probability of a particle remaining attached to the bubble depends on the turbulence level in the cell as well as size of particle.

Numerous models have been proposed for the evaluation of the collision, attachment and stability efficiencies. Some of these models will be presented later on.

Assuming independence of particle velocities from fluid flow, Abrahamson derived a turbulent collision model whose simplistic form is presented here (Abrahamson 1975):

$$Z_{12} = 2^{2/3}\pi^{1/2} N_1 N_2 d_{12}^2 \sqrt{\bar{u}_1^2 + \bar{u}_2^2} \tag{5.11}$$

where N_1 is a number of particles, N_2 is a number of bubbles, d_{12} is collision diameter or sum of radii of one bubble and one particle, $\bar{u}_1$ is the RMS velocity of particles, and $\bar{u}_2$ is the RMS velocity of bubbles.

Based on work of Abrahamson (1975), Schubert and Bischofberger (1979) have proposed the following equation for the number of particle–bubble collisions per unit time and volume in mineral flotation where inertial effects are the primary cause of collisions:

$$Z_{12} = 5 N_1 N_2 \left(\frac{d_p + d_b}{2}\right)^2 \sqrt{U_p^2 + U_b^2} \tag{5.12}$$

where d_p is the particle diameter and d_b is the bubble diameter, U_p is the turbulent (rms) fluctuating velocity of the particle relative to the fluid, and U_b is the turbulent (rms) fluctuating velocity of the bubble relative to the fluid. In typical flotation processes, these velocities ($U_i = U_p$ *or* U_b) are a function of the local turbulent dissipation rate as follows (Schubert & Bischofberger 1979):

$$U_i = \frac{0.4 \varepsilon^{4/9} d_i^{7/9}}{\nu^{1/3}} \left(\frac{\rho_i - \rho_f}{\rho_f}\right)^{2/3} \tag{5.13}$$

where ε is the turbulent dissipation rate per unit mass, ν is the kinematic viscosity, ρ_f is the fluid density, and ρ_i is the density of the particle (p) or bubble (b). The condition for use of the above model with independent velocities is that the diameter of the particle or bubble must be greater than the critical diameter, d_{crit} in the following equation:

$$d_i^2 > d_{crit}^2 = \frac{15 \mu_f U_f^2}{\rho_i \varepsilon} \tag{5.14}$$

where ρ_f is the fluid viscosity and U_f is the mean fluid velocity deviation. Otherwise, the collision equation by Saffman and Turner (1956) is applicable for fine particles and bubbles confined within eddies in low turbulent dissipation regions as follows:

$$Z_{12} = \sqrt{\frac{8\pi}{15}} N_1 N_2 \left(\frac{d_p + d_b}{2}\right)^3 \sqrt{\frac{\varepsilon}{\nu}} \tag{5.15}$$

The most recent general turbulent flotation rate model was given by Pyke, Fornasiero, and Ralston (2003):

$$k = -2.39 \frac{G_{fr}}{d_2 V_{cell} u_2} \left(\frac{0.33 \varepsilon_d^{4/9} d_2^{7/9}}{\nu^{1/3}}\right) \left(\frac{\Delta\rho_2}{\rho_3}\right)^{2/3} P_c P_a P_s \tag{5.16}$$

In Equation (5.16), P_c, P_a, P_s, are the efficiencies of collision, attachment and stability respectively. The remainder of the equation is the collision frequency. The true number of collisions, that may or may not become attached, results from the combination of the collision efficiency and collision frequency. The collision frequency shown in Equation (5.16) is a modified equation given by Abrahamson (1975) that is divided by the number density of particles.

Equation (5.16) provides a model of the flotation process based upon turbulent characteristics of the flow as well as hydrodynamic forces. What the model does not account for is the effects of surface forces.

5.3.1 Bubble-particle collision

The first step involved in flotation is the process of particle–bubble collision during which a particle collides with a bubble as a result of a sufficiently close encounter. This process is primarily determined by hydrodynamics of the flotation environment. Among the three successive subprocesses of particle-bubble interaction, the collision subprocess has been investigated the most extensively and numerous models have been proposed for the evaluation of the collision efficiency. Due to the complexity of the collision subprocess, a simplified picture of the system has frequently been adopted. As a result, though all of these P_c models are based on a hydrodynamic analysis of the particle-bubble system, they are different because of the various simplifications and assumptions made in each case. A detailed review of bubble–particle collision models has been given by Dai et al. (2000).

The Stokes number (St) and the bubble Reynolds number (Re_b) are critical in defining the flow parameters that characterize P_c.

The Stokes number represents a ratio of inertia to drag forces and is defined as

$$St = \frac{\rho_b u_b d_p^2}{9 d_b \mu_f} \tag{5.17}$$

where u_b is the bubble rise velocity , μ_f is the dynamic viscosity of the fluid, d_b is the bubble diameter, and ρ_p and d_p are the density and the diameter of the particle, respectively.

This dimensionless number can be used to characterize the shape of the particle trajectory in the fluid flow and the interactions between the particle and bubble surfaces (Ralston et al., 2002). For conditions where:

- $St \ll 1$: inertial forces have practically no effect on the motion of the particles, which can be considered as inertia-free.
- $St \leqslant 0.1$: "negative" inertial forces can impede particle deposition on a bubble (Dai et al. 1998).
- $0.1 < St < 1$: an inelastic inertial impact of particles on a bubble surface is characteristic of this regime and a major portion of the kinetic energy of the particles is lost both during the approach to the bubble and at the impact itself, when a liquid layer is formed between the surfaces of a particle and a bubble.
- $St > 3$: the trajectory of a particle deviates very slightly from a straight line and the energy of the particle, as it approaches the bubble and on collision, changes so little that the impact can be considered as being quasi-elastic, i.e. the particle bounces away from the bubble surface at almost the same speed as it approaches the bubble surface.

The Reynolds number is the ratio of the inertial forces to the viscous forces of the fluid and is defined as:

$$Re_b = \frac{\rho_f d_b u_b}{\mu_f} \tag{5.18}$$

where ρ_f is the density of the fluid.

The first model of bubble–particle collision was proposed by Sutherland (1949) for the condition of potential flow. In this model, Sutherland assumed that firstly, particle inertia can be neglected and thus particles follow the streamlines of the fluid, so that the particle trajectories and thus the collision efficiency can be determined from the streamlines of the fluid; secondly, the bubble surface is completely unretarded, or mobile; and thirdly the fluid flow regime at the bubble surface is potential, i.e. the Reynolds number of the bubble is very large ($Re_b \gg 1$).

Using the Ramsey equation for the streamlines of a fluid moving past a sphere, Sutherland derived an equation for the distance R_c. of a critical stream-line from the line of motion of the bubble (Figure 5.2).

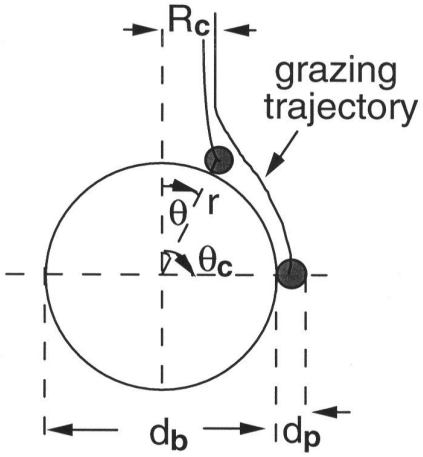

Figure 5.2: Schematic representation of the grazing trajectory of a particle around a bubble (Dai et al. 2000)

This critical streamline is defined as the fluid streamline where a particle, moving along it, just touches the bubble surface. The particle trajectory which coincides with this critical streamline is also called the grazing trajectory, or limiting trajectory, and R_c is also referred as the collision radius. The collision radius, R_c , is expressed as

$$R_c = \left(\frac{3d_p d_b}{4}\right)^{1/2} \tag{5.19}$$

According to Sutherland, all particles lying within the collision radius will collide with the bubble and therefore the collision efficiency, P_c, is determined by the ratio of the cross-sectional area of the stream tube ($\pi R_c^2 = 3\pi d_p d_b/4$) to the projected area of the bubble ($\pi d_b^2/4$), i.e.

$$P_c = \frac{3d_p}{d_b} \tag{5.20}$$

where d_b is the bubble size and d_p the particle size. This model is valid only when bubbles are very large and water in a flotation cell is nonviscous, neither of which is realistic. As a result, it cannot be used to accurately describe the flotation process.

Gaudin (1957), assuming a Stokes flow regime around the bubble surface and ignored the inertial force of the particles, used the following equation to express the collision efficiency

$$P_c = \frac{3}{2}(d_p/d_b)^2 \tag{5.21}$$

Yoon (1991) compared the Gaudin model prediction with experimental data and concluded that the model is useful for bubbles smaller than approximately 100 μm in diameter. This is expected, since for bubbles in this size range, the assumption of Stokes flow is valid ($Re_b \ll 1$).

Neither Sutherland's nor Gaudin's model can be applied to flotation processes in most industrial flotation cells where the bubble size falls between these two extreme cases.

Weber and Paddock (1988) proposed a model for the collision of spherical particles with spherical collectors. In their model, they assumed that the particles were very small, the hydrodynamic interaction between the particles and the fluid was negligible, the streamlines of the fluid could be characterized by the Stokes stream function and that these stream functions could be approximated by a Taylor series. The collision efficiency was express as

$$P_c = \frac{3}{2}\left[1 + \frac{(3/16)Re_b^{0.72}}{1 + 0.24Re_b^{0.56}}\right]\frac{d_p^2}{d_b^2} \tag{5.22}$$

which was the first collision model to apply for wide ranges of particle and bubble sizes.

Yoon-Luttrell (1989) developed a new stream function valid for intermediate Reynolds numbers by combining the Stokes and potential stream functions. Through this stream function, a formula for collision efficiency under intermediate Reynolds numbers was derived

$$P_c = \left(\frac{3}{2} + \frac{4}{15}Re_b^{0.72}\right)\frac{d_p^2}{d_b^2} \tag{5.23}$$

The equation is valid for particles smaller than 100 μm and bubbles smaller than 1 mm with immobile surfaces due to adsorbed surfactants. Equation (5.23) shows that the collision efficiency increases with the square of particle size to bubble size ratio, but is also a function of the bubble Reynolds number.

This model is more general than the Sutherland collision model since it considers different flow conditions at the bubble surface and, correspondingly, different stream functions are used to characterize the respective streamlines trajectories.

All the abovementioned models are based on the interceptional collision model that neglects particle inertial forces, since particle mass density is often low.

A more comprehensive collision model was proposed by Schulze (1989) who considers that the overall collision probability P_c is the sum of three different effects, i.e., interceptional (P_c^{ic}), gravitational (P_c^{g}), and inertial (P_c^{in}):

$$P_c = P_c^{ic} + P_c^{g} + \left[1 - \frac{P_c^{ic}}{\left(1 + (d_p/d_b)^2\right)}\right] \cdot P_c^{in} \tag{5.24}$$

Schulze suggested that the interceptional and gravitational collision probabilities be determined using the Weber–Paddock collision model (Equation (5.22)) and the inertial probability, (P_c^{in}), using the Plate model (Tao, 2005):

$$P_c = \left(\frac{1}{1 + \nu_p/\nu_b}\right)\left(\frac{K}{K + a}\right)^{b} (1 + d_p/d_b)^2 \tag{5.25}$$

where K is the Stokes number, ν_b is the rising velocity of the bubble, ν_p is the settling velocity of the particle, and the constants a and b are Reynolds number-dependent coefficients whose values are shown in Table 3.

Table 3: Values of a and b (Schulze 1989)

Re_b	>500	250-500	100-250	50-100	25-50	5-25	<5
a	0.5	0.6	0.8	1.12	2.06	2.48	1.3
b	2	2	2	1.84	2.06	1.95	3.7

There are a number of other models that describe particle–bubble collision in flotation. A thorough review of these models is provided by Dai et al. (2000).

By incorporating the influence of particle inertial forces, the Schulze model is superior to most other collision models. However, the collision efficiencies calculated with this model are too high because the negative effect of the inertial forces is neglected.

5.3.2 Bubble-particle attachment

The attachment of solid particles to air bubbles determines the selective separation between hydrophobic and hydrophilic particles in a flotation process. Thus this sub-process constitutes the most important act of a flotation.

The attachment process requires significantly more complex modelling than the collision process which, as shown in the previous section, is governed primarily by the

fluid dynamics close to the bubble. The attachment process is governed by hydrodynamic and chemical factors which interact in complex ways that ultimately determine whether a particle will attach to the bubble or not.

For a successful particle-bubble attachment, three steps have to take place (after particle collision):

- thinning of the intervening liquid film to a thickness h_{cr} where the film ruptures (also called critical thickness),
- rupture of the intervening liquid film and formation of a "hole" of the three-phase contact (TPC) (a hole of a critical wetting radius r_{cr}), and
- expansion of the "hole" and formation of the perimeter of the three phase contact assuring stability of the bubble-particle aggregate.

The time taken from the instant of collision to the establishment of a stable three-phase contact is called the induction time which will be represented by t_{ind}. The induction time for a particle is determined primarily by its contact angle but the particle size and shape are also important. Other chemical factors such as the concentration of surfactants at the bubble surface and the interaction between collector adsorbed on the solid and frother on the bubble surface also play a role.

While the film thinning, film rupture and receding three-phase contact line are proceeding another, purely physical, process is occurring. The particle is being carried downward over the surface of the bubble by the water as it moves past the bubble surface. If a stable three-phase contact has been established before the fluid stream lines start to diverge from the bubble, successful attachment is achieved. Particles that have not formed a stable three-phase contact by the time the streamlines start to diverge from the bubble surface at the equator are pulled away from the bubble surface and they do not attach. The time taken by a particle to slide over the bubble surface from its point of collision to the point of divergence is called the sliding time, t_s.

Another mechanism for particle adsorption is also possible. The particle may directly impact the bubble surface. As the particle strikes the bubble, the bubble is deformed. If a stable contact is achieved before the particle is repulsed by the reformation of the bubble surface, adsorption will occur.

The contact time is considered to be the time for which a particle and a bubble are in contact after their collision. In the case of particle rebound from the bubble surface, the only component in the contact time is the impact time. If particle sliding occurs after the bubble–particle impact, the contact time is the sum of the impact time and the sliding time.

Particles with diameters less than about 100 μm only impact and slide on the bubble surface, for their collision kinetic energy is too small to distort the bubble surface (Dobby & Finch 1987). There is no rebound without bubble surface deformation. Typically, the contact times are very short, about 10 ms or less (Schulze 1984). Considering only particle attachment by sliding, the probability of attachment by sliding, P_a can be defined as the fraction of particles in the path of the bubble that actually adheres, compared to the maximum possible. Referring to Figure 5.3 this should be the ratio of the area inscribed by the limiting radius R_{crit}, the radius from the stagnation line to the line corresponding to the touching angle associated with ϕ^*_{crit}, to

the area inscribed by the sum of the bubble, particle, and critical film thickness ($R_B + R_p + h_{crit}$). Since we can expect $h_{crit} \ll R_p$, it is common to write P_a as

$$P_a = \frac{R_{crit}^2}{(R_B + R_P)^2} \tag{5.26}$$

Relating R_{crit} to ϕ^*_{crit}, Equation (5.26)can be written as

$$P_a = \sin^2 \phi^*_{crit} \tag{5.27}$$

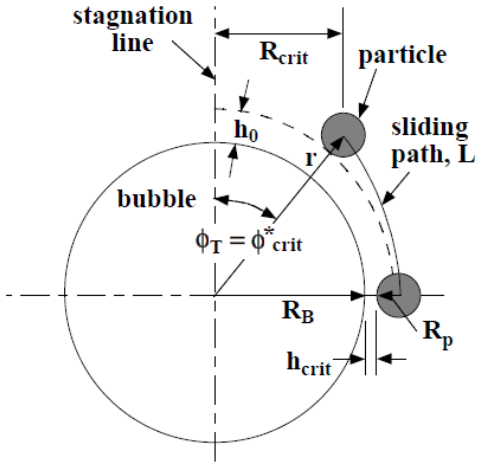

Figure 5.3: Schematic representation of P_a

The critical angle ϕ^*_{crit} is extremely difficult to measure experimentally. Bloom and Heindel (1997) describe a process to calculate the angle by integrating the sum of the forces acting on the particle over time. The behaviour of the thin film between the bubble and the particle is modelled to yield an expression relating the critical film thickness to the maximum of the critical angle. This is only useful if experimental data is available for the critical film thickness, which is as difficult to observe as the critical angle.

Another possible approach is to modelled the probability of attachment in terms of contact time and induction time. If the sliding time is longer than the induction time, adhesion is likely. Yoon and Luttrell (1989) derived an expression for the adhesion probability dependent on the particle and bubble sizes, the bubble Reynolds number and the induction time as follows:

$$P_a = \sin^2 \left(2 \arctan \exp \left[\frac{-(45 + 8Re_b^{0.72} u_b t_{ind}}{15 d_b (d_b/d_p + 1)} \right] \right) \tag{5.28}$$

where u_b is the bubble relative velocity.

The induction time is a function of the particle size and contact angle which can be determined by experiment and correlated in the form

$$t_{ind} = A d_p^B \tag{5.29}$$

where parameters A and B are independent of particle size.

Once the thin film has ruptured, three-phase contact points must form between the bubble, particle, and liquid. A contact point must form quickly to prevent the particle from immediately detaching from the surface. This aggregate formation is

schematically represented in Figure 5.4, where θ represents the contact angle measured in the liquid.

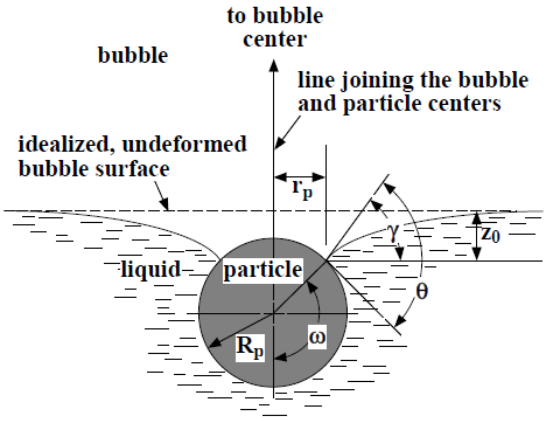

Figure 5.4: The three-phase contact between the bubble, particle, and liquid regions

Schulze (1984) proposes that the turbulent vortices in the cell are the main source of disruption of this formation and that for formation to occur, the time needed to form the three-phase contact, τ_{TPC}, must be less than the average lifetime of the turbulent vortices, τ_v. He proposes that the probability of this formation has the form

$$P_{TPC} = 1 - \exp\left(\frac{-\tau_v}{\tau_{TPC}}\right) \tag{5.30}$$

Schulze also shows that this probability is equal to 1 for many particles sizes. Indeed, most authors neglect this probability in their models (Heindel & Bloom 1997, Dai et al. 2000, Yoon 1991).

5.3.3 Probability of Attachment Stability

Once a bubble-particle aggregate forms, it must remain stable on its journey to the froth layer to be removed from the system. It has generally been accepted (Schulze 1984, Hou at al. 1993, Bloom at al. 1997) that bubble-particle stability can be determined by performing a force balance on the particle attached to the bubble. Figure 5.5 summarizes these forces (Heindel 1999).

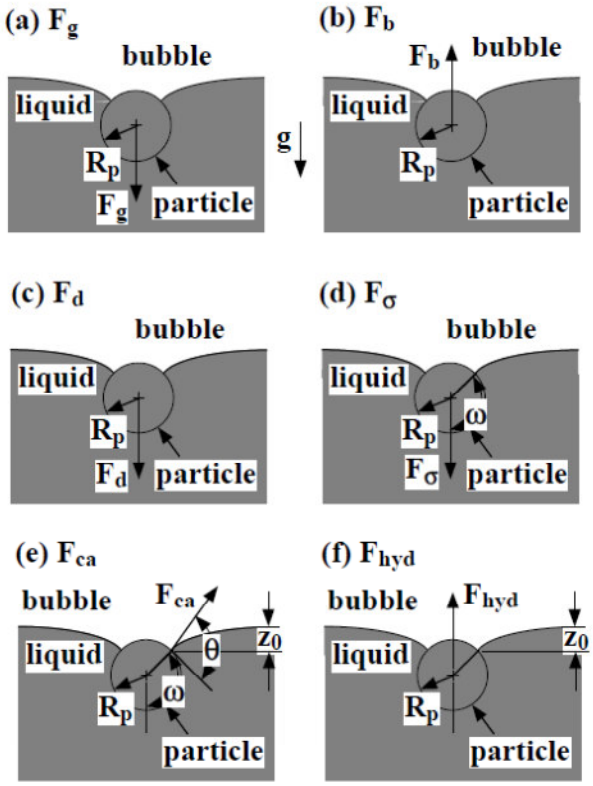

Figure 5.5: Forces that act on a bubble-particle aggregate

Assuming spherical particles, the gravitational force (Figure 5.5a) is specified by

$$F_g = \frac{4}{3}\pi R_p^3 \rho_p g \tag{5.31}$$

where r_p is the particle density, and g is the acceleration due to the gravity. The static buoyancy force that acts on the particle (Figure 5.5b), assuming that the entire particles is immersed in the liquid, is

$$F_b = \frac{4}{3}\pi R_p^3 \rho_\ell g \tag{5.32}$$

with ρ_ℓ the liquid density. The buoyant and gravitational force can be combined to obtain an expression for the apparent particle weight

$$F_{wt} = \frac{4}{3}\pi R_p^3 (\rho_p - \rho_\ell) g \tag{5.33}$$

For the detaching force due to fluid drag (Figure 5.5c),

$$F_d = \frac{4}{3}\pi R_p^3 \rho_p a_c \tag{5.34}$$

where expressions for the fluid acceleration, a_c depend on both the structure and intensity of the turbulence within the flotation cell. For aggregates where the particle size is smaller than the bubble size, it has been determined that the fluid acceleration can be related to the energy dissipation in the tank by (Schulze 1993)

$$a_c \approx \frac{1.9\varepsilon^{2/3}}{(R_b + R_p)^{1/3}} \tag{5.35}$$

where ε is the turbulent energy density. The force generated by the capillary pressure in the gas bubble that acts on the contact area of the attached particle (Figure 5.5d) is given by

$$F_\sigma \approx \pi R_p^2 \left(\frac{2\sigma}{R_b} - 2R_b \rho_\ell g \right) \sin^2 \omega \tag{5.36}$$

where σ is the surface tension, and ω is the angle specified inFigure 5.4. The capillary force exerted on the three-phase contact in the z-direction (Figure 5.5e) is

$$F_{ca} = -2\pi R_p \sigma \sin\omega \sin(\omega + \theta) \tag{5.37}$$

where θ is the contact angle. Finally, the hydrostatic pressure force (Figure 5.5f) of the liquid of height z_0 above the contact area of radius r_p (=$R_p \sin\omega$ in Figure 5.4) is

$$F_{hyd} = \pi R_p^2 \rho_\ell g z_0 \sin^2 \omega \tag{5.38}$$

Therefore, the net detachment force which acts on a bubble-particle aggregate is

$$F_{det} = F_{wt} + F_d + F_\sigma \tag{5.39}$$

and the net attachment force is given by

$$F_{ad} = F_{ca} + F_{hyb} \tag{5.40}$$

The stability of bubble-particle aggregates is then characterized by comparing the net detachment force to the net attachment force by the following dimensionless parameter, with $F_{hyd} = 0$ and F_{ca} replaced by the maximum capillary force F_{cam} (Schulze 1993),

$$Bo' = \frac{F_{detachment}}{F_{attachment}} \tag{5.41}$$

where

$$F_{attachment} = 4R_p^2 \left(\Delta\rho_p g + \frac{1.9\rho_p \varepsilon^{2/3}}{(R_p + R_b)^{1/3}} \right) + 3R_p \left(\frac{2\sigma}{R_b} - 2R_b \rho_\ell g \right) \sin^2 \left(\pi - \frac{\theta}{2} \right) \tag{5.42}$$

and

$$F_{attachment} = \left| 6\sigma \sin\left(\pi - \frac{\theta}{2} \right) \sin\left(\pi + \frac{\theta}{2} \right) \right| \tag{5.43}$$

As cited in Schulze (1993), taking into account the experimental results of Plate, a reasonable form for P_s is

$$P_s = 1 - \exp\left(1 - \frac{1}{Bo'} \right) \tag{5.44}$$

5.3.4 Conclusions

Using CFD it is possible to determine the hydrodynamics within a flotation system from which local turbulent dissipation rates and local collision rates can be obtained. Thus, CFD is potentially capable of relating flotation performance to cell design and operation. CFD modelling, has been used by Koh and Schwarz (2000, 2003, 2005) to simulate various types of flotation cell, including Metso, Denver and Outokumpu designs. Bubble-particle collision rates and efficiencies in different parts of the cell have been calculated from the local turbulent velocities, and the size and number concentrations of bubbles and particles obtained from CFD modelling.

5.4 Fine particle flotation

5.4.1 Reasons for low recovery of fine particles

The size at which a particle becomes a "fine particle" is defined as the size finer than the minimum for optimal flotation recovery (Subrahmanyam & Forssberg 1990).

The reasons for the low performance of flotation on fine particles are usually explained by the three distinct characteristics related to their small size: small mass, high specific surface area and high surface energy (Soto & Barbery 1988, Subrahmanyam & Forssberg 1990).

The small mass of the particles causes a low flotation rate because of the lower probability of particle bubble collision and adhesion (Soto & Barbery 1988, Lange et al. 1997, Feng & Aldrich 1999, Liu et al. 2002, Pyke et al. 2003). In fact all particle–bubble collision models described previously show that P_c decreases with decreasing particle size and increasing bubble size. Fine particles have low probability of collision with bubbles and are thus difficult to catch by bubbles, particularly by large bubbles. Dai et al. (1998) and Ralston et al. (1999a, 1999b) studied the effect of particle size on attachment efficiency both experimentally and analytically. They found that P_a decreases with increasing particle size and increases with increasing particle hydrophobicity. Yoon and Luttrell (1989) showed that P_a increases with decreasing induction time and decreasing particle size; P_a also increases with decreasing bubble size until the bubble size becomes too small. These conclusions are in agreement with Equation (5.28).

The high surface energy and high surface area result in high non specific reagent consumption, enhanced surface oxidation and solubility, which decrease selectivity (Soto & Barbery 1988, Gorman & Smith 1991, Lange et al. 1997, Song et al. 2001).

Among these factors, it is generally accepted that the main reason for the low flotation response of fine particles is the low probability of collision between particles and bubbles. This due to the tendency of fine particles to follow the liquid streamlines around the bubble (Yoon & Luttrell 1989, Matis et al. 1993, Ityokumbul et al. 2000, Mileva & Nikolov 2003) as a result of their low inertia.

A mineral particle will follow the liquid streamlines for a given bubble size if (Ityokumbul et al. 2000):

$$\frac{\rho_p d_p^2 U_b}{9\mu d_b} \ll 1 \tag{5.45}$$

Where ρ_p is the particle density, d_p the particle diameter, U_b the bubble rise velocity, μ the slutty viscosity, and d_b the bubble diameter. Therefore, fine particles will be able to collide with small bubbles only. Thus the use of small bubbles improves the flotation recovery since it increases the probability of collision between the particles and the bubbles.

In conventional flotation cells, only “macrobubbles” (600-2000 μm) are produced, to enhance the true flotation of fine mineral particles, small or mid size bubbles are required (40-600 μm).

5.4.2 Methods to improve fine particle recovery

Two main approaches have been used to achieve an improvement in fine particle flotation (Song et al., 2001):

- decrease the bubble size;
- increase the apparent particle size.

Several flotation technologies have been developed to achieve these two points. The latest point is obtained through several aggregation methods and the aggregated particles are then floated, a process known as floc flotation. Examples of technologies based on the use of small bubbles are dissolved air flotation, electro-flotation, and turbulent microflotation among others.

In this area, the chances offered by the use of waterjet, to both pulp agitation and bubbles generation, seem very attractive (Carbini et al. 1996, 1998, 2001, 2007; Chudacek et al. 1997).

In fact waterjet potential in flotation can be summarize as follows:

- capability of generating a high velocity water streams at least one order of magnitude higher than with mechanical impellers, even at relatively low pressures. This lead to an enhancement of aeration pulp. In fact it has been experimentally proven that the degree of aeration of the pulp in the form of small bubbles increases linearly with the relative velocity of the two interacting fluids (air and water) (Ciccu & Kursun, 2010);
- generation of small initial bubbles;
- even distribution of the bubbles into the vessel;
- generation of high turbulence into the vessel due to the feasibility of producing a number of superimposing whirls by suitably modifying the arrangement of the nozzles.

5.4.3 Previous works of waterjet-agitated cell

Experimental studies on the possibility of using high velocity water jets to create more suitable conditions in order to enhance the collection and separation mechanisms of a flotation process have been carried out since 1996 at the DIGITA Laboratories of the University of Cagliari.

In 1998 a first prototype of a waterjet-agitated flotation cell, named Hydrojet cell, was built. It consists of a cylindrical vessel, 200 mm in diameter and 400 mm high (total free volume 10.2 litres), provided with a hemispherical bottom screen for the discharge of the reject through a central outlet. Froths are skimmed out through a chute in the upper section of the cylindrical body.

The Hydrojet cell was tested on barite and zinc sulphide ore and on coal. Parallel series of flotation tests were carried out with waterjet and with a conventional impeller (Minemet), using the same cell and under common experimental conditions for the unbiased comparison of the results. Table 6 shows some of the experimental setting used.

The use of water jets for pulp stirring and bubbles generation produced:

- an improvement in the quality of the floated products;

- a higher recovery. This is probably due to an increase of bubble-particle collision probability enhanced by the presence of bubbles which are smaller (and hence much higher in number for a given overall air flow), faster and better distributed in the cell than in the case of mechanical agitation;
- a shorter flotation time to achieve a given recovery level due to a faster development of collection mechanism;
- a decrease in energy consumption.

In conclusion the application of water jets to flotation process appears corroborated by the experimental tests carried out on sulphide ores, coal and industrial minerals.

Table 4: Experimental setting Hydrojet cell (Carbini et al. 1998a, 1998b, 2001, 2007)

Pressure [MPa]	Nozzle diameter [mm]	Air flow rate [Nl/min]	Rotational speed [rpm]	Optimum pressure value [MPa]	Ore tested
From 4 to 14	0.3 mm	From 2.55 to 10.2	2000	9	Coal, Barite ore, Zinc sulphide ore

5.5 Waterjets

A water jet is formed as the high pressure fluid exits through a small opening called nozzle into a region of less pressure. Assuming the fluid jet exiting the nozzle as in the ideal case, there is a rotationally symmetric flow with a constant speed over the cross sectional of pipe. This simplification will neglect the pipe and nozzle friction for an incompressible flow. Therefore the exit velocity v_2 can be estimated. According to the Bernoulli equation, the equilibrium equation (the inlet is indexed as 1, and the outlet side is 2) can be established as in

$$p_1 + \rho_1 g h_1 + \frac{1}{2}\rho_1 v_1^2 = p_2 + \rho_2 g h_2 + \frac{1}{2}\rho_2 v_2^2 + \Delta p \tag{5.46}$$

where Δp is a pressure loss in the nozzle (energy that is lost because of friction in the nozzle). In order to calculate the theoretical maximum possible energy conversion in the nozzle, the pressure drop is neglected as in ideal case, i.e. $\Delta p \approx 0$. The height difference between inlet and outlet is negligible especially in horizontal arrangement, i.e.$h_1 = h_2$. Let $p_2 \rightarrow 0$ and $v_1 \rightarrow 0$, then simplification of Equation (5.46) becomes Equation (5.47) below:

$$p_1 = \frac{1}{2}\rho v_2^2 \tag{5.47}$$

After rearranging the Equation(5.47), it will give the exit velocity, v_2 as in Equation (5.48).

$$v_{2,th} = \left(\frac{2p_1}{\rho_w}\right)^{0.5} \tag{5.48}$$

Where the subscript *th* represents the theoretical value of the jet exit velocity.

So the velocity of the water at the exit of the nozzle does not depend on the geometrical characteristics of the nozzle.

In practice the jet velocity is somewhat less that the theoretical value because wall friction, fluid flow disturbances, etc. Therefore the actual jet speed is a fraction of the theoretical:

$$v_2 = \xi \left(\frac{2p_1}{\rho_w} \right)^{0.5} \tag{5.49}$$

The values for ξ, called speed point, are given in the literature from 0.95 to 0.99.

Furthermore the jet contraction should be taken into account. It is described by the contraction number μ defined as the ratio between the minimum beam cross-sectional area after leaving the nozzle to the nozzle cross-sectional area itself:

$$\mu = \frac{A_{min}}{A_0} \tag{5.50}$$

Often $\mu$and ξ are used together to calculate the coefficient of discharge:

$$C_D = \mu\xi \tag{5.51}$$

Chapter 6 PIV Bubble Column

6.1 Introduction

In this chapter the results of the PIV measurements in a bubble column are presented. The measurements reported were supported by the Laboratory of the Multiphase Reactors Group (SMR) at the Technical University of Eindhoven in the Netherlands.

The challenge in applying PIV to multiphase flows is in separating the tracer particles tracking the entrained continuous phase from the dispersed phase. Up to the present no comprehensive method for discerning the phases of multiphase flows has been developed.

During the period spent at the University of Eindhoven, the main purpose was to develop a simple method of phase-separation based on standard image analysis tools. This methods will be presented in this chapter.

6.2 Experimental procedure

Measurements were done on a glass bubble column with dimensions $0.15 \times 0.15 \times 1$ m^3 filled with water to a height of 0.45 m. The air was injected from a perforate plate with 9 holes with diameter of 1 mm at a square pitch of 6.25 mm which were positioned in the middle of the column. The airflow rates in the experiments were 12.5 L/min at standard temperature and pressure. The water flow was seeded with polystyrene particles with a diameter of 50 μm and a density of 1030 kg/m^3.

The experimental setup was a LaVision FlowMaster PIV system which consists of a Double pulsed Q-switched Nd: YAG laser (wavelength 532 nm, 320 mJ/pulse), an HighSpeedStar CMOS camera (1024 x 1024 pixel resolution), a HighSpeed Controller, a DaVis FlowMaster software and a PC. A beam expanding lens was used to create a lightsheet with a thickness of around 3 mm.

The field of view of the camera was 15 x 15 cm. The PIV measurements were performed on the first 15th centimetres of the column. Velocity fields are obtained for entrained fluid and bubbles in double-frame model. The time interval between image pairs was equal to 1 ms.

6.3 Phase separation method

The phase separation method developed uses standard tools available in most image analysis software. In this work ImageJ was used. It is a public domain Java image processing program.

Starting from the original image it's possible to obtain a mask in which seed particles and bubbles are separated by means of image processing techniques. This is achieved by taking advantage of the difference in size and intensity between bubbles and tracer particles. Whenever this mask is subtracted from the original image one obtains an

image that contains only tracer particles. Then, subtracting the tracer particle image from the original image one obtains an image that contains only bubbles.

The procedure that leads to the definition of the mask consists of six steps:

1 Median filter;
2 Subtract background from the original image;
3 Canny-Deriche edge detection;
4 Binarize image;
5 Removal of outliers,
6 Morphological filters.

The first step involves the use of a 2D-median filter in order to remove, from the raw image (Figure 6.1-a), the tracer particles signal that can be considered an image noise. In fact a median filtering is a nonlinear process useful in reducing impulsive, or salt-and-pepper noise. It is also useful in preserving edges in an image while reducing random noise. In a median filter, a window slides along the image, and the median intensity value of the pixels within the window becomes the output intensity of the pixel being processed. An important parameter in using a median filter is the size of the window. For the image shown in Figure 6.1-b a 4x4 pixels window size was used, based on the tracer particle size.

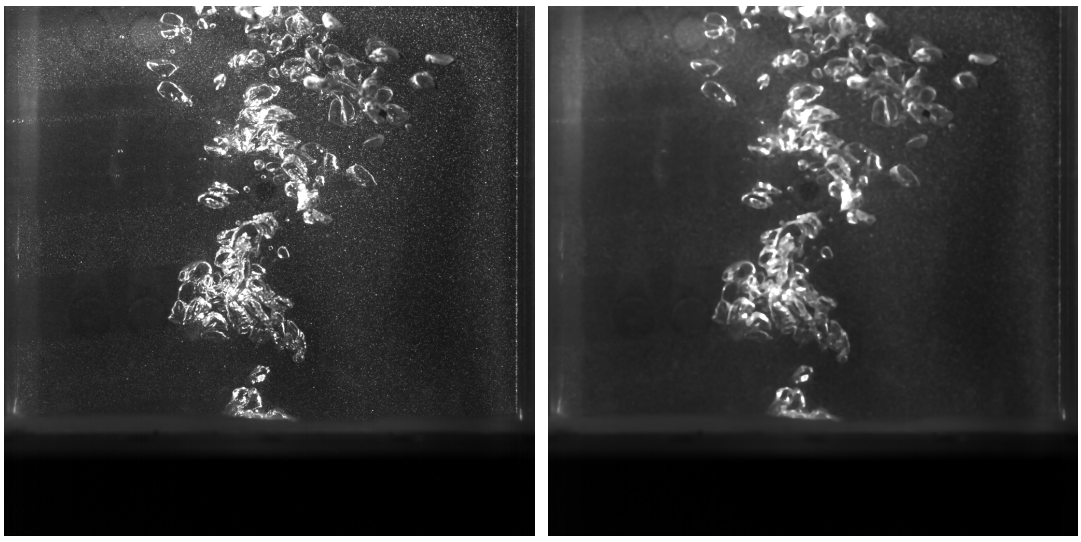

a) b)

Figure 6.1: a) Original image b) Filtered image

The aim of the second step is to correct uneven illuminated background by using a “rolling ball” algorithm. A local background value is determined for every pixel by averaging over a very large ball around the pixel. Thereafter this value is subtracted from the original image, so as to remove large spatial variation of the background intensities. The input parameter is the ball radius. This value should, at least, equal to the size of the largest object that is not part of the background. For the images shown in Figure 6.2 it was used a radius equal to 20 pixel.

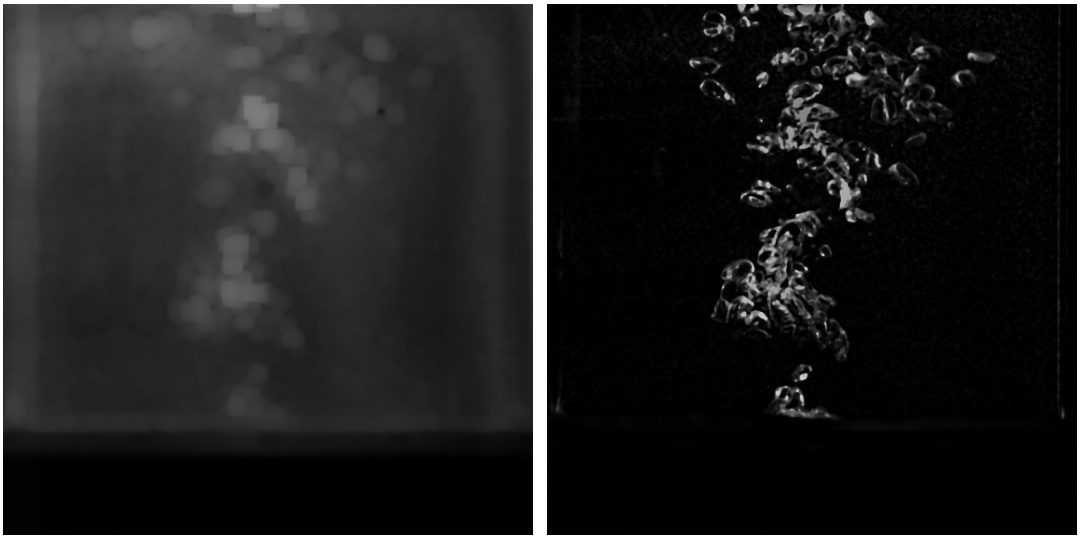

a) b)

Figure 6.2: a) Background image b) Image after background subtraction

The third step consists of applying the Canny-Deriche edge detector, which was derived from similar mathematical criteria as the Canny edge detector, though starting from a discrete viewpoint and then leading to a set of recursive filters for image smoothing instead of exponential filters or Gaussian filters.

The ImegeJ plugin calculates and shows both the raw Deriche norm (smoothed gradient) and the non-maximum suppressed norm. A parameter, (alpha), controls the degree of smoothing applied and its value can be chosen between 0 and 1; whilst greater values imply less smoothing but more accurate detection, the lower values imply more smoothing but less accurate detection. The raw Deriche norm has been used to perform the following step.

For the images shown in Figure 6.3 an alpha value equal to 0.5 was used.

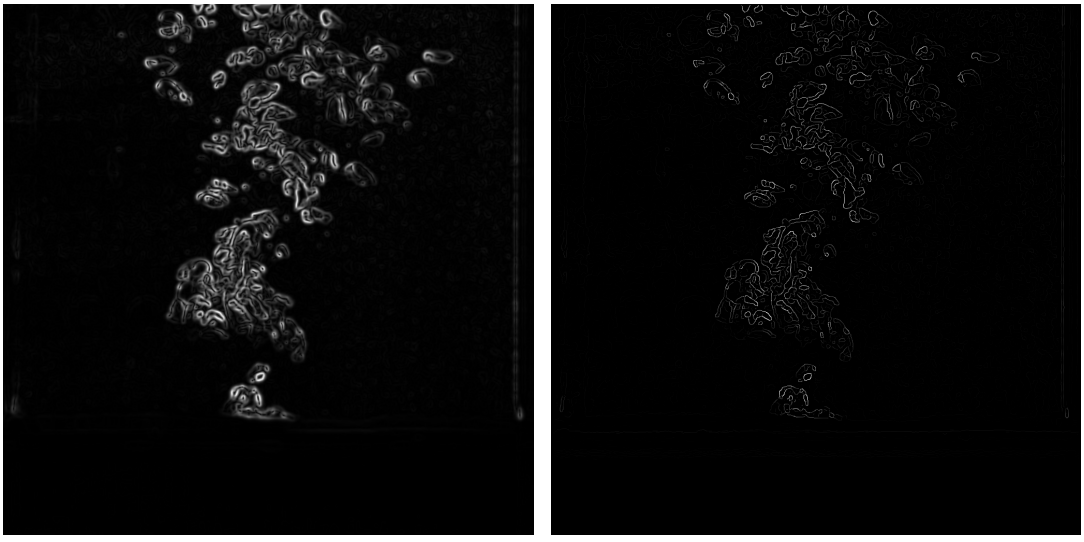

a) b)

Figure 6.3: Image after application of Canny-Deriche filter: a) raw Deriche norm, b) non-maximum suppressed norm

The fourth step converts the grey scale image into a binary image. This is achieved by comparing the intensity (named, grey value) of each pixel with a given threshold value; all pixels with a grey scale value above the threshold value are considered to be part of an object, and so their intensity value is set equal to 1. Whereas all pixels with a grey value below the threshold value are part of the image background and so their intensity value is set equal to 0. In digital image processing, there are several methods available that yield a threshold level on the basis of histogram information.

In the proposed method a semi-automatic process is used to determine the threshold which uses the histogram of the initial image after applying the first two steps. The optimal threshold value is quantified as the intensity value corresponding to a percentage of this histogram area. This percentage is chosen on the basis of visual evaluation.

Once this value is determined for a time series, the threshold value is calculated for each image based on its histogram. For the image shown in Figure 6.4-a a threshold value correspond to 90% of the histogram area was used. As shown Figure 6.4-a the binary image contains not so well defined bubble edges. However, due to the impossibility of eliminating completely the uneven illumination, it also contains typically small size contours which don't correspond to bubbles, that are characterized by small size. In order to eliminate them a second median filter, with the same size window of the previous one, is applied (Figure 6.5-b).

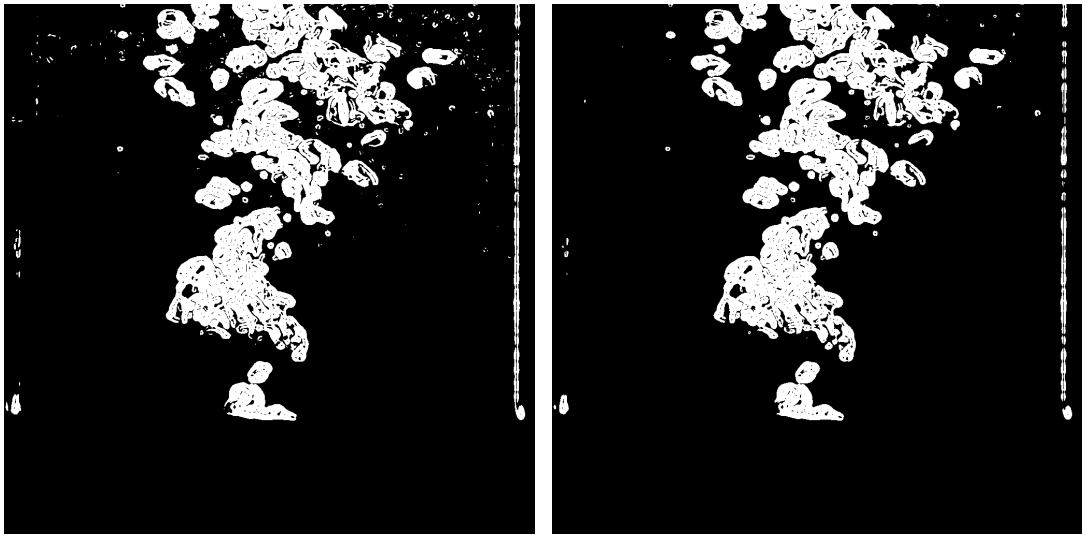

a) b)

Figure 6.4: a) Binary Image obtained by segmentation b) Result after median filtering

As mention before, the bubbles contours are not well defined. For this reason two morphological filters are applied.

In an image the dilatation filter adds pixels to the boundaries of objects. The number of pixels added from the objects in an image depends on the size and shape of the structuring element used to process the image. In the example in Figure 6.5 a 4x4 pixels circle structuring element was used. During the morphological dilatation, the state of any given pixel in the output image is determined by applying a rule to the

corresponding pixel and its neighbours in the input image. The value of the output pixel is the maximum value of all the pixels in the neighbourhood of the input pixel.; if, in a binary image, the value of any of pixels is set to 1, so is the value of the output pixel.

The close filter fills gaps and enlarges protrusions so as to connect objects that are close to each other. In the example in Figure 6.5-a 10x10 pixels circle structuring element was used.

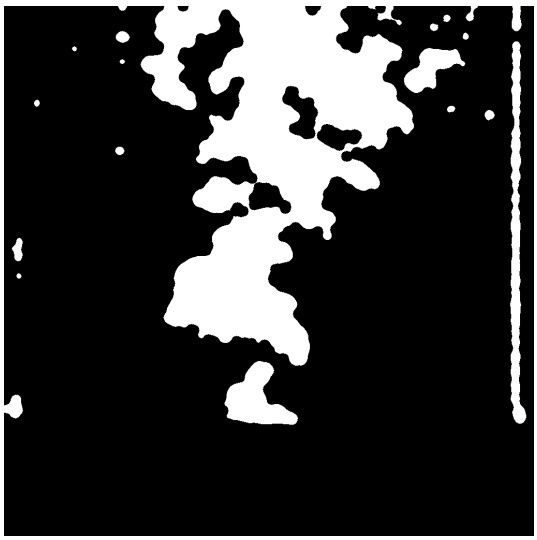

Figure 6.5: Image after applying morphological filters

The resulting mask (Figure 6.5) subtracted from the original image gives an image which contains only tracer particles (Figure 6.5-a). Subsequently subtracting this image from the original one, an image is obtained in which the bubbles are present (Figure 6.6-b).

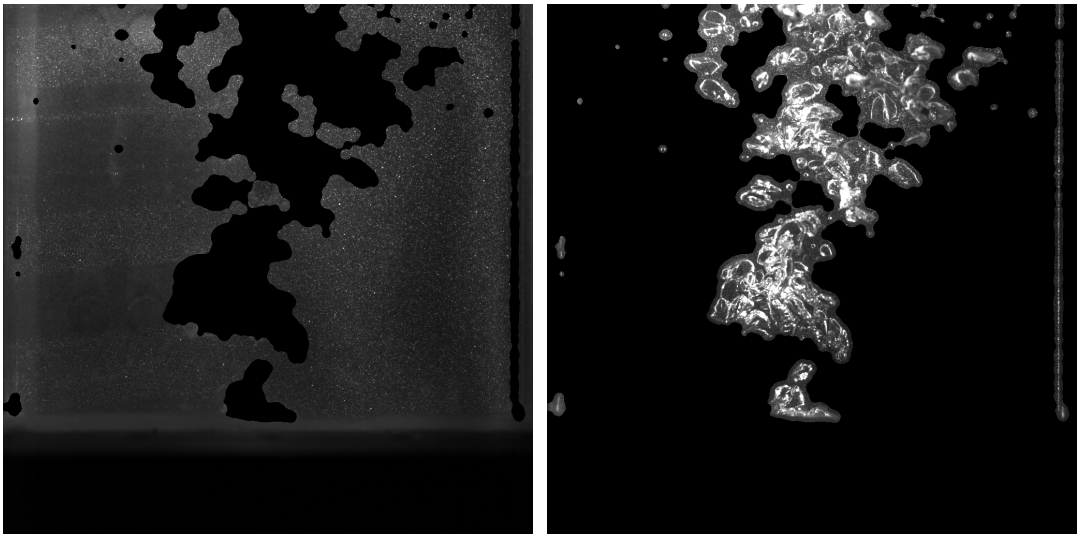

a) b)

Figure 6.6: a) Tracer particles image b) Bubbles image

An ImageJ macro has been written to perform automatically the steps previously described.

After being acquired, the images are extracted from DaVis 8.0 creating a time series.

The necessary parameters are chosen on the basis of size and intensity characteristics of bubbles and tracer particles (window's size of median filter, ball's radius, alpha parameter, percentage threshold histogram and morphological filters' dimension). By running the ImageJ macro two time series are obtained and then imported in Davis 8.0 for processing.

6.4 Data Analysis

The two sets of single-phase images obtained were processed using Davis 8.0 software where a multi-pass cross-correlation was used to determinate the displacement (velocity) vectors.

An interrogation window size of 32 x 32 pixels with 0% overlap was used to process the bubble images, while an interrogation window size of 32 x 32 pixels with 50% overlap was used to process the tracer particles images.

The obtained results were subjected to a post-interrogation procedure, median filter, in which spurious vectors were identified and subsequently discarded from the data set. Instantaneous flow fields of both phases are showed in Figure 6.7.

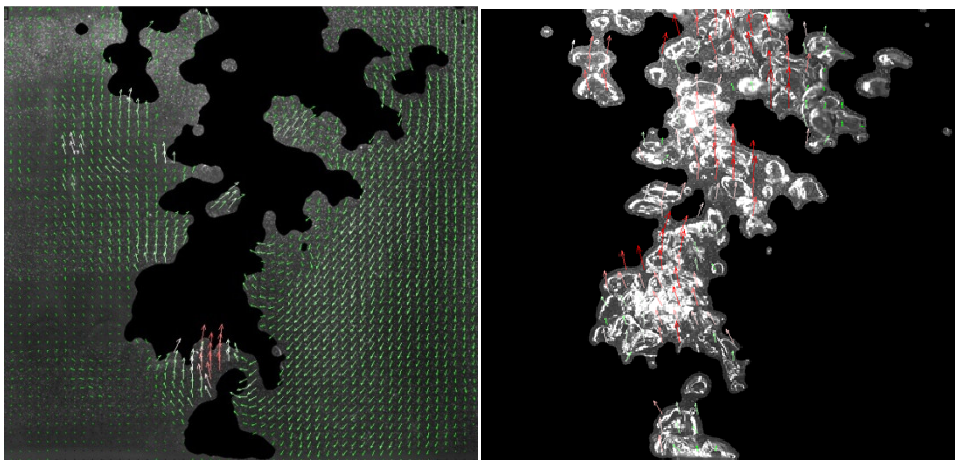

Figure 6.7: Instantaneous velocity vector plots of liquid (left) phase and the gas (right)

The resulting averaged radial velocity profiles of the gas and the liquid phase are shown in Figure 6.8. This figure shows the capability of the separation method to discriminate between the bubble plume and the continuous phase. The slip velocity measured is higher than the expected slip velocity of around 0.2 m/s. Which is probably a result of an insufficient acquisition time.

6.5 Conclusions

The phase separation method proposed is not meant to be better than the other phase separation methods but a simple end effective alternative to obtain the mean flow characteristics of a bubble plume.

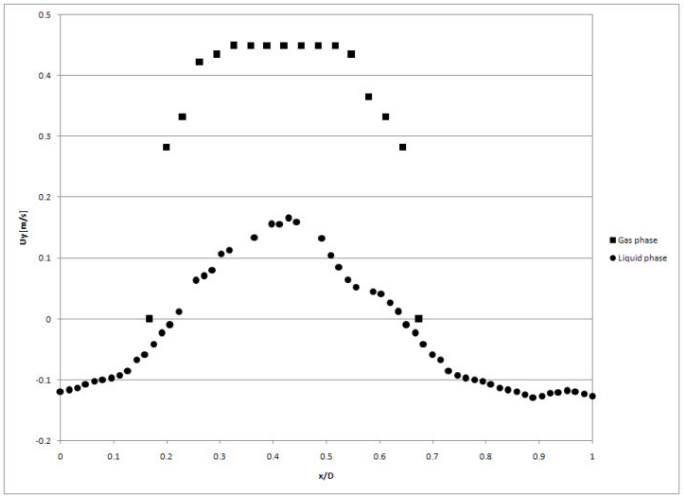

Figure 6.8: Axial velocity profiles at a height of y/H = 0.2 and a depth z/W= 0.50 of the gas and liquid phase.

The described technique leads to a digital mask by which a mixed-fluid image can be separate into two single-phase images. The mask relies on the existence of a significant difference in size and intensity of the particles constituent the two phases. Application of the mask was demonstrated with a test case performed in a square bubble column. The acquired images were pre-processed to obtain the singe-phase images. The two sets of images were processed using a standard PIV method and then time-averaged to obtain the average velocity field data for the bubbles and the liquid phase. The measured liquid velocities in the central part of the cell are significantly lower than those of the gas phase, this demonstrate the capacity of the method to discriminate between the two phases. Slip velocity values higher than those expected are thought to be due to a too short acquisition time which does not allow to calculate a steady time average (i.e. free from wiggles). For this reason the PIV measurements could not be used to validate the numerical simulations. Instead the simulations were compared with the available experimental PIV data of Deen (2001).

Chapter 7 Numerical Simulations of Flow in a Bubble Column

7.1 Introduction

In this chapter the 3D transient numerical simulations of the flow pattern in a square bubble column are presented. The geometry of the bubble column simulated is equal to the one used during the experimental part, with the exception of the gas inlet, which is a perforated distributor plate having 7 x 7 (49) holes with a diameter of 1 mm and a pitch length of 6.75 mm, positioned in the middle of the column, as in the work of Deen (2001). The solver that was used is based on the finite volume method, and the Euler model was adopted to simulate the gas-liquid flow. Two different models to calculate the turbulent viscosity were used: LES and SST model. Various closure models were examined in order to study the effect of the interface forces on gas-liquid flow behaviour. The simulation settings will be presented before discussing the results.

7.2 Simulation settings

The flow was simulated using the governing equations presented in Chapter 2. LES model and SST model were used to modelled the turbulent viscosity. Different interfacial closure models reported in the literature (Section 2.8.5.3) were examined along with the LES model. A summary of the different settings which were used is reported in Table 5.

Table 5: Overview of models

Case	Δt	μ_{eff}	M_I	**Model**
1	0.0025 s	LES, BIT	M_D	Ishii & Zuber (1979)
2	0.0025 s	LES, BIT	M_D M_{VM}	Ishii & Zuber (1979) C_{VM}=0.5
3	0.0025 s	LES, BIT	M_D M_L	Ishii & Zuber (1979) C_D=0.5
4	0.0025 s	LES, BIT	M_D M_L M_{VM}	Ishii & Zuber (1979) C_D=0.5 C_{VM}=0.5
5	0.005 s	SST, BIT	M_D M_L M_{VM}	Ishii & Zuber (1979) C_D=0.5 C_{VM}=0.5

The total domain was subdivided into uniform computational grid cells with $\Delta x = \Delta y = \Delta z = 0.5\ mm$.

When SST model was used, a column height of 1 m with a water level of 0.45 m was simulated, which gives a total of 18000 hexahedral cells. While, when LES model was used, due to difficulties in convergence, a column height of 0.45 m was simulated, thus a total of 81000 hexahedral cells form the computational domain.

The inlet of the bubble column was modelled as a fully open inlet, as in the work of Deen (2001), in a central area of 6 × 6 grid cells, which gives an inlet area $A_{inlet} = 0.03 \times 0.03$ m².

The inlet boundary condition was modelled as a velocity inlet, in which the velocity and volume fraction of the fluid were specified. The velocity value normal to the inlet was calculated as follows

$$u_{y,G} = \frac{u_{G,s} W \times D}{\alpha_G A_{inlet}} \tag{7.1}$$

where $u_{G,s}$ is the superficial gas velocity, $W \times D$ is the cross sectional area of the column (0.15 ×0.15 m²), and α_G is the gas volume fraction.

For a superficial gas velocity of 4.9 mm/s, as in the PIV experiments (Deen 2001), and a gas volume fraction of 1.0, the gas velocity at the inlet becomes 0.12 m/s.

The diameter of gas bubbles was set to 4 mm as in the work by Deen (2001).

An opening boundary condition and a gas volume fraction of 1.0 were applied at the outlet and no slip boundary conditions were applied for both phases along the walls.

In the simulations, to discretize the convection terms two schemes were used:

- high resolution scheme along with the SST turbulence model;
- central different scheme along with the LES turbulence model.

The flow was simulated for a period of 120 s. The data was time averaged over the last 110 s. For the LES, the simulations took about 6 days real time using a 3.4 GHz Intel(R) Core(TM) i7-2600 CPU PC with 15.9 GB of RAM.

7.3 Results

7.3.1 Turbulence models

As mentioned before, two different turbulence models were used: SST model and LES model. To evaluate the effect of the turbulence model, the two simulations that include all interface forces were compared (Cases 4 and 5). In Figure 7.1 and in Figure 7.2 snapshots of gas fraction iso-surfaces and liquid velocity fields are displayed for case 4 and 5. While Figure 7.3 and Figure 7.4 show, for the two cases, a time series of contour plots showing instantaneous gas volume fraction in a diagonal cut plane.

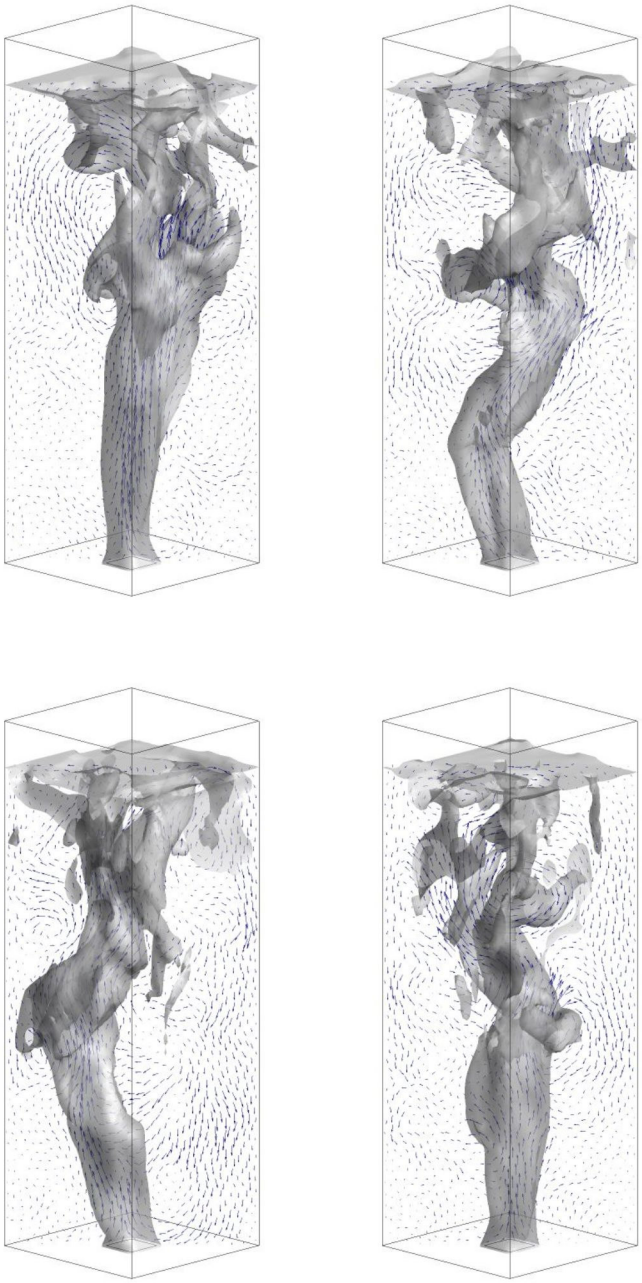

Figure 7.1: Snapshots of the instantaneous liquid velocity fields and iso-surfaces of α_G =0.04 at 5s intervals from 100s to 115s - Case 4 (LES)

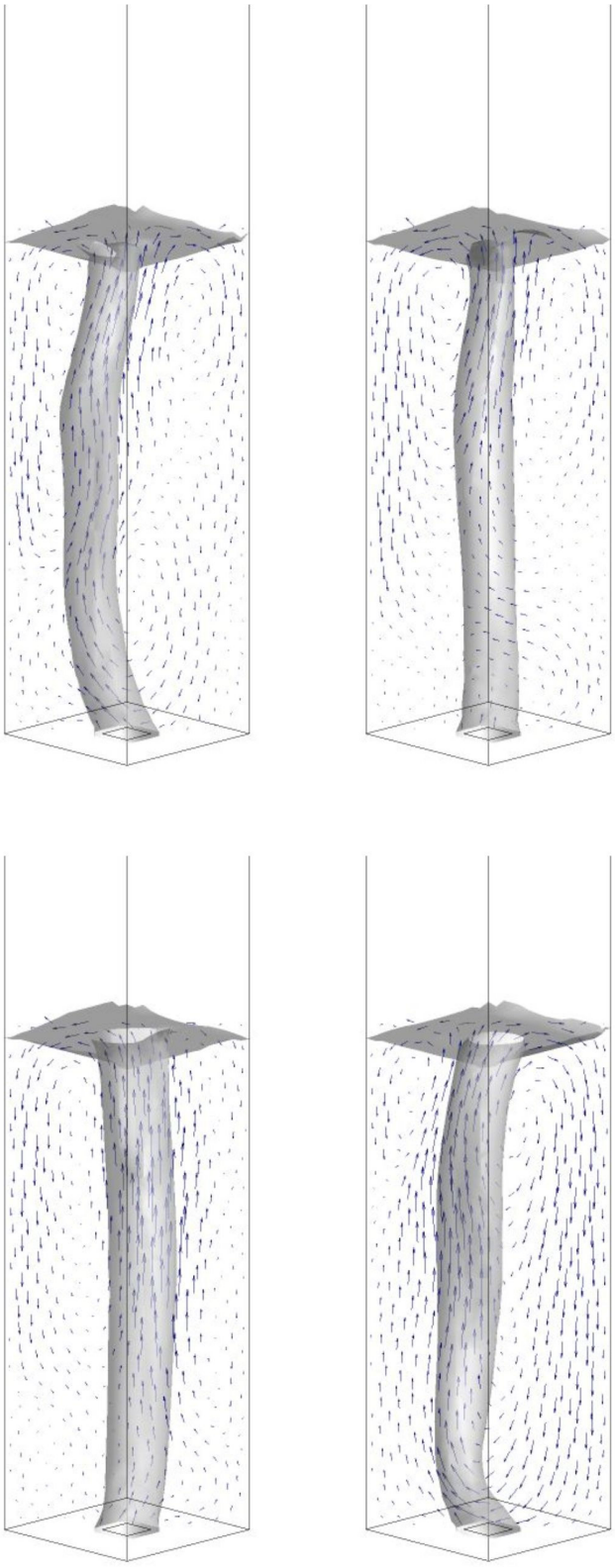

Figure 7.2: Snapshots of the instantaneous liquid velocity fields and iso-surfaces of α_G =0.04 at 5s intervals from 100s to 115s - Case 5 (SST)

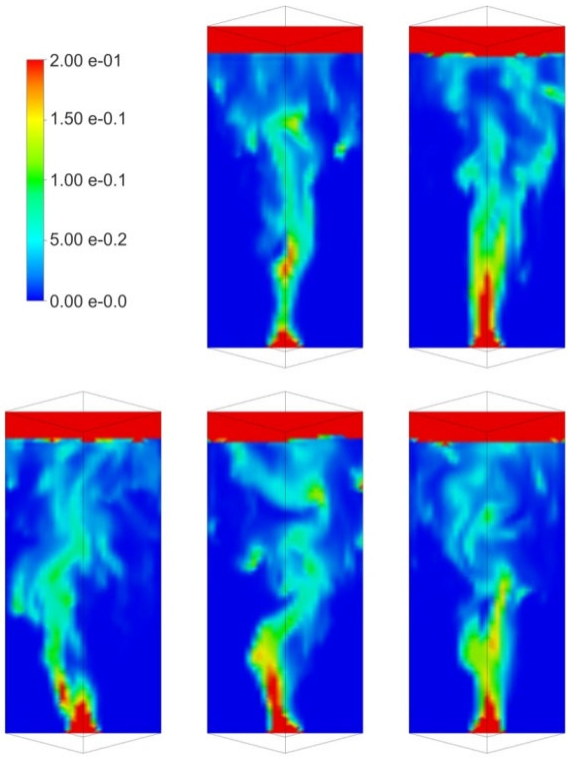

Figure 7.3: Contour plots of the instantaneous volume fraction of gas in a diagonal cut plane at 5s intervals from 100s to 120s. Case 4 (LES)

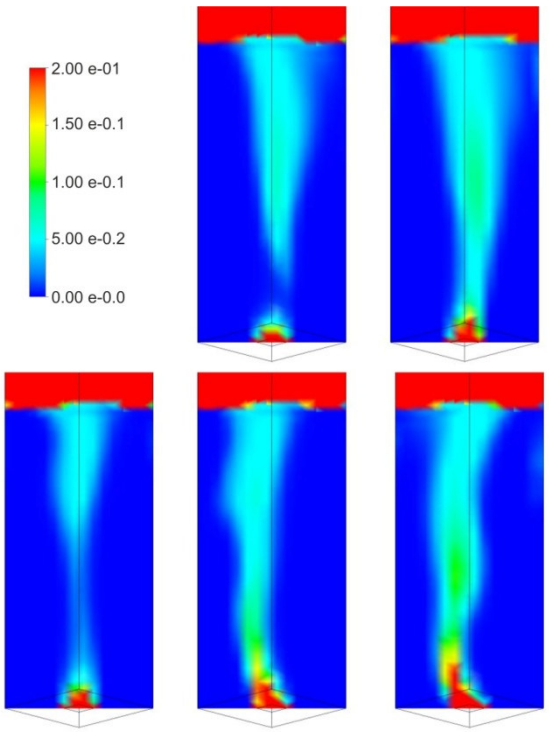

Figure 7.4: Contour plots of the instantaneous volume fraction of gas in a diagonal cut plane at 5s intervals from 100s to 120s. Case 5 (SST)

These figures show the capability of both models of simulating the bubble plume oscillations. The substantial difference lies on the level of detail with which the flow is resolved. In fact the LES model has the capacity of simulating the flow in detail simulating the fluctuations of the bubble plume. Along the plume several larger and smaller vortices coexist, which stagger on each other and change their size, shape and position with time. The velocity vectors exhibit a high degree of randomness, in agreement with experimental observations.

Conversely the SST model has not the capacity to capture in detail these fluctuations. Big liquid vortices which move downwards on the lefthand and righthand sides of the column are responsible for the oscillatory motion of the bubble swarm. This because of the averaging procedure on which the method is based on, thus all small-scale velocity fluctuations are enclosed in the turbulent kinetic energy k, leading to a smooth meandering plume.

A better comparison between the two models, can be done comparing the velocity fields. Figure 7.5 and Figure 7.6 show the average axial velocity profiles at a height of 25 cm and at a half of the depth for liquid and gas. The figures also illustrate the experimental profiles obtained from PIV experiments (Deen, 2001). It can be see that the SST gives asymmetrical profiles, though in the right order of magnitude. For both phases, the maximum average velocity predicted is higher than the one experimental measured. While the LES gives a more symmetrical velocity profiles and shows good agreement with the PIV data. The difference in velocity between liquid and gas phase, known as slip velocity, is about 22 cm/s for both turbulence models, close to that expected (20 cm/s).

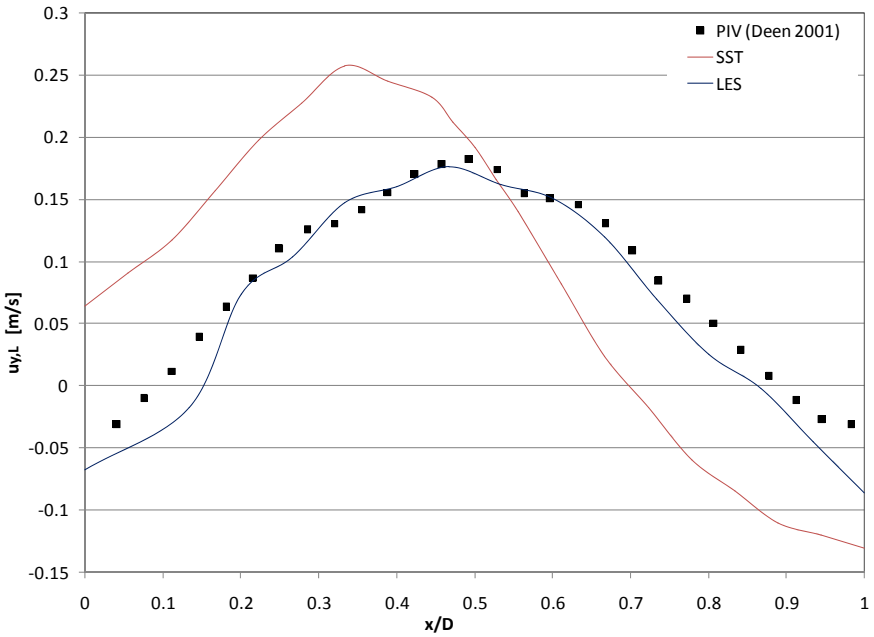

Figure 7.5: Comparison of simulated and experimental profiles of the axial liquid velocity (Cases 4 and 5)

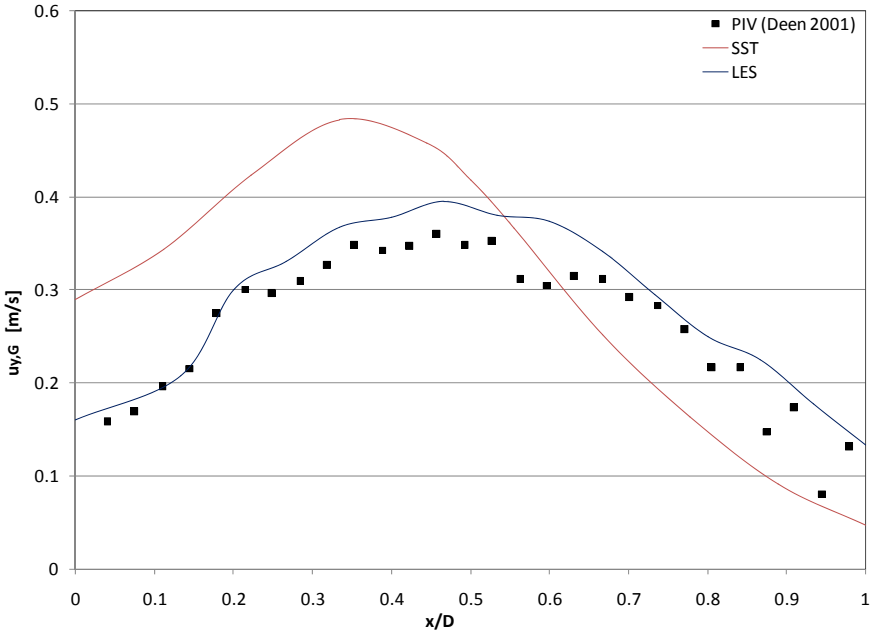

Figure 7.6: Comparison of simulated and experimental profiles of the axial gas velocity (Cases 4 and 5)

A further comparison can be made by means of the velocity fluctuations. In the SST model the velocity fluctuations are not resolved but contained in the turbulent kinetic energy, k (Deen, 2001). Assuming local isotropy of the turbulence, the velocity fluctuations in each direction can be derived as follows:

$$\overline{u_L'^2} = \overline{v_L'^2} = \frac{2}{3}k \tag{7.2}$$

In the LES the velocity fluctuations can be derived from Statistical Reynolds Stresses. A Reynolds Stress component can be evaluated using the difference between the running arithmetic average of the instantaneous velocity correlation and the running arithmetic average of the instantaneous velocities as:

$$\overline{u_i' u_j'} = \overline{u_i u_j} - \bar{u}_i \bar{u}_j \tag{7.3}$$

Figure 7.7 and Figure 7.8 show the profiles of the radial and axial fluctuations of the liquid velocity. It is clear that the that the assumption of isotropy is not valid. The SST predicts to low axial fluctuations velocity. While the axial fluctuations velocity profile predicted by the LES fits well the PIV data. The radial fluctuations velocity profiles of both models don't agree so well with the experimental data, although in the right order of magnitude.

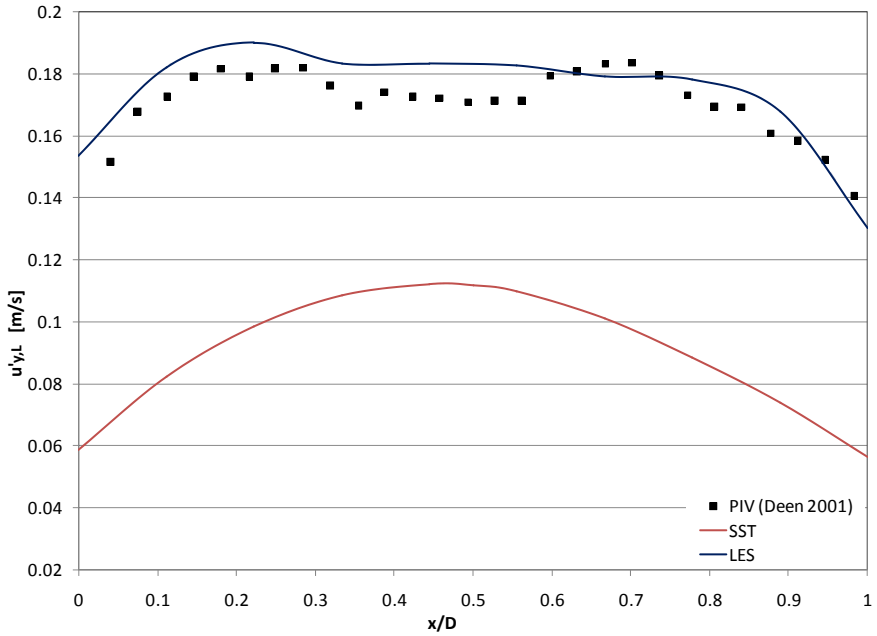

Figure 7.7: Comparison of simulated and experimental profiles of the axial liquid velocity fluctuations (Cases 4 and 5)

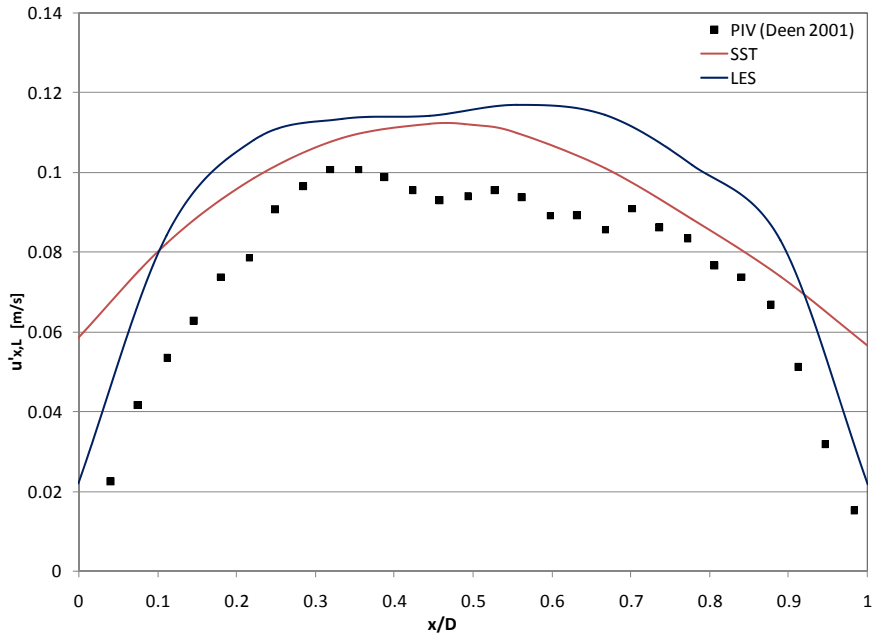

Figure 7.8: Comparison of simulated and experimental profiles of the radial liquid velocity fluctuations (Cases 4 and 5)

7.3.2 Interface models

To show the effect of the different interface forces for the LES the profiles of time averaged simulated axial liquid velocity at a height of 25 cm and a depth of 7.5 cm are show in Figure 7.9.

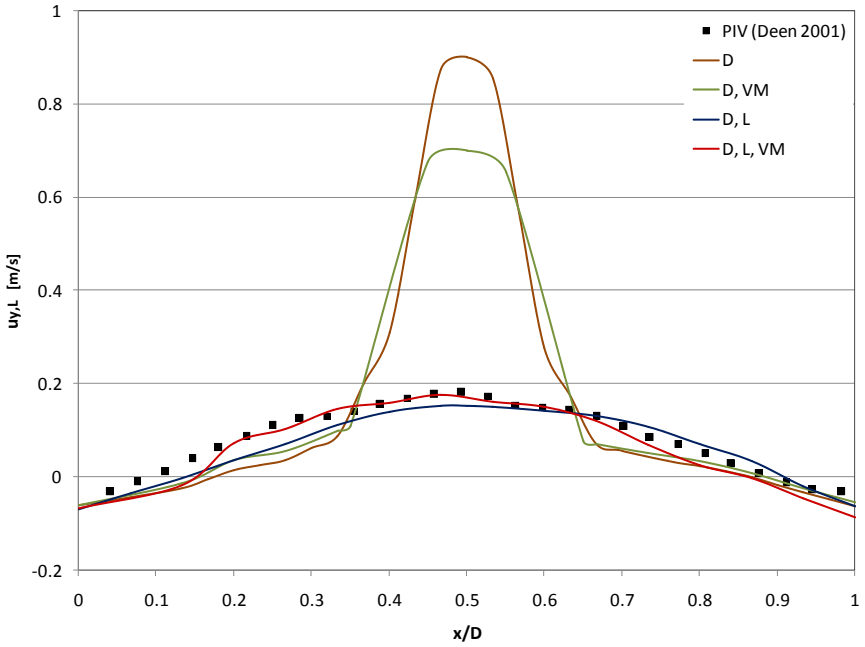

Figure 7.9: Comparison of simulated and experimental profiles of the axial liquid velocity for different interfacial forces (Cases 1,2,3 and 4)

From this figure it is clear that when only the drag force is included no radial fluctuation of the bubble plume is predicted. The plume rise straight to the top of the column, without transversal spreading. Thus the liquid velocity profile presents a strong peak in the centre, where the gas is rising and moderate downflow alongside the plume. There are not substantial differences in this behaviour when the virtual mass force is also considered. It can be see only a reduction of the peak in the centre of the column. So the influence of the virtual mass force is small.

When the drag and the lift forces are included, fluctuations of the bubble plume in the radial direction are predicted. Thus the lift force is responsible for transient spreading of the bubble plume across the cell. The predicted velocity profile match well the PIV data. Addition of the virtual mass force yield only to a simulated velocity a little bit lower in correspondence to the centre. So it is evident that the core velocity is simulated suitably with drag force and lift force. However, when only these two forces are incorporated the predicted profile of axial liquid velocity fluctuations (Figure 7.10) presents higher values than expected close to the centre of the column. This behaviour does not occur when the virtual mass force is included. In this case simulated and experimental profiles are in good agreement. The incorporation of the virtual mass force does not produce a big change in radial velocity fluctuations. Both profiles (Figure 7.11) show the same trend, with values slightly higher than those measured.

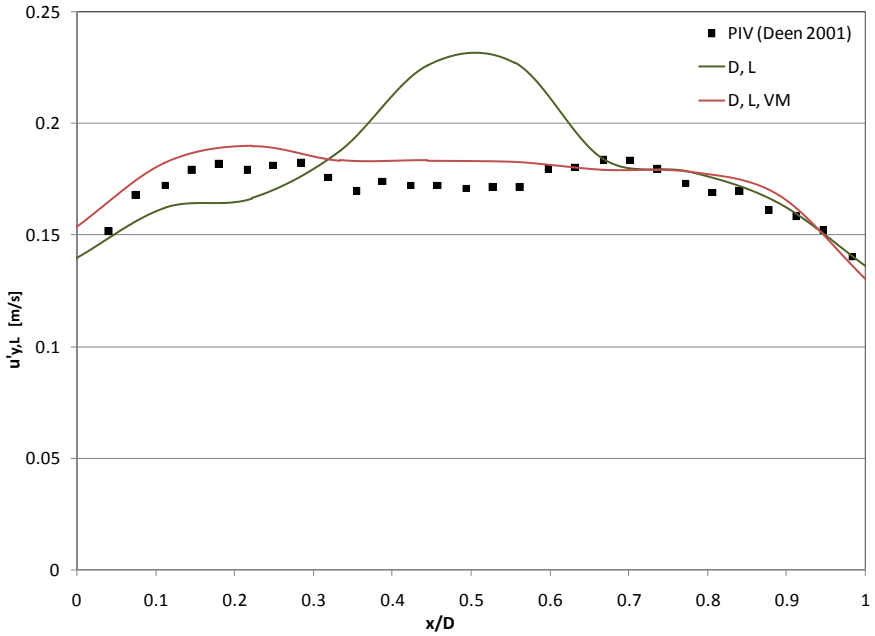

Figure 7.10: Comparison of simulated and experimental profiles of the axial liquid velocity fluctuations (Cases 3 and 4)

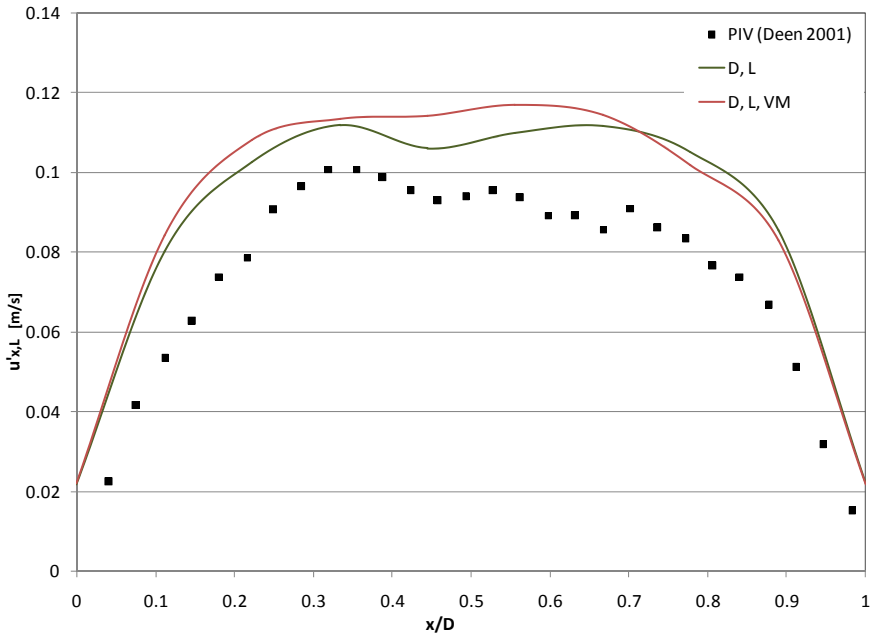

Figure 7.11: Comparison of simulated and experimental profiles of the radial liquid velocity fluctuations (Cases 3 and 4)

7.4 Conclusions

In this chapter a bubble plume in a rectangular bubble columns has been modelled with two different turbulence models along with different interfacial forces.

It has been shown that the SST turbulence model cannot reproduce all the complex turbulence characteristics of bubble column, as is instead able to do the LES model. The velocities and the velocity fluctuations simulated by the SST are anyway in the right order of magnitude. The simulations with LES model give velocity profiles and axial velocity fluctuations in good agreement with experimental data of Deen (2001), while the radial velocity fluctuation predicted are slightly higher than the PIV data.

The transient behaviour of the bubble plume can be modelled adequately by LES turbulence model, drag model by Ishii and Zuber (1979), a constant lift force with $C_L = 0.5$ and a bubble induced turbulence (BIT) as proposed by Sato and Sekoguchi (1975). The virtual mass force does not produce a substantial behaviour modification.

Chapter 8 Bubble Size Distribution in a Rectangular Cell

8.1 Introduction

It is clear, from what it was said in Chapter 5, the importance of the bubble size on flotation efficiency. One of the potentials offered by the use of the water-jet to improve the performance of the flotation process is the ability to generate bubbles of small diameter. To investigate this aspect, an experimentation was carried out in order to determinate the bubble size distribution (BSD) along the jet by the optical method.

In this chapter, the results from this experimentation will be presented along with the experimental set-up and the experimental procedure.

8.2 Experimental apparatus and procedures

Figure 8.1 shows a schematic diagram of the experimental set-up which consists of a rectangular cell, a high pressure plunger pump connected with a waterjet lance , and a compressed air duct. The cell is made of perspex and has a dimension of 50×5×50 cm^3. The waterjet lance is about 20 cm long and it ends with a calibrate nozzle with 0.5 mm diameter. It is powered by a Pratissoli high-pressure pump. The lance is housed in a flange which is connected with the cell. Along this flange, downstream the nozzle, is located a duct through which the air is injected.

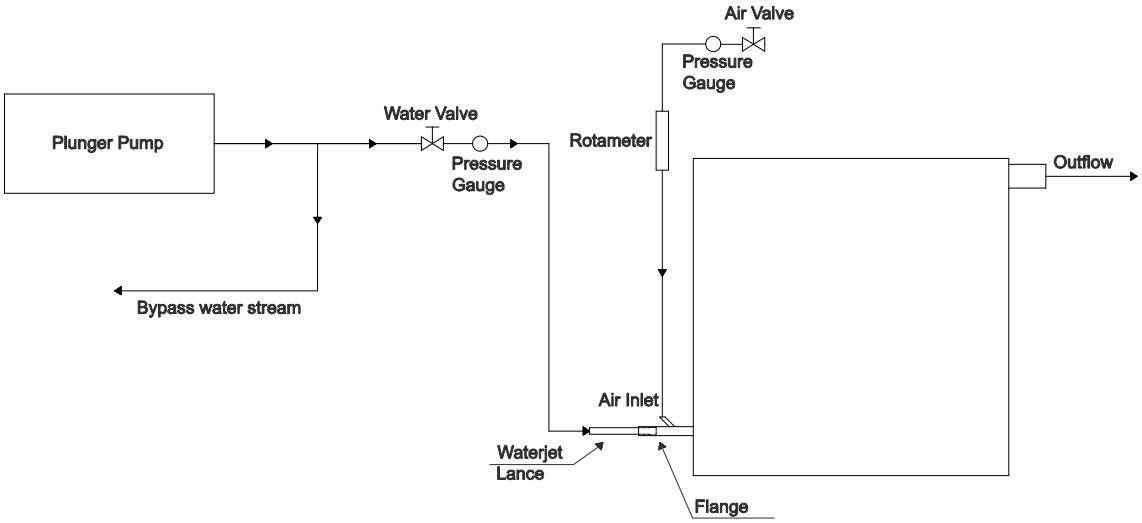

Figure 8.1: Schematic diagram of the experimental set-up

The measurements were performed using a SouthernVision Inc. MemView high speed camera positioned perpendicular to the jet axis. The back lighting method for measuring the sizes of bubbles was used The measurement area was illuminated with a halogen lamp (500 W) located behind the vessel. With this illumination apparatus only

low pressure waterjet could be tested, because an increase of the jet velocity requires a progressive reduction of the acquisition time and thus an increase in the light is required. Also due to the reduction of the light intensity by the light scattering from bubbles, it was not possible to perform measurement at the beginning of the jet. This area contains a very high concentration of bubbles, so it becomes too opaque to detect the bubble shadows among the background noise of the image.

Measurements were performed, for three pressure values 3, 4 and 5 MPa, in two axial locations A and B, positioned at 6.75 cm and 17.55 cm from the edge of the cell respectively.

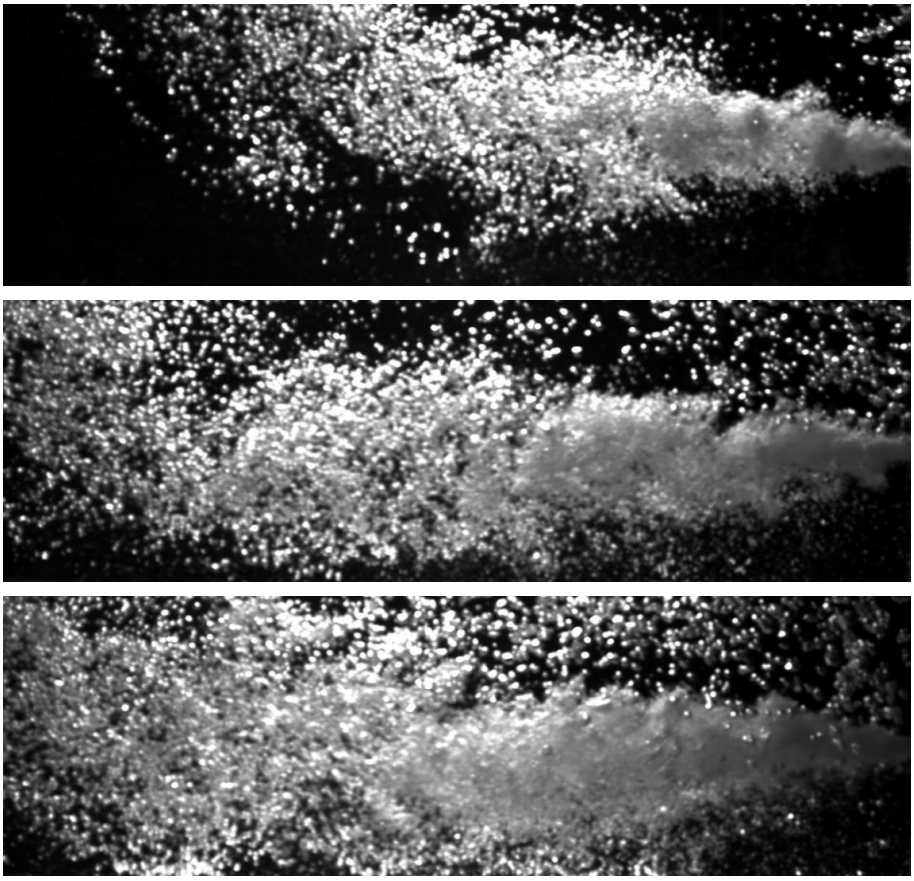

Figure 8.2: Air-Water jet generated at different pressures (3, 4 and 5 MPa)

In these tests the air flow was not imposed, but is the one that is dragged by the water jet. An overview of the experimental settings is given in Table 6. The measurements were done with a small camera aperture, so that the depth of field of the image is big. Only the bubbles in the measurement plane are in focus (Figure 8.3), i.e., they have sharp edges. Other bubbles generate out-of-focus images that disturb the measurement. The bubbles are distinguished as shadows, so that the pixel of the bubble image has much smaller brightness than the pixels representing the background.

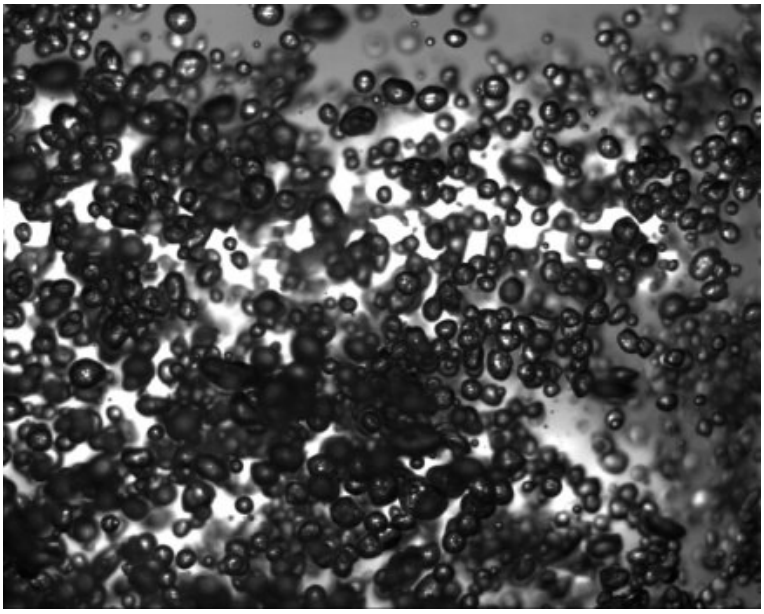

Figure 8.3: Example of acquired image

Table 6: Overview of the experimental settings

Pressure of pump [MPa]	Outlet velocity [m/s]	Nozzle diameter [mm]	coefficient of discharge	Water flow rate [l/min]	Air flow rate [nl/min]
3	77.5	0.5	0.63	0.58	4.2
4	89.4	0.5	0.63	0.66	4.4
5	100	0.5	0.63	0.74	4.6

Due to the continuous light source it was not possible to record sequential images with a short enough time delay. Since the recordings do not consist of image pairs, but of single images, the bubble velocities remain unknown. The bubbles were detected using a semi automatic detection method based on the differences in brightness between bubbles and background.

8.3 Results

For each experimental setting 50 samples were used to obtain statistics.

Figure 8.4 and Figure 8.5 show the histograms of the bubble size distribution relative to the positions A and B for the three pressure values tested. In Table 7 the descriptive statistics of the data are reported.

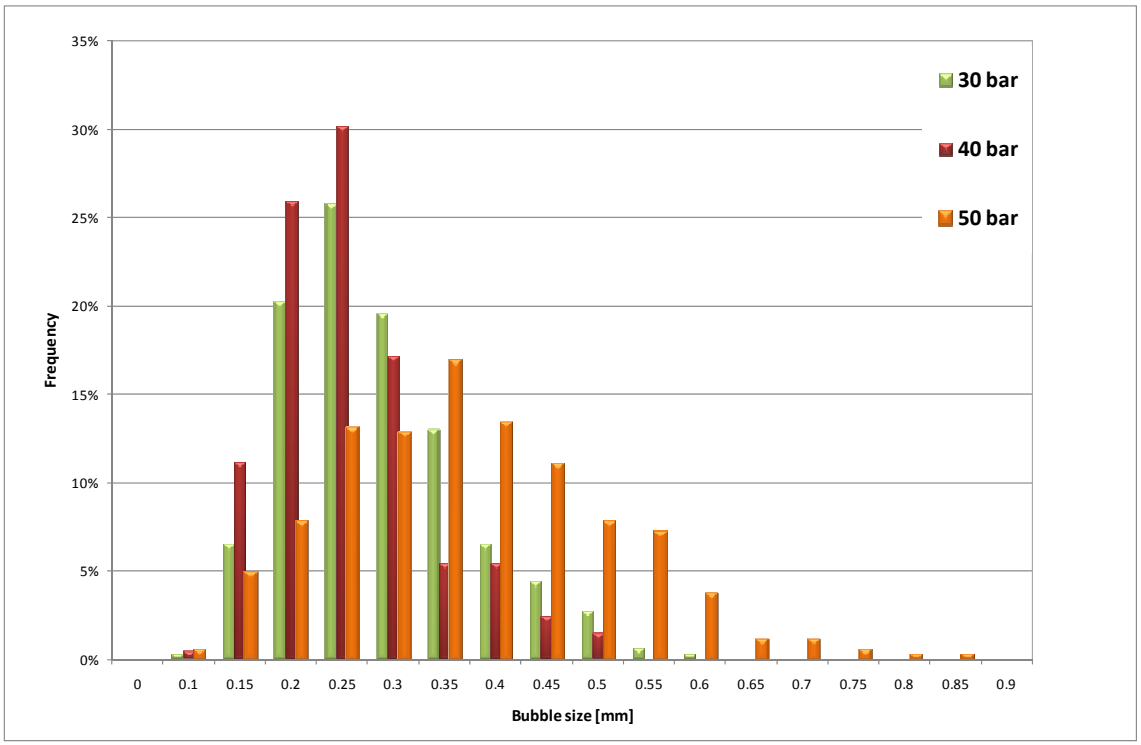

Figure 8.4: Frequency histograms of bubble size distribution at the location A

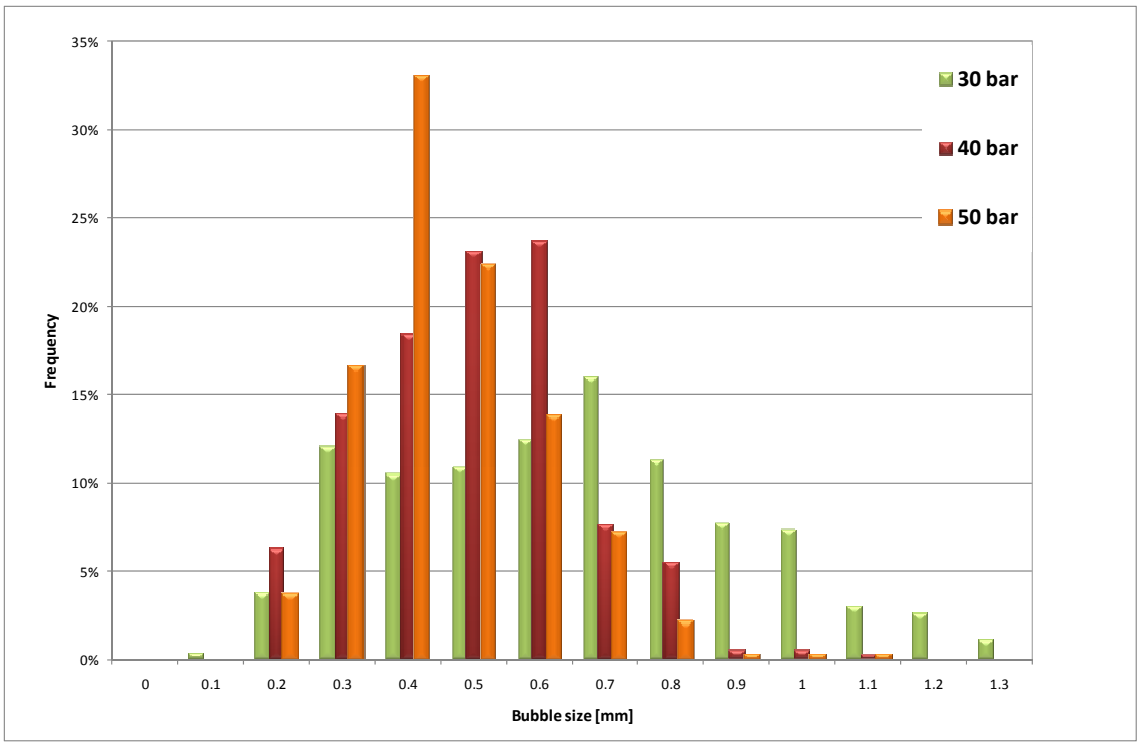

Figure 8.5: Frequency histograms of bubble size distribution at the location B

Table 7: Descriptive statistics of the data

	3 Mpa		4 MPa		5 MPa	
	Position A	**Position B**	**Position A**	**Position B**	**Position A**	**Position B**
Min	0.11	0.15	0.10	0.10	0.07	0.15
Max	0.82	1.27	0.58	1.06	0.49	1.06
Mean	0.35	0.60	0.26	0.45	0.23	0.42
Range	0.73	1.18	0.48	0.94	0.42	0.91
Standard error	7.28E-03	1.63E-02	5.07E-03	8.17E-03	4.18E-03	7.99E-03
Standard deviation	1.35E-01	2.62E-01	8.64E-02	1.59E-01	7.62E-02	1.42E-01
Variance	1.82E-02	6.84E-02	7.47E-03	2.54E-02	5.80E-03	2.03E-02
Kurtosis	0.136	-0.522	0.533	0.090	0.707	1.469
Skewness	0.482	0.313	0.838	0.283	0.867	0.853

It is seen that the bubble sizes in the location B are greater than in location A, and in all cases, the bubble size distribution was not symmetrical (normal distribution). The coalesced bubbles of location A go ahead and accumulate in the location B. This results in the wider bubble size distribution in the location B compared to location A.

The higher is the pressure, and thus the velocity of the jet, the higher is the air entrainment by the jet. Furthermore, an increase in pressure produces a reduction of the bubble size due to an higher momentum of the liquid jet

8.4 Conclusions

This experimentation shows the capability of water jets at moderate pressure to break an air stream into small bubbles. Increasing the pressure of the pump, smaller and more uniform bubbles were obtained. Also using moderate pressure, the dimensions of the generated bubbles were smaller than those generated by a traditional mechanical impeller in a flotation system.

Chapter 9 Numerical Simulations of Flow in the Hydrojet Cell

9.1 Introduction

In this chapter the steady numerical simulations of the Hydrojet cell are presented. The solver that was used is based on the finite volume method, and the Euler model was adopted to simulate the gas-liquid flow. To calculate the turbulent viscosity, the SST model was used. To simulate the rotation of the waterjet lance, a single reference of frame was used. The geometry of the experimental setup will be presented before discussing the numerical model and its results.

9.2 Hydrojet cell

In light of the promising results presented in Section 5.4.3, it was decided to scale up the Hydrojet system. Figure 9.1 shows a sketch of the laboratory plan and a sketch of the waterjet lance.

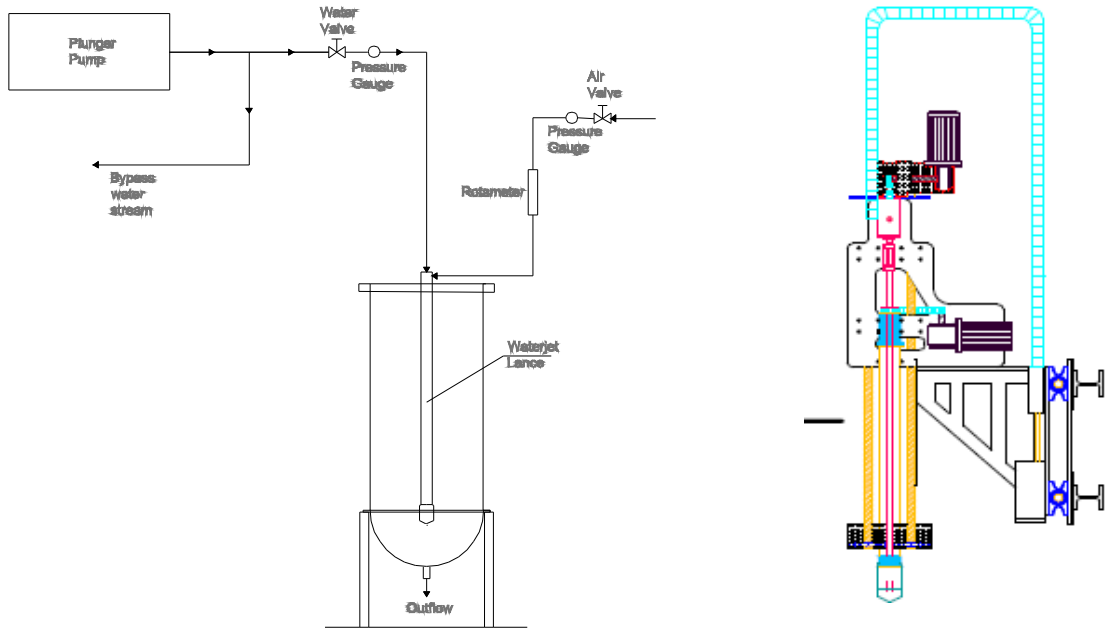

a) b)

Figure 9.1: a) Sketch of the laboratory plan, b) Sketch of the waterjet lance

The new experimental apparatus consists of a waterjet lance connected to a plunger pump, to a compressed air system, and to a supporting and guiding structure. A cylindrical vessel with a hemispherical bottom, 50 cm in diameter and 100 cm high, made of perspex, is located at the base of the supporting system. This system is equipped with a windlass and three electrical motors which permit the rotation as well

as the horizontal and the vertical translations of the lance, thus the lance positioning within the cell (Figure 9.2).

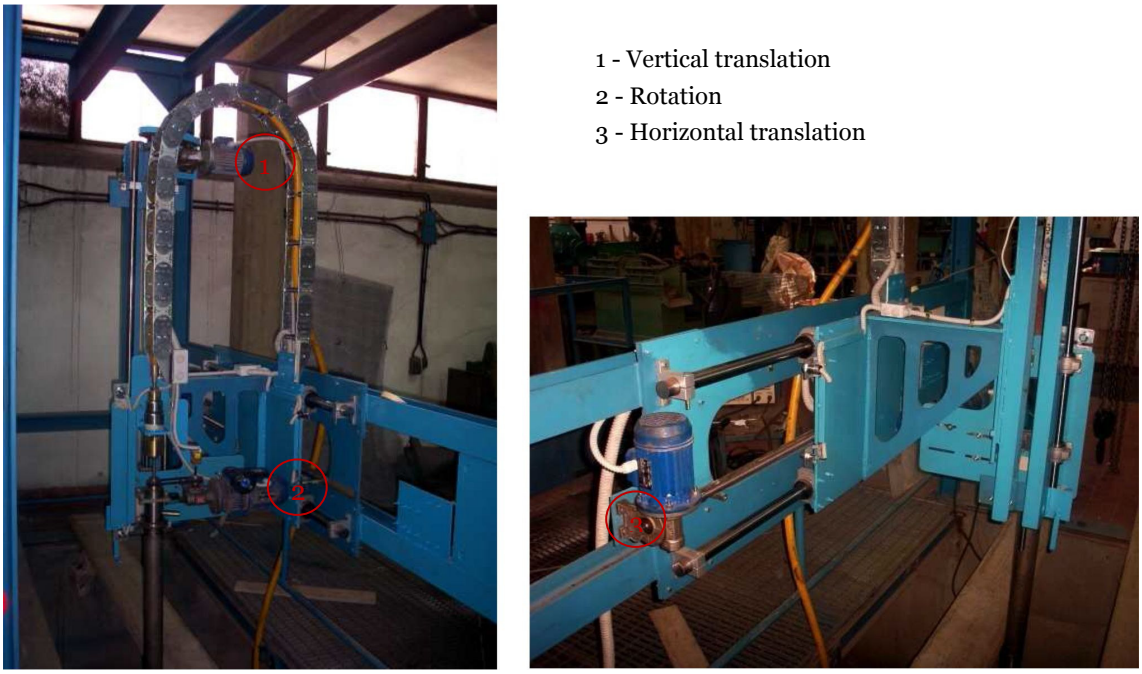

1 - Vertical translation
2 - Rotation
3 - Horizontal translation

Figure 9.2: Details of the guiding structure

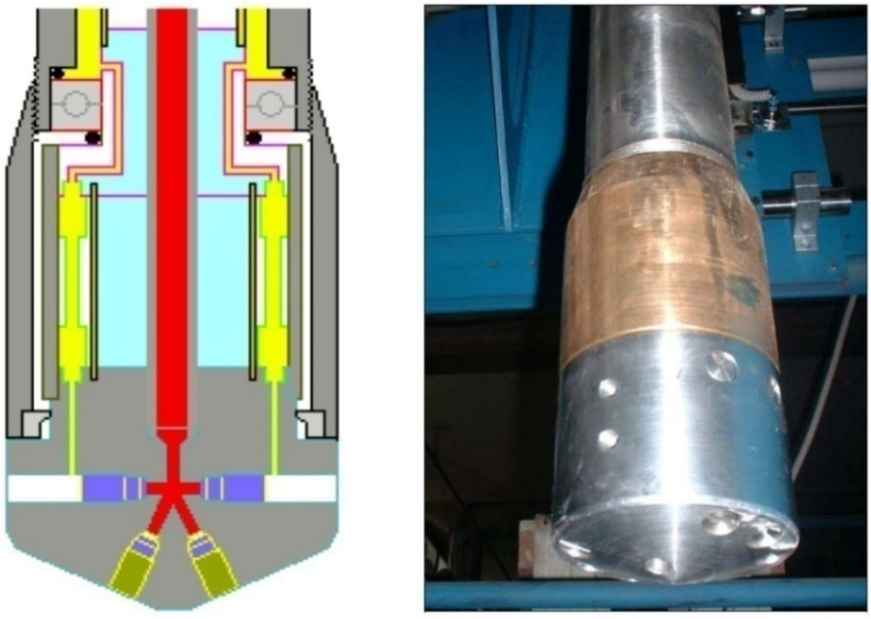

Figure 9.3: Details of the waterjet lance head

Translations and rotation of the lance are controlled by means of a control panel. The waterjet lance has a diameter of 8 cm. Pressurized water generated by the pump comes into the lance from the top by means of a swivel which connects a flexible high pressure pipe to the lance, while air is injected through a nozzle positioned in the upper part of

the lance. Pipes convey water and air to the bottom of the lance. A section of the lance head is presented in Figure 9.3. The transformation of the pressure energy into kinetics energy is obtained by means of calibrated nozzles positioned on the head of the lance. Several nozzles are contained in the lance head, in this work only the two positioned perpendicularly to the lance's rotation axis were used.

9.3 Numerical model

9.3.1 Numerical implementation

Modelling of the gas–liquid flow was carried out using an Eulerian two-fluid model. The flow was simulated using the governing equations, presented in Chapter 2.

Turbulence was solved using the SST model for the continuous phase and Dispersed Phase Zero-Equation model for the bubbles. Sato Enhanced Eddy Viscosity was used for turbulence transfer between the phases. The bubble–liquid interphase forces included were the drag force, lift force and virtual mass force. The Ishii-Zuber drag model was used to determine the draft coefficient of the liquid phase. The coefficients for both the lift and virtual mass force were set equal to a value of 0.5. The high resolution scheme was used to discretize the convection terms in the equations.

There are several modelling approaches for moving domains. The equations of fluid flow can be solved in a rotating reference frame by considering additional acceleration terms to the momentum equations. Thus solutions become steady with respect to the rotating reference frame. Due to the simple geometry of the Hydrojet cell, the entire computational domain was referred to a single moving reference frame. Single Frame of Reference (SFR) assumes all domain rotate with a constant speed with respect to a single specified axis.

A cylindrical vessel, 50 cm in diameter and 100 cm high, with hemispherical bottom, was modelled. The geometry included, in axial position, a cylindrical tube with diameter of 8 cm and 100 cm high. Two circular inlets were positioned at a distance of 5 cm from the bottom of the tube. Two inlet sizes were simulated: 10 mm and 2 mm. For the first configuration the whole cell was modelled. The relative computational grid is shown in Figure 9.4. While for the second configuration only 180° of the cell was modelled and the relative computational grid is shown in Figure 9.5. Table 8 reports some of the properties of the two grids.

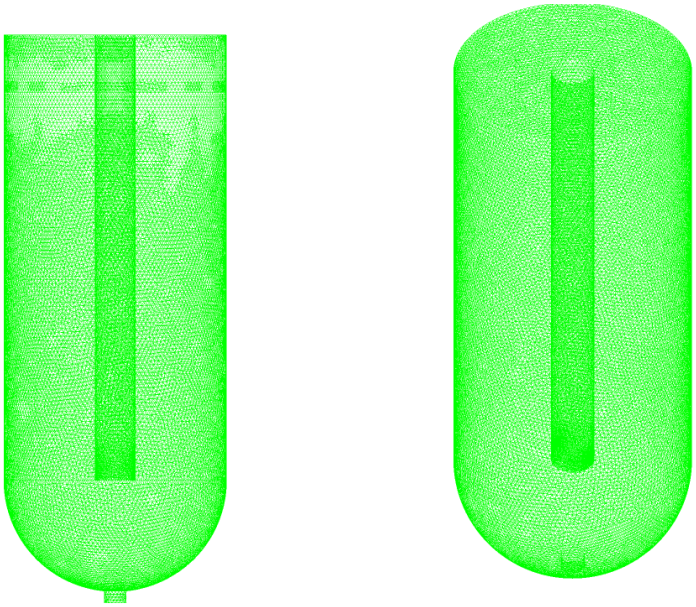

Figure 9.4: Computational grid - 360°

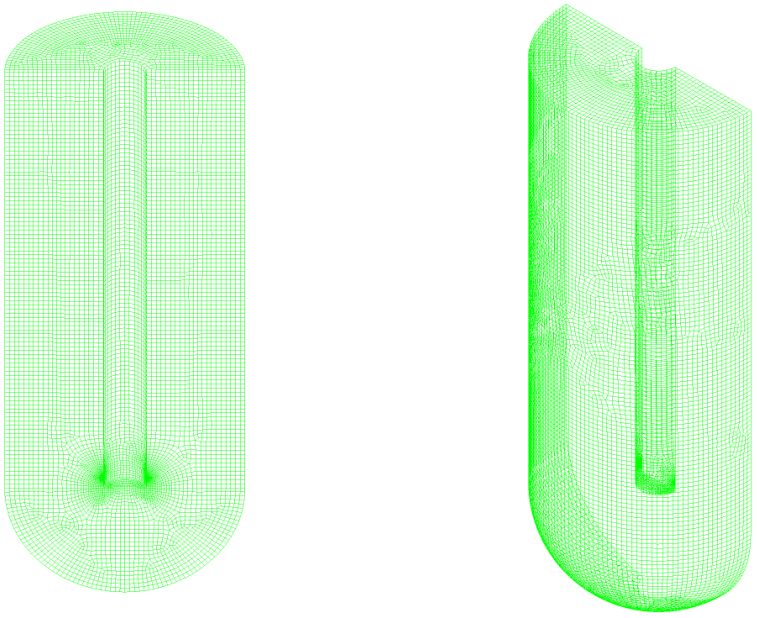

Figure 9.5: Computational grid - 180°

Table 8: Meshes composition

	N. of Elements	Tetrahedral	Pyramids	Wedges	Hexahedra	Max Edge Length Ratio	Skewness (average)	Aspect ratio (average)	Volume [m³]
Mesh 1	1780653	1138393	-	642260	-	43.31	0.18	5.6	0.22
Mesh 2	175921	13678	23618	2102	136523	23.70	0.22	2.6	0.11

9.3.2 Simulations

In the first two simulations the nozzles through which water and air flow into the cell were modelled as round orifices with a diameter of 10 mm. A bubble size of 0.5 mm was used. The inlet boundary conditions were modelled as a velocity inlet where the velocity and volume fraction of the fluid are to be specified. For both inlets ,the velocity was set equal to 100 m/s, which corresponds to a pump pressure of about 5 MPa. The gas volume fraction $\alpha_{G,in}$ was set equal to 0.13. The outlet, positioned at the bottom of the cell, was modelled as a pressure outlet where the air volume fraction is specified to be zero and the walls are modelled as no-slip boundaries for both phases. The liquid surface was modelled as a degassing boundary condition, which is used to model a free surface from which dispersed bubbles are permitted to escape, but the liquid phase is not. The rpm for the rotating domains was set at 60 and 120.

Figure 9.6 shows the volume fraction of gas in a horizontal plane passing through the axis of the nozzles obtained from simulations under the two different rotational speeds.

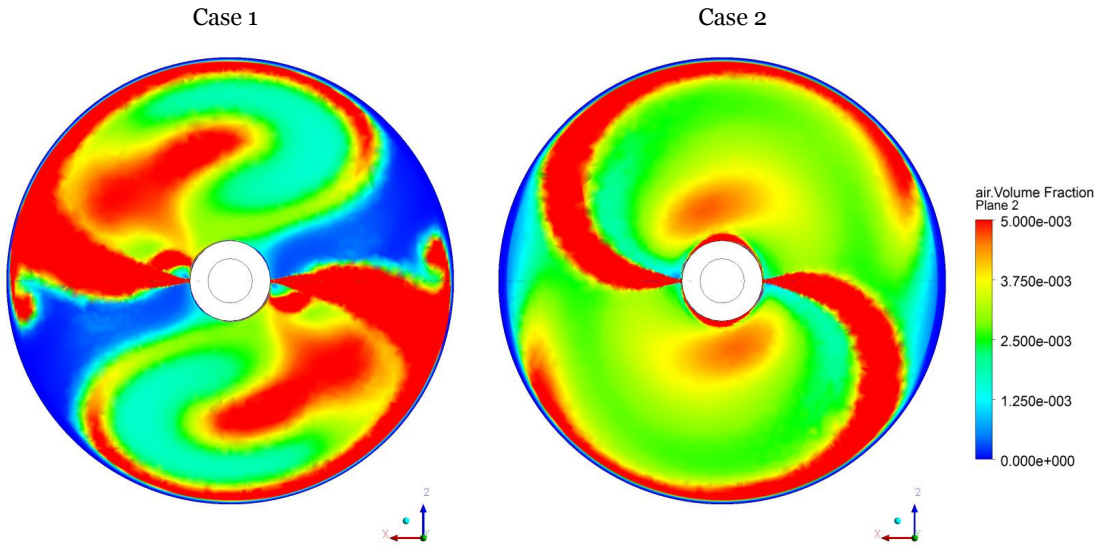

Figure 9.6: Gas volume fraction distribution in a horizontal plane passing through the axis of the nozzles (Cases 1 and 2)

In both cases the jets remain coherent till they intercept the cell wall where the bubbles tend to gather and rise to the top. This behaviour was also observed experimentally in a qualitative way. A rotational speed of 60 rpm is insufficient to ensure the spread of the bubbles across the whole cell section. A double rotational speed improves the mixing conditions but the gas fraction distribution is still concentrated along the wall of the cell.

To reduce the length of the area in which the beam is consistent, it is possible to use a nozzle with a smaller diameter. With this aim a new geometry having two inlets with diameter of 2 mm was adopted. The inlet boundary conditions were modelled again as a velocity inlet, different values of velocity and volume fraction were simulated. An overview of the simulations is shown in Table 9.

Table 9: Overview of simulations settings

	ϕ_{nozzle} [mm]	v_{inlet} [m/s]	α_G	ω [rpm]
Case 1	10	100	0.13	60
Case 2	10	100	0.13	120
Case 3	2	100	0.13	120
Case 4	2	200	0.13	120
Case 5	2	200	0.50	120
Case 6	2	300	0.50	120
Case 7	2	300	0.50	240

Figure 9.7 shows the volume fraction of gas in a horizontal plane passing through the axis of the nozzles resulting from the aforementioned cases.

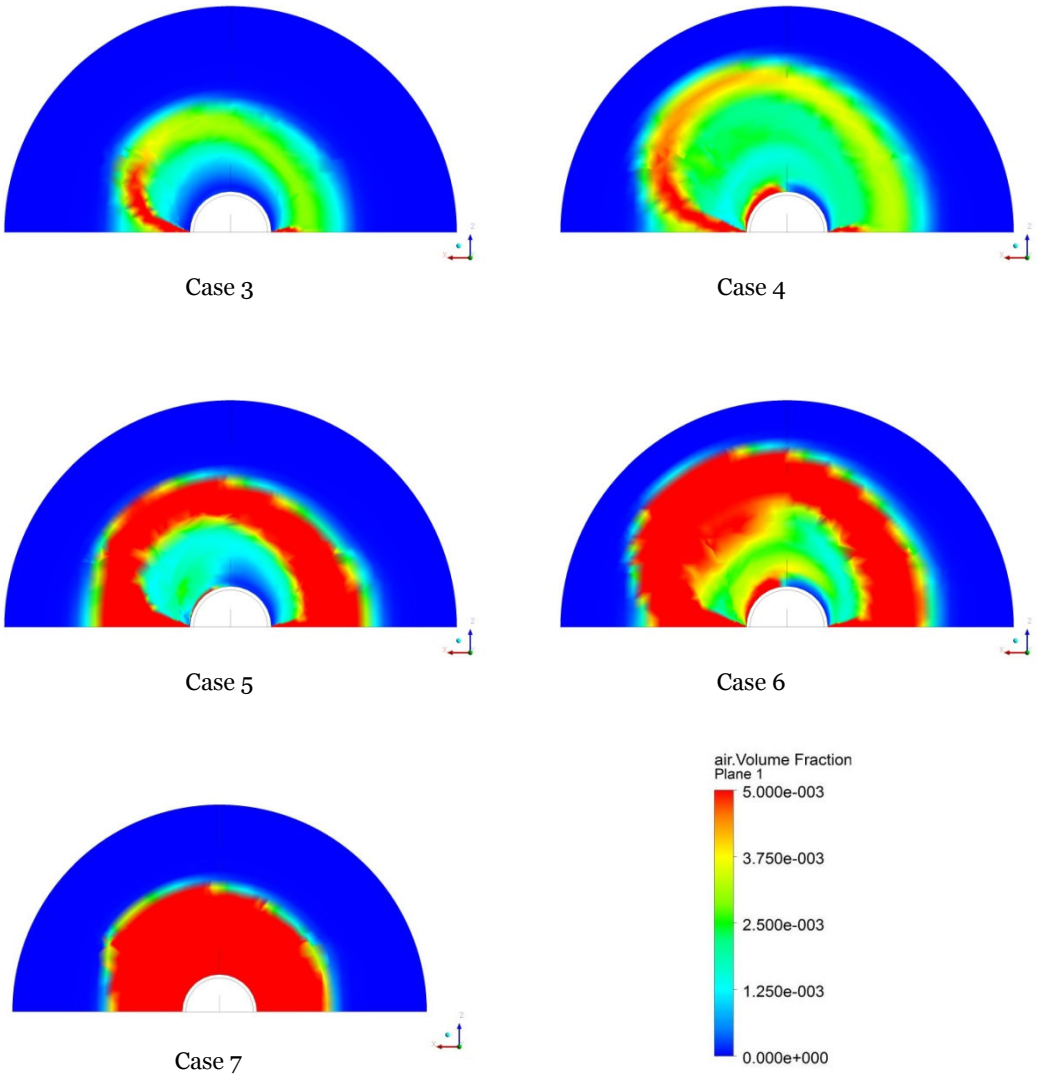

Figure 9.7: Gas volume fraction distribution in a horizontal plane passing through the axis of the nozzles (Cases 3, 4, 5, 6 and 7)

With a diameter equal to a quarter of the previous one under the same operating condition (which implies a reduction of sixteen times of the inlet mass flow), the area affected by the dispersion of the gas is approximately half of the entire section. With a velocity inlet equal to 100 m/s, the bubbles are spread across a circular area with a radius of about half of the radius of the cell. Increasing the inlet velocity up to 200 m/s (Case 4), and thus duplicating air and water inlet mass flow, the radius of influence increase of about 16%. A further increase of the air mass flow, set equal to 0.5 at the inlets in Case 5, does not increase the area affected by the dispersion of the gas. There is, however, an increase of the gas volume fraction in a narrow annular section at the boundary of the area. It is clear that the amplitude of the area affected by a higher value of gas increases as the input flow rate, as shown the comparison between Case 5 and Case 6. However the radial spreading of the gas phase is still non uniform. A more uniform distribution is obtained by increasing the rotational speed of the lance, which in Case 7 was set equal to 240 rpm.

9.4 Conclusions

The influence of the four main parameters that control the hydrodynamics of the process, nozzles diameter, speed of rotation of the lance, speed of generation of the jet, and then the pressure of the pump and inlet air flow rate, can be inferred from the simulations done. Among all parameters, it was found that the rotational speed of the lance plays a key role to ensure a uniform dispersion of the bubbles within the cell. At present this appears to be the weak point of the experimental apparatus which allows low rotation speeds, which are not able to ensure adequate dispersion. It was also observed that the nozzle diameter should be chosen carefully because too large diameters generated jets which stay coherent until impacting the cell wall, where the bubbles gather and rise to the top. As regards to the other parameters the existing equipment does not pose any limitation ensuring a wide range of variation. After choosing a suitable nozzle diameter, the inlet velocity and the inlet gas fraction should be selected to ensure a proper gas dispersion in the nozzles region.

At this stage of the study, focus on enhancing the Hydrojet system design setup, the results of the simulations have given important information about the performance required for the system to be capable of creating suitable conditions for an efficient flotation process. Future experimental measurements will allow an improvement of the numerical model, relating especially to the inlet condition settings, as well as its validation.

Chapter 10 Conclusions and Future Work

10.1 Bubble column

PIV measurements were performed in a square bubble column. A separation method was developed and tested. The proposed method leads to a digital mask by which a mixed-fluid image can be separated into two single-phase images. The mask relies on the existence of a significant difference in size and intensity of the particles that constitut the two phases.

The slip velocity measured is higher than the expected slip velocity of about 0.2 m/s. It is believed that this is the result of an insufficient acquisition time. Moreover, due to a no longer enough acquisition time a steady time average (i.e., free from wiggles) could not be calculated. So the PIV measurements could not be used to validate the numerical simulations. Instead the simulations were compared with the available experimental PIV data of Deen (2001).

Transient simulations of a bubble column were performed using the Eulerian approach, thus the dispersed and continuous phases are assumed to be interpenetrating continua and for each phase a complete set of Navier-Stokes equations are solved. Coupling between the momentum equations of the phases is achieved by implementing interphase momentum exchange terms into the respective phase's momentum balance equations.

For the continuous liquid phase, two different turbulence models were used: the Shear Stress Transport (SST) and the Large Eddy Simulation (LES). For the dispersed gas phase, the zero equation model was used. It was shown that the SST turbulence model cannot reproduce all the complex turbulence characteristics of the bubble column, as it is instead able to do the LES model. The velocity and the velocity fluctuations simulated by the SST are anyway in the right order of magnitude. The simulations with LES model gave velocity profiles and axial velocity fluctuations in good agreement with experimental data (Deen, 2001), while the radial velocity fluctuations predicted are slightly higher than the PIV data.

To conclude, the transient behaviour of the bubble plume can be modelled adequately by LES turbulence model, drag model by Ishii & Zuber (1979), a constant lift force with $C_L = 0.5$ and a bubble induced turbulence (BIT) as proposed by Sato and Sekoguchi (1975). The virtual mass force does not produce a substantial behaviour modification.

10.2 Hydrojet cell

Experimental measurements were performed in order to determinate the bubble size distribution (BSD) along the axis of a air-water jet. The high-velocity stream of water and air was generated by an high-pressure pump by means of a calibrated nozzle. The measures were performed via a photographic method at two positions along the jet axis and for three different pressure values. This experimentation showed the capability of

water jets at moderate pressure to break an air stream into small bubbles. Increasing the pressure of the pump, smaller and more uniform bubbles were obtained. The dimensions of the bubbles were smaller than those generated by a traditional mechanical impeller in a flotation system.

Steady simulations of the Hydrojet cell were carried out using the Eulerian approach. For the continuous liquid phase, the Shear Stress Transport (SST) turbulence models were used. For the dispersed gas phase, the zero equation model was used. Drag, lift and virtual mass forces were included in the simulations. A single frame of reference was used to simulate the rotation of the lance.

The results gave useful indications about the role of the four principal operating parameters: nozzles diameter, velocity of rotation of the lance, speed of the water jets and then pressure of the pump and inlet air flow rate. What emerges is the need of high rotational speed of the waterjet lance in order to ensure an uniform gas distribution within the mixing zone. This is not possible with the current apparatus. Thus in order to make the system suitable to produce an appropriate environment for the full development of the flotation process it is necessary to modify the system.

This confirms the importance of CFD as a powerful tool to improve the design of flotation system and to reduce scale-up problems.

10.2.1 Future work

On the basis of the conclusions drawn, some future work considerations are presented in the following.

Experimental work

Future experimental measurements are essential to improve the numerical model, especially regarding the more appropriate conditions to model the two inlet nozzles. Moreover, experimental measurements are crucial for the validation of the model. There is no safe procedure to judge CFD results without validation. It is therefore essential for a future development of the Hydrojet numerical model to carry out experimental measurements in order to determine turbulence velocity field in the cell as well as the bubble size distribution. The most frequently used methods to determine velocity field in gas-liquid system are laser-based, while the most frequently used bubble size measurement technique are based on image analysis. PIV technique would be an obvious choice, since the technique is able to investigate flow fields, turbulence quantities in gas–liquid systems and bubble size as well.

Numerical work

The main weak point of the proposed numerical model of the Hydrojet cell is the assumption of constant diameter of the bubbles. Actually after the bubbles are introduced into the cell, they are further broken under the turbulent conditions in the mixing region and are then dispersed throughout the cell by the pumping action of the jets. Bubbles in this region may collide and coalesce. The equilibrium bubble size distribution in the cell is dictated by all the events taking place in the cell, in particular by the relative rates of bubble breakage and bubble coalescence in the cell. Thus in order to determine the bubble-particle collection and flotation rate in the Hydrojet cell, by means of the models presented in Section 5.3, it is necessary to compute not only

three-dimensional distributions of the turbulence dissipation rates, turbulence kinetic energies and volume fractions of air but also bubble size distributions. Thus a considerable improvement of the model would be obtained coupling a population balance model with the multi-phase modelling. Population balance is a well-established method in computing the size distribution of the bubbles and accounting for the breakage and coalescence effects in bubbly flows. Lo (2000) formulated the MUSIG model which involved discretization of the size distribution to size fractions, and this methodology has been introduced into the flotation model. Another method, suggested by Kocamustafaogullari and Ishii (1995), uses a balance equation for the interfacial area concentration and a similar method based on bubble number density was implemented into a CFD model by Lane et al. (2002).

Bibliography

Abrahamson, J. 1975. “Collision rates of small particles in a vigorously turbulent fluid.” *Chemical Engineering Science* 30(11):1371–1379.

Adrian, R.J. 1991. “Particle-imaging techniques for experimental fluid mechanics.” *Ann. Rev. Fluid Mechanics* 22:261–304.

Adrian, R.J. and C. Yao. 1984. “Development of pulsed laser velocimetry (PLV) for measurement of turbulent flow.” *Int. Symposium on Turbulence, University of Missouri, Rolla, Chem. Engr. Dept.,* 170–186.

Agüi, J.C. and J. Jiménes. 1987. “On the performance of particle tracking.” *J. Fluid Mech.* 185:447-468.

Ahmedi, G. 1987. “On the Machanics of incompressible multiphase suspensions.” *Adv. Water Res.* 10(32):32-43.

Ahmed, N. and G.J. Jameson. 1985. “The effect of bubble size on the rate of flotation of fine particles.” *International Journal of Mineral Processing* 14(3):195–215.

Anfruns, J.F. and J.A. Kitchener. 1977. “Rate of capture of small particles in flotation.” *Transactions of the Institution of Mining and Metallurgy, Section C: Mineral Processing and Extractive Metallurgy* 86:9–15.

Apsley, D. 2004. *CFD, Turbulence modelling in CFD.*

Apsley, D. 2013. *Introduction to CFD*. SPRING 2013.

Ashgriz, N. and J. Mostaghimi 2002. “An Introduction to Computational Fluid Dynamics.” in *Chapter 20 in Fluid Flow Handbook*. McGraw Hill Publishing.

Bakhvalov, N.S. 1966. “On the Convergence of a Relaxation Method with Natural Constraints on the Elliptic Operator.” *U.S.S.R. Computational Math. and Math. Phys.* 6(5):101-135.

Baldwin, B.S. and H. Lomax. 1978. “Thin layer approximation and algebraic model for separated turbulent flows.” *AIAA Paper* 78-257.

Bendat, J.S. and A.G. Piersol. 1986. *Random Data, Analysis and Measure Measurement Procedures*. 2nd ed. Wiley-interscience.

Bennett, A.J.R., W.R. Chapman, and C.C. Dell. 1958. “Froth flotation of coal.” *International Coal Preparation Congress, third ed. Brussels-Liege* E2:452–462.

Besnard, D.C. and F.H. Harlow. 1988. “Turbulence in Multiphase Flow.” *Int. J. Multiphase Flow*. 14(6):679-699.

Bloom, F. and T.J. Heindel. 1997. “Mathematical Modelling of the Flotation Deinking Process.” *Mathematical and Computer Modelling* 25(5):13-58.

Boussinesq, J. 1877. “Theorie de l'Ecoulement Tourbillant.” *Mem. Presentes par Divers Savants Acad. Sci. Inst. Fr.* 23:46-50.

Brandt, A. 1977. “Multi-Level Adaptive Solutions to Boundary- Value Problems.” *Math. Comp.* 31:333-390.

Brandt, A. 1981. *Guide to Multigrid Development. Multigrid Methods I.* Springer Verlag. Lecture Notes in Mathematics, No. 960.

Bröder, D. and M. Sommerfeld. 2002. "Experimental studies of bubble interaction and coalescence in a turbulent flow by an imaging PIV/PTV system." *Proceedings of the 11th International Symposium Application of Laser Techniques to Fluid Mechanics, Lisbon.*

Brücker, C. 2000. "PIV in two-phase flows." *Lecture series 2000-01, Von Karman Institute for Fluid Dynamics, Rhode-Saint-Genese, Belgium.*

Carbini, P., R. Ciccu, M. Ghiani, F. Satta, and C. Tilocca. 1996. "Oil agglomeration using water jets." *VIth International Mineral Processing Symposium Kusadasi Settembre 1996.*

Carbini, P., R. Ciccu, M. Ghiani, F. Satta, and C. Tilocca. 1998a. "A new concept in flotation technology, Proc. 5th Pacific Rim International Conference on Water Jet Technology." *New Dehli, India, Vijay M.M, Babu N.R. and Yahiro T (eds), Allied Publishers Ltd, New Delhi* 295-301.

Carbini, P., R. Ciccu, M. Ghiani, F. Satta, and C. Tilocca. 1998b. "Flotation of barite fines with the new Hydrojet cell." *Proc.7th International Mineral processing Symposium Innovations in Mineral and Coal processing, Istanbul.*

Carbini, P., R. Ciccu, M. Ghiani, F. Satta, and C. Tilocca. 2001. "Flotation of a sulphide ore using high velocity water jets." *Proc. VI SHMMT/XVIII ENTMME, Rio de Janeiro* 5.

Carbini, P., R. Ciccu, M. Ghiani, F. Satta, and C. Tilocca. 2007. "Advances in Coal Flotation Technology." *Proc. Third Int. Conf. on Clean Coal Technologies for our Future, Cagliari May* 15.

Castleman, K.R. 1996. *Digital Image Processing*. Prentice Hall.

Cebeci, T. and A.M.O. Smith. 1967. "Numerical solution of the turbulent boundary layer equations." *Douglas aircraft division report DAC 33735.*

Chudacek, M.W., S.H. Marshall, M.A. Fichera, J. Burgess, and F.L. Burgess. 1997. "Super-Scavenging of Zinc Tailings by Fastflot 2500 at Pasminco Mining, Broken Hill." *International Journal of Mineral Processing* 10(4):357-366.

Ciccu, R. and I. Kursun. 2011. "Potential advances in flotation by using water jets." *Physicochem. Probl. Miner. Process.* 46:35-50.

Coirier, W.J. and K.G. Powell. 1995. "An Accuracy Assessment of Cartesian-Mesh Approaches for the Euler Equations." *J. Computational Physics* 117:121-131.

Collins, D.N. and D. Read. 1971. "The treatment of slimes." *Mineral Science and Engineering* 3:19-31.

Dai, Z., D. Fornasiero, and J. Ralston. 1998. "Influence of dissolved gas on bubble–particle heterocoagulation." *Journal of the Chemical Society Faraday Transactions 94 (14)* 1983–1987.

Dai, Z., D. Fornasiero, and J. Ralston. 1999. "Particle–bubble attachment in mineral flotation." *Journal of Colloid and Interface Science* 217(1):70–76.

Dai, Z., D. Fornasiero, and J. Ralston. 2000. "Particle–bubble collision models – a review." *Advances in Colloid and Interface Science* 85(2-3):231–256.

Davidson, L. 2003. “An introduction to turbulence models.” Chalmers University of Technology ed. Getebörg, Sweden.

Davidson, L. 2012. “Fluid mechanics, turbulent flow and turbulence.” Division of Fluid Dynamics Department of Applied Mechanics Chalmers University of Technology SE-412 96 Goteborg, Sweden.

De Zeeuw, D. and K.G. Powell. 1993. “An Adaptively Refined Cartesian Mesh Solver for the Euler Equations.” *J. Computational Physics* 56-68.

Deardorff, J.W. 1970. “A numerical simulation of 3-dimensional turbulent channel flow at large Reynolds numbers.” *J. Fluid Mech.* 41:453-480.

Deen, N.G. 2001. “An Experimental and Computational Study of Fluid Dynamics in Gas-Liquid Chemical Reactors.” *Ph.D. thesis, Aalborg, University Esbjerg, Denmark.*

Deen, N.G., T. Solberg, and B.H. Hjertager. 2001. “Large eddy simulation of the gas-liquid flow in a square cross-sectioned bubble column.” *Chem. Eng. Sci., 56* 6341-6349.

Deen, N.G., T. Solberg, and B. H. Hjertager. 2002. “Flow generated by an aerated Rushton impeller, Part I: two-phase PIV experiments.” *Can. J. Chem. Eng.* 80:1-15.

Deen, N.G., J. Westerweel, and E. Delnoij. 2002. “Two-Phase PIV in Bubbly Flows: Status and Trends.” *Chem. Eng. Technol.* 25:97-101.

Delnoij, E., F.A. Lammers, J. A. M. Kuipers, and W.P.M. Van Swaaij. 1997. “Dynamic simulation of dispersed gas-liquid two-phase flow using a discrete bubble model.” *Chem. Eng. Sci.* 52:1429–1458.

Delnoij, E., J. Westerweel, N.G. Deen, J. A. M. Kuipers, and W. P. M. Van Swaaij. 1999. “Ensemble correlation PIV applied to bubble plumes rising in a bubble column.” *Chem. Eng. Sci.* 54:5159–5171.

Derjaguin, B.V. and S.S. Dukhin. 1961. “Theory of flotation of small and medium-size particles.” *Bulletin – Institution of Mining and Metallurgy* 651:21–246.

Dobby, G.S. and J.A. Finch. 1987. “Particle size dependence in flotation derived from a fundamental model of the capture process.” *International Journal of Mineral Processing* 21(3-4):241-260.

Drew, D.A. 1983. “Mathematical modelling of two-phase flow.” *ann. Rev. Fluid. Mech.* 15:261-291.

Drew, D. and R. T. Lahey. 1979. “Applications of general constitutive principles to the derivation of multidimensional twophase flow equations.” *Intl J. Multiphase Flow 5* 243-264.

Emerson, Z.I. 2007. *Particle and Bubble Interactions in Flotation Systems*. Auburn University.

Enwald, H., E. Peirano, and A.E. Almstedt. 1996. “Eulerian Two Phase Flow Theory Applied to Fluidization.” *Int. J. Multhiphase Flow* 22:21-66.

Favre, A. 1965a. “Equations des gaz turbulents compressibles, part 1: formes gènèrales.” *Journal de MQcanique 4* 361-390.

Favre, A. 1965b. “Equations des gaz turbulents compressibles, part 2: methode des vitesses moyennes; methode des vitesses moyennes pondèrèes par la masse volumique.” *Journal de MBcanique* 4:391-421.

Fedorenko, R.P. 1962. “A Relaxation Method for Solving Elliptic Difference.” *Equations. U.S.S.R. Computational Math. and Math. Phys.* 1(5):1092-1096.

Feng, D. and C. Aldrich. 1999. “Effect of particle size on flotation performance of complex sulphide ores.” *Minerals Engineering* 12(7):721-731.

Ferziger, J.H. and M. Peric. 1995. *Computational Methods For Fluid Dynamics*. Berlin: Springer-Verlag.

Finch, J. A. and G. S. Dobby. 1990. *Column Flotation*. Oxford: Pergamon Press.

Fkymier, P.D., H.A. Hassan, and M.D. Salas. 1988. “Navier-Stokes Calculations Using Cartesian Grids: I Laminar Flows.” *AIAA Journal* 26:1181-1188.

Gaudin, A.M. 1957. *Flotation*. 2nd ed. New York: McGraw-Hill Book Company.

Gonzalez, R.C. and R.E. Woods. n.d. *Digital Image Processing*. 3rd ed. 2008: Prentice Hall.

Gorman, M.G. and R.W. Smith. 1991. “Amine flotation of fine quartz and glass beads.” *Minerals Engineering* 4(12):1219-1226.

Grota, B. and K. Strau. 2000. “DPIV in a particle-laden gas flow - the influence of the particle fluctuation velocities on the accuracy of several cross-correlation-based analysis methods.” *In Proceedings of EUROMECH 4*. Eindhoven, The Netherlands.

Gui, L. and W. Merzkirch. 1996. “ Phase-separation of PIV measurements in two-phase flow by applying a digital mask technique.” *ERCOFTAC Bulletin 30* 45-48.

Gui, L., W. Merzkirch, and J.Z. Shu. 1997. “Evaluation of low image density PIV recordings with the MQD method and application to the flow in a liquid bridge.” *Journal of Flow Visualization and Image Processing* 4:333-343.

Harlow, F.H. and A.A. Amsden. 1975. “Numerical Calculation of Multiple Fluid Flow.” *Journal of Computational Physic* 17:19-52.

Heindel, T.J. 1999. “Fundamentals of flotation deinking.” *Tappi J.* 82(3):115.

Hilgers, S., W. Merzkirch, and T. Wagner. 1995. “PIV measurements in multiphase flow using CCD-and Photo-camera.” *ASME FED* 209:151–154.

Hiltunen, K., A. Jäsberg, S. Kallio, H. Karema, M. Kataja, A. Koponen, M. Manninen, and V. Taivassalo. 2009. *Multiphase Flow Dynamics - Theory and Numerics*. Helsinki: VTT.

Honaker, R.Q. and A.V. Ozsever. 2003. “Evaluation of the selective detachment process in flotation froth.” *Minerals Engineering* 16:975–982.

Huang, H.T., H.E. Fielder, and J.J. Wang. 1993a. “Limitation and improvement of PIV, Part I: Limitation of conventional techniques due to deformation of particle image patterns.” *Exp. Fluids* 15:168-174.

Huang, H. T., H. E. Fielder, and J. J. Wang. 1993b. “Limitation and improvement of PIV, Part II: Particle image distortion, a novel technique.” *Exp. Fluids* 15:263-273.

Ishii, M. 1975. *Thermo-Fluid Dynamic theory of Two Phase Flow*. Eyrolles.

Ishii, M. and K. Mishimam. 1984. “Two-Fluid Model and Hydro-dynamic Constitutive Relations.” *J. Nuclear Engineering and Design* 82:107–126.

Ishii, M. and N. Zuber. 1979. “Drag coefficient and relative velocity in bubbly, droplet or particulate flows.” *AIChE J.* 25:843–855.

Issa, R.I. 1986. “Solution of the implicitly discretized fluid flow equations by operator splitting.” *J. Computat. Phys.* 62:40–65.

Ityokumbul, M.T., J.A. de Aquino, C.T. O’Connor, and M.C. Harris. 2000. “Fine pyrite flotation in agitated column cell.” *Int. J. Miner. Process.* 58:167-178.

Jakobsen, H.A., B.H. Sanns, S. Grevskott, and H.F. Svendsen. 1997. “Modeling of vertical bubble-driven flows.” *Ind. Eng. Chem. Res.* 36:4052–4074.

Jameson, G.J., S. Nam, and M.M. Young. 1977. “Physical factors affecting recovery rates in flotation.” *Minerals Science Engineering* 9(3):103–118.

Jia, Y. and S.S.Y. Wang. 2005. “Numerical Model Validation Using Physical Model Data.” *Us-China Workshop On Advanced Computational Modleing In Hydroscience & Engineering*.September 19-21, Oxford, Mississippi, USA.

Kataoka, I. and A. Serizawa. 1989. “Basic Equations of Turbulence in Gas-Liquid Two-Phase Flow.” *Int. J. Multiphase Flow* 15(5):843-855.

Keane, R.D. and R.J. Adrian. 1990. “Optimization of Particle Image Velocimeters.” *Measurement Science and Technology* 2:1202-1215.

Kiger, K.T. and C. Pan. 2000. “PIV technique for the simultaneous measurement of dilute two-phase flows.” *J. Fluids Eng.* 122:811–818.

Kocamustafaogullari, G. and M. Ishii. 1995. “Foundation of the interfacial area transport equation and its closure relations.” *International Journal of Heat and Mass Transfer* 38:481-491.

Koh, P. T. L., M. Manickam, and M. P. Schwarz. 2000. “ CFD simulation of bubble-particle collisions in mineral flotation cells.” *Minerals Engineering, 13*, pp. 1455-1463.

Koh, P.T.L. and M.P. Schwarz. 2003. “CFD modelling of bubble-particle collision rates and efficiencies in a flotation cell.” *Minerals Engineering* 16:1055-1059.

Koh, P. T. L. and M. P. Schwarz. 2005. “CFD modelling of bubble-particle attachments in a flotation cell.” *Centenary of Flotation Symposium 2005,* Brisbane, Australia.

Kolmogorov, A.N. 1941. “On the degeneration of isotropic turbulence in an incompressible viscous fluids.” *Dokl. Akad. Nauk.* 31:538-541.

Kolmogorov, A.N. 1941. *The local structure of turbulence in incompressible viscous fluids at very large Reynolds numbers*. Dokl. Akad. Nauk.SSSR 30, 299-303.

Kolmogorov, A.N. n.d. “Dissipation of energy in isotropic turbulence.” *Dokl. Akad. Nauk. SSSR* 32:19-21.

Lahey, R.T. and D.A. Drew. 1989. “The Three Dimensional Time and Volume Average Conservation Equations for Two-Phase Flow.” *Adv. Nucl. Sci. Technol.* 20(1).

Lane, G.L, M.P. Schwarz, and G.M. Evans. 2002. “Predicting gas-liquid flow in a mechanically stirred tank.” *Applied Mathematical Modelling* 26:223-235.

Lane, G.L., M.P. Schwarz, and G.M. Evans. 2003. “Development of improved methods for computational modelling of gas dispersion in stirred tanks.” *3rd International Conference on CFD in the Minerals and Process Industries, Melbourne, Australia.*

Lange, A.G., W.M. Skinner, and R.St.C. Smart. 1997. “Fine:coarse particle interactions and aggregation in sphalerite flotation.” *Minerals Engineering* 10(7):681-693.

Launder, B.E. and D.B. Spalding. 1972. *Mathematical Models of Turbulence*. London: Academic Press.

Lesieur, M. and O. Metais. 1996. “New trends in large-eddy simulations of turbulence.” *Ann. Rev. Fluid Mech.* 28:45-82.

Liepe, F. and H.O. Moeckel. 1976. “Studies of the combination of substances in liquid phase. Part 6: The influence of the turbulence on the mass transfer of suspended particles.” *Chemische Technik (Leipzig, Germany)* 28(1):205-209.

Lilek, Z. and M. Peric. 1995. “A fourth order finite volume method with colocated variable arrangement.” *Comput. Fluids* 24:239–252.

Liu, J., T. Mak, Z. Zhou, and Z. Xu. 2002. “Fundamental study of reactive oily-bubble flotation.” *Minerals Engineering* 15:667-676.

Lo, S. 2000. “Application of population balance to CFD modelling of gas-liquid reactors.” *Trends in Numerical and Physical Modelling for Industrial Multiphase Flows Conference, Corse.*

Lourenco, L. and A. Krothapalli. 1995. “On the accuracy of velocity and vorticity measurements with PIV.” *Exp Fluids* 18:421-442.

Luttrell, G.H. and R.H. Yoon. 1992. “A hydrodynamic model for bubble-particle attachment.” *J. Colloid Interface Sci.* 154:129–137.

Lynch, A.J., N.W. Johnson, E.V. Manlapig, and C.G. Thorne. 1981. “Mineral and coal flotation circuits, their simulation and control.” *In: Fuerstenau, D.W. (Ed.), Developments in Mineral Processing Elsevier, Amsterdam* 291.

Manninen, M. and V. Taivassalo. 1996. *On the mixture model for multiphase flow*. VVT.

Markatos, N.C. 1986. “Computer simulation techniques for turbulent flows.” *Encyclopedia of Fluid Mechanics”, Vol. 3, (Ed.) Chereminishoff, N.P., Gulf Publishing Co.*

Matis, K.A., G.P. Gallios, and K.A. Kydros. 1993. “Separation of fines by flotation techniques.” *Separation Technologies* 3:76-90.

Menter, F.R. 1992. “Influence of free stream values on k-ω turbulence model predictions.” *AIAA Journal, 30(6)* 1657-1659.

Menter, F.R. 1994. “Two-Equation Eddy-Viscosity Turbulence Models for Engineering Applications.” *AIAA Journalr* 32(8):269-289.

Mileva, E. and L. Nikolov. 2003. “Entrapment efficiencies of hydrodynamic boundary layers on rising bubbles.” *Journal of Colloid and Inteiface Science* 265:310-319.

Nallaswamy, M. 1987. “Turbulence models and their application to the predictions of internal flows: A review.” *Computational Fluids* 15:151.

Nobach, H., N. Damaschke, and C. Tropea. 2004. “High-precision sub-pixel interpolation in PIV/PTV image processing.” *Proc. 12th Int. Symp. on Appl. of Laser Techn. to Fluid Mechanics,* Lisbon, Portugal. paper 24.1.

Norris, L.H. and W.C. Reynolds. 1975. “Turbulent channel flow with a moving wavy boundary.” *Stanford Univ. Dep. Mech.Eng. Rep.* FM-10.

Patankar, S,V. 1980. *Numerical Heat transfer and Fluid Flow*. New York: Hemisphere Publishing Co.

Patankar, S.V. and D.B. Spalding. 1972. “A calculation procedure for heat, mass and momentum transfer.” *Int. J. Heat Mass Transfer* 15:1787.

Prandtl, L. 1925. “Uber die ausgebildete Turbulenz.” *ZAMM* 5:136-139.

Prandtl, L. 1945. “Uber ein neues Formelsystem fur die ausgebildete Turbulenz.” *Nacr.Akad. Wiss. Gottingen, Math-Phys. Kl.* 6-19.

Pratt, W.K and J. Wiley. 2001. *Digital Image Processing, 3rd Edition*. John Wiley.

Press, W.H., B.P. Flannery, S.A. Teukolsky, and W.T. Vetterling. 1992. *Numerical recipes in FORTLAN: The Art of Scientific Computing*. 2nd ed. Cambridge: Cambridge University Press.

Pyke, B., D. Fomaserio, and J. Ralston. 2003. “Bubble particle heterocoagulation under turbulent conditions.” *Journal of Colloid and Interface Science* 265:141-151.

Raffel, M., C. Willert, and J. Kompenhans. 1998. *Particle Image Velocimetry A practical Guide*. Berlin: Springer.

Ralston, J. and S.S. Dukhin. 1999a. “The interaction between particles and bubbles.” *Colloids and Surfaces A: Physicochemical and Engineering Aspects* 151(1-2):3–14.

Ralston, J., S.S. Dukhin, and N.A. Mishchuk. 1999b. “Inertial hydrodynamic particle–bubble interaction in flotation.” *Int. J. Miner. Process.* 56(1-4):207– 256.

Ralston, J., S.S. Dukhin, and N.N. Mishchuk. 2002. “Wetting film stability and flotation kinetics.” *Advances in Colloid and Interface Science* 95:145–236.

Reay, D. and G.A. Ratcliff. 1975. “Experimental testing of the hydrodynamic collision model of fine particle flotation.” *Canadian Journal of Chemical Engineering* 53(5):481–486.

Renade, V.V. 2002. “Computational flow modeling for chemical reactor engineering.” San Diego, CA, USA: Academic Press.

Reynolds, O. 1895. “On the Dynamical Theory of Incompressible Viscous Fluids and the Determination of the Criterion.” *Philosophical Transactions of the Royal Society of London, Series A* 186:123.

Rietema, K. and H.E.A. van den Akker. 1983. “On the Momentum Equations in Dispersed Two Phase Flow.” *Int. J. Multiphase Flow* 9(1):21-36.

Rodi, W. 1984. *Turbulence Models and their Application in Hydraulics*. Delft, The Netherlands, IHRA.

Roesgen, T. 2003. “Optimal subpixel interpolation in particle image velocimetry.” *Exp. in Fluids* 35:252–256.

Saffman, P.G. and J.S. Turner. 1956. “On the collision of drops in turbulent clouds.” *J. Fluid Mech.* 1:16-30.

Sato, Y. and K. Sekoguchi. 1975. “Liquid velocity distribution in two-phase bubble flow.” *Int. J. Multiphase Flow* 2:79–95.

Scarborough, J.B. 1958. *Numerical Mathematical Analisys*. 4th ed. Baltimore: University Press.

Schiller, L. and A. Nauman. 1933. “A drag coefficient correlation.” *VDI Zeits* 77:318–320.

Schubert, H. and C. Bischofberger. 1979. “On the optimization of hydrodynamics in flotation processes.” *Proceedings of 13th Int. Miner. Process. Cong. Warszawa* 2:1261–1287.

Schulze, H.J. 1984. *Physico-chemical Elementary Processes in Flotation: An Analysis from the Point of View of Colloid Science Including Process Engineering Considerations*. Amsterdam, New York: Elsevier.

Schulze, H.J. 1993. "Flotation as a Heterocoagulation Process: Possibilities of Calculating the Probability of Flotation." Pp. 321-353 in *Coagulation and Flocculation: Theory and Application (B.Dobias, Editor)*, vol. 47, *Surfactant Science Series*. New Yorh: Marcel Dekker.

Seol, D.G., T. Bhaumik, C. Bergmann, and S. A. Socolofsky. 2007. "Particle Image Velocimetry Measurements of the Mean Flow Characteristics in a Bubble Plume." *J. Eng. Mech. 133* 665-676.

Seol, D.G. and S.A. Socolovsky. 2008. "Vector post-processing algorithm for phase discrimination of two-phase PIV." *Exp. Fluids* 45:223-239.

Sivamohan, R. 1990. "The problem of recovering very fine particles in mineral processing – a review." *International Journal of MineralProcessing* 28:247–288.

Smagorinsky, J. 1963. "General circulation experiments with the primitive equations." *Mon. Weather Rev*. 91:99–165.

Song, S., A. Lopez-Valdiviesco, J.L. Reyes-Bahena, and C. Lara-Valenzuela. 2001. "Floc flotation of galena and sphalerite fines." *Minerals Engineering* 14(4):87-98.

Soto, H. and G. Barbery. 1988. "Separation of fine particles by floc flotation." *Proceedings of the International Symposium on the Production and Processing of Fine Particles, A.J. Plumpton (ed.)* 297-307.

Sridhar, G., B. Ran, and J. Katz. 1991. "Implementation of particle image velocimetry to multiphase flow." *Cavitation Multiphase Flow Forum, ASME, New York* 205–210.

Subrahmanyam, T.V. and K.S.E. Forssberg. 1990. "Fine particles processing: Shear-flocculation and carrier flotation. A review." *Int. J. Min. Process.* 30(3-4):265–286.

Sutherland, K.L. 1948. "Physical chemistry of flotation XI. Kinetics of the flotation process." *Journal of Physical and Colloid Chemistry* 52:394–425.

Tao, D. 2005. "Role of bubble size in flotation of coarse and fine particles — A review." *Separation Science and Technology 39 (4)* 39 (4):741–760.

Tennekes, H. and J.L. Lumley. 1972. *A First Course in Turbulence*. Cambridge: MIT Press.

Tomlinson, H.S. and M.G. Flemming. 1963. "Flotation rate studies." *Proc. Sixth Inter. Min. Proc. Congr. (Cannes)* 463-573.

Trahar, W.J. 1981. "A rational interpretation of role of particle size in flotation." *International Journal of Mineral Processing* 2:289–327.

Tropea, C., A. L. Yarin, and J. F. Foss. 2007. *Springer Handbook of Experimental Fluid Mechanics*. Springer.

van der Wijngaart, R.J.F. 1990. "Composite grid techniques and adaptive grid refinement in CFD." *Report ClaSSiC-90-07, Dept. of Computer Science, Stanford University*.

Van Doormal, J.P. and G.D. Raithby. 1984. "Enhancements of the SIMPLE method for predictingincompressible flows." *Numerical Heat Transfer* 7:147–163.

Versteeg, H.K. and W. Malalasekara. 1995. *An Introduction to Computational Fluid Dynamics: The Finite Volume Method*. Harlow: Longman Scientific & Technica.

Weber, M.E. and D. Paddock. 1983. "Interceptional and gravitational collision efficiencies for single collectors at intermediate Reynolds numbers." *Colloid Interface Sci.* 94(2):328–335.

Westerweel, J. 1993. "Digital particle image velocimetry - theory and application." *PhD thesis, Delft University*.

Westerweel, J. 1994. "Efficient detection of spurious vectors in particle image velocimetry data." *Exp. Fluids 16* 236–247.

Westerweel, J, D. Dabiri, and M. Gharib. 1997. "The Effect of a Discrete Window Offset on the accuracy of Cross Correlation Analysis of Digital PIV Recording." *Experiments in Fluids 23 (1)* 20-28.

Wilcox, D.C. 1988. "Reassessment of the Scale Determining Equation for Advanced Turbulence Models." *AIAA Journal* 26(11):1299-1310.

Willert, C.E. and M. Gharib. 1991. "Digital particle image velocimetry." *Experiments in Fluids* 10(4):181-193.

Wörner, M. 2003. *A Compact Introduction to the Numerical Modeling of Multiphase Flows*. Institut fur Reaktorsciherheit. Programm Nukleare Sicherheitsforschung.

Yoon, R.H. 1991. "Hydrodynamic and surface forces in bubble–particle interactions." *Aufbereitungs Technik* 32(9):474-485.

Yoon, R.H. and G.H. Luttrell. 1986. "The effect of bubble size on fine coal flotation." *Coal Preparation* 2:179–192.

Yoon, R.H. and G.H. Luttrell. 1989. "The effect of bubble size on fine particle flotation." *Mineral Processing and Extractive Metallurgy Review* 5:101–122.

Yoon, R.H. and L. Mao. 1996. "Application of extended DLVO theory, IV. Derivation of flotation rate equation from first principles." *Journal of Colloid and Interface Science* 181(2):613–626.

Zikanov, O. 2010. *Essential Computational Fluid Dynamics*. John Wiley & Sons, Inc.